ABSTRACT

Title of Dissertation: DEVELOPMENT AND WHIRL FLUTTER TESTING OF SWEPT-TIP TILTROTOR BLADES

James Sutherland
Doctor of Philosophy, 2022

Dissertation Directed by: Professor Anubhav Datta
Department of Aerospace Engineering

This thesis describes the development and whirl flutter testing of swept-tip tiltrotor blades. The blades are tested on the Maryland Tiltrotor Rig (MTR). The MTR is also developed as part of this thesis. MTR is a new test facility developed to support the research and development of next-generation high-speed tiltrotors. It is a parametric test bed for developing a fundamental understanding of high speed tiltrotor flight and acquisition of test data to validate advanced simulation tools. The baseline MTR is a Froude-scaled, 4.75 feet diameter, 3-bladed, semi-span, floor-mounted, optionally-powered, gimballed flutter rig. In this work, the rotor blades are designed with the objective of gaining a fundamental understanding of the impact of a swept-tip on tiltrotor whirl flutter. Two sets of blades are fabricated for wind tunnel testing – straight and swept. The blades have a VR-7 profile, chord of 3.15 inches, and linear twist of -37° per span. The blades have a uniform cross section with mass and stiffness properties loosely based on a 1/5.26 Froude scale XV-15 rotor properties. The swept-tip blades are identical to the straight blades up to 80% radius, where a 20° sweep back angle is introduced to assess the impact on whirl

flutter. The cross-section was designed using in-house 2-D section analysis tools. The blade inertial and structural properties were carefully measured. A novel method was developed to attain more reliable measurements of the blade cross-sectional stiffness using accelerometers as tilt sensors. Full 3-D models of the blades were also developed concurrently. These models were built in CATIA, meshed in Cubit, and analyzed with X3D. These models were validated with test data of the measured blade properties. Experiments in a vacuum chamber were carried out to measure frequencies and strains. The 3-D model was validated with this data. Tests and predictions proved the blades have sufficient structural integrity and stress margins to allow for wind tunnel testing. The first whirl flutter test of the MTR was completed in the Naval Surface Warfare Center Carderock Division (NSWCCD) 8- by 10-ft large subsonic wind tunnel. Testing was performed in four configurations for both blade geometries. The configurations progressed step-by-step from the baseline configuration of a gimballed rotor, freewheeling flight, with wing fairings installed; the second configuration removed the wing fairings; the third then locked the rotor gimbal; the fourth configuration then operated in powered flight. The frequency and damping of the wing beam and chord bending were collected at a rotor speed of 1050 RPM and wind speeds up to 100 knots. The 100 knots speed was a limitation posed by NSWCCD. In freewheel flight, the swept-tip blades increase the damping and stability of the wing chord bending mode, even at lower flight speeds. However, in powered flight, the opposite effect is observed. The parametric testing results in a comprehensive data set for evaluating the effect of swept-tip blades on whirl flutter. Richer data is expected at higher speeds where the aerodynamic and inertial couplings of the swept-tip blades are expected to be more pronounced. Nevertheless, it is hoped that the results presented in this work will inspire further investigation using advanced computational tools to develop a more complete understanding of tiltrotor whirl flutter and ultimately eliminate it.

DEVELOPMENT AND WHIRL FLUTTER TESTING OF SWEPT-TIP TILTROTOR BLADES

by

James Robert Sutherland

Dissertation submitted to the Faculty of the Graduate School of the
University of Maryland, College Park in partial fulfillment
of the requirements for the degree of
Doctor of Philosophy
2022

Advisory Committee:
Professor Anubhav Datta, Chair/Advisor
Professor Inderjit Chopra
Professor James Baeder
Professor Alison Flatau
Professor Maria Cameron, Dean's Representative

Acknowledgments

This work would not have been possible to complete on my own and required the support of my friends, family, fellow graduate students, professors, and most especially my advisor Dr. Anubhav Datta. I am blessed to have found my way into Dr. Datta's research group at the University of Maryland five years ago. I could always rely on the unconditional support of Dr. Datta to accomplish my goals. I cannot thank you enough for your guidance, wisdom, and constantly giving me the opportunity to flourish.

Although I was initially unsure if I wanted to pursue a Ph.D., I quickly decided it was the best choice after I fell in love with the Maryland Tiltrotor Rig project and the people I got to work with regularly. During my first summer of graduate school, I learned invaluable skills from Dr. William Staruk and Lauren Wolfe. I would also like to thank Dr. Daniel Lathrop for inspiring me to develop the accelerometer method to measure blade stiffness. I'd like to give a special thank you to the members of the Tiltrotor Research Lab: Fred Tsai, Seyhan Gul, Lex (Cheng) Chi, Amy Morin, Akinola Akinwale, Nate O'Brien, and Xavier Delgado for your tireless efforts and long nights preparing for wind tunnel testing; working with you was never a chore and always joyful. Thank you to my friends and colleagues Ravi, Emily, Katie, Brandyn, Shashank, Mrinal, Abhishek, Wanyi, Brent, Eric, Matt, Dan, and everyone else in the Alfred Gessow Rotorcraft Center.

I owe unending gratitude to my family. Thank you to my parents, who raised me to always be curious about the world and continuously thirst for knowledge, and my brothers for inspiring me to pursue my passions. To my wife, Rosie, even though we were often separated by a 129-mile stretch of I-95, thank you for your love, patience, and support every day, forever and always.

I am thankful for the financial support from the Clark Doctoral Fellowship provided by A. James Clark Foundation. This work is also funded by the Vertical Lift Research Center of Excellence (VLRCOE) and the Office of Naval Research (ONR). The carbon fiber material used to fabricate the blades was donated by the Boeing Company. Lastly, I received invaluable technical guidance from experts at Army Research Lab (ARL), NASA Langley, NASA Ames, Naval Surface Warfare Center, Bell, Boeing, and Sikorsky.

Table of Contents

List of Tables

List of Figures

Chapter 1: Introduction

This chapter introduces the topic of this dissertation. It begins with the motivation behind this thesis and the research objectives, then describes the history and development of fixed-wing sweep, forward sweep, rotary-wing sweep as well as tiltrotors and the nature of whirl flutter instability and use of swept-tip tiltrotor blades before concluding with an outline of the organization of this thesis.

1.1 Motivation

While man took first flight in an airplane with fixed wings, the dream of hovering motionless in the air can be traced back to Leonardo da Vinci and led to the development of the modern helicopter. Helicopters are aircraft which rely on one or more sets of rotating wings (rotors) to provide lift, thrust, and control for an aircraft. Because the lifting surfaces are not stationary, like those of a fixed-wing aircraft, a helicopter is able to perform vertical takeoff and landing (VTOL) as well as hover stationary at a point and fly in any direction.

Even a bird cannot hover, except for the hummingbird. The dream of vertical flight was likely the same dream which drove Leonardo da Vinci (1452-1519) to sketch the first heavier-than-air, manned, flying machine shown in Fig 1.1. Although it never flew, Leonardo's aerial screw inspired countless efforts over the subsequent 500 years to design and innovate new machines capable of hovering flight. It wasn't until 30 years after the Wright Brothers first cruised over the sand dunes of Kitty Hawk that the Focke 61, the world's first practical helicopter, achieved stable and controlled flight [1]. However, the helicopter's rotor, which enables VTOL and hover, places limitations on the helicopter's aerodynamic lift and propulsion in forward flight. A modern turboprop aircraft, such as the one shown in Fig. 1.2, has a maximum cruise speed of 351 knots (650 km/hr) while a conventional helicopter, shown in Fig. 1.3, has a maximum speed of 120 knots (220 km/hr) [2]. Thus, there exists a trade-off between efficient, high-speed flight and VTOL capabilities.

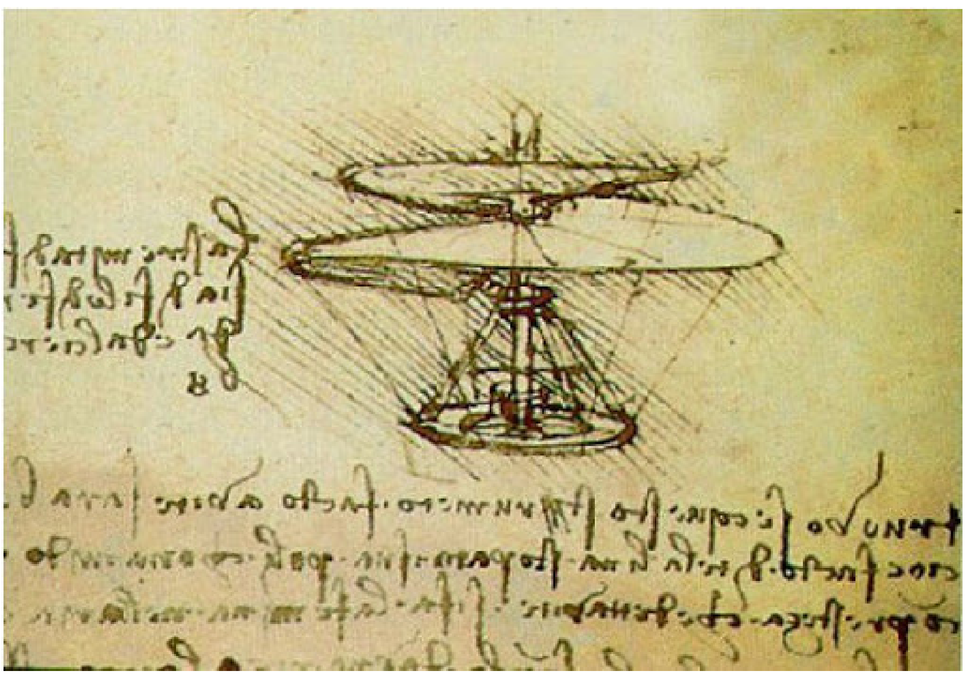

Figure 1.1: Leonardo da Vinci's sketch of an aerial screw flying machine.

Tiltrotor aircraft, such as the experimental XV-15, military V-22, or the civil AW-609 shown in Fig. 1.4, combine the vertical takeoff and landing (VTOL) ability of a

Figure 1.2: A typical turboprop aircraft (Piper Cheyenne III).

Figure 1.3: A conventional helicopter (Bell 206).

helicopter with the cruise ability of fixed-wing aircraft to perform many long range and high-speed missions. A tiltrotor is able to accomplish this feat by taking off with the rotors mounted vertically at the wing tips as seen in Fig. 1.4. Once in the air, the aircraft begins to transition as rotors tilt forward. A conversion maneuver over 10-20 seconds brings the rotors down to orient horizontally like a typical propeller. The rotors which can flap like a helicopter rotor, but also serve double duty as propellers in cruise are called proprotors. In this way, a tiltrotor is able to achieve significantly higher speeds than a helicopter up to about 250 knots (km/hr), while still maintaining hover capabilities. Efficient helicopter mode flight still requires the rotors to be large, have cyclic controls, flexible blades for flapping, and a compromise for twist–lower than a propeller, but much higher than a conventional helicopter rotor. Furthermore, the tip speed in cruise is reduced by 15-20% from hover to partially compensate for the twist. Tiltrotors are a marvel of modern engineering.

The tiltrotor configuration provides a balanced compromise between fixed-wing cruise flight and helicopter VTOL capabilities. However, dramatic expansions of speed, range, and payload are desired for future vertical lift aircraft. A grand vision for the future is to achieve speeds up to 350-400 knots in cruise as seen in modern turboprop aircraft. One of the key barriers to this goal is whirl flutter, a dynamic instability that occurs in tiltrotors during high speed flight. Current methods to solve or delay whirl flutter introduce new limits on cruise speed. There is a severe lack of publicly available test data on tiltrotor whirl flutter in order to study the phenomenon and develop new technologies that can achieve the dream of an aircraft that can hover and fly at over 400 knots airspeed.

That is the overarching motivation behind the Maryland Tiltrotor Rig (MTR).

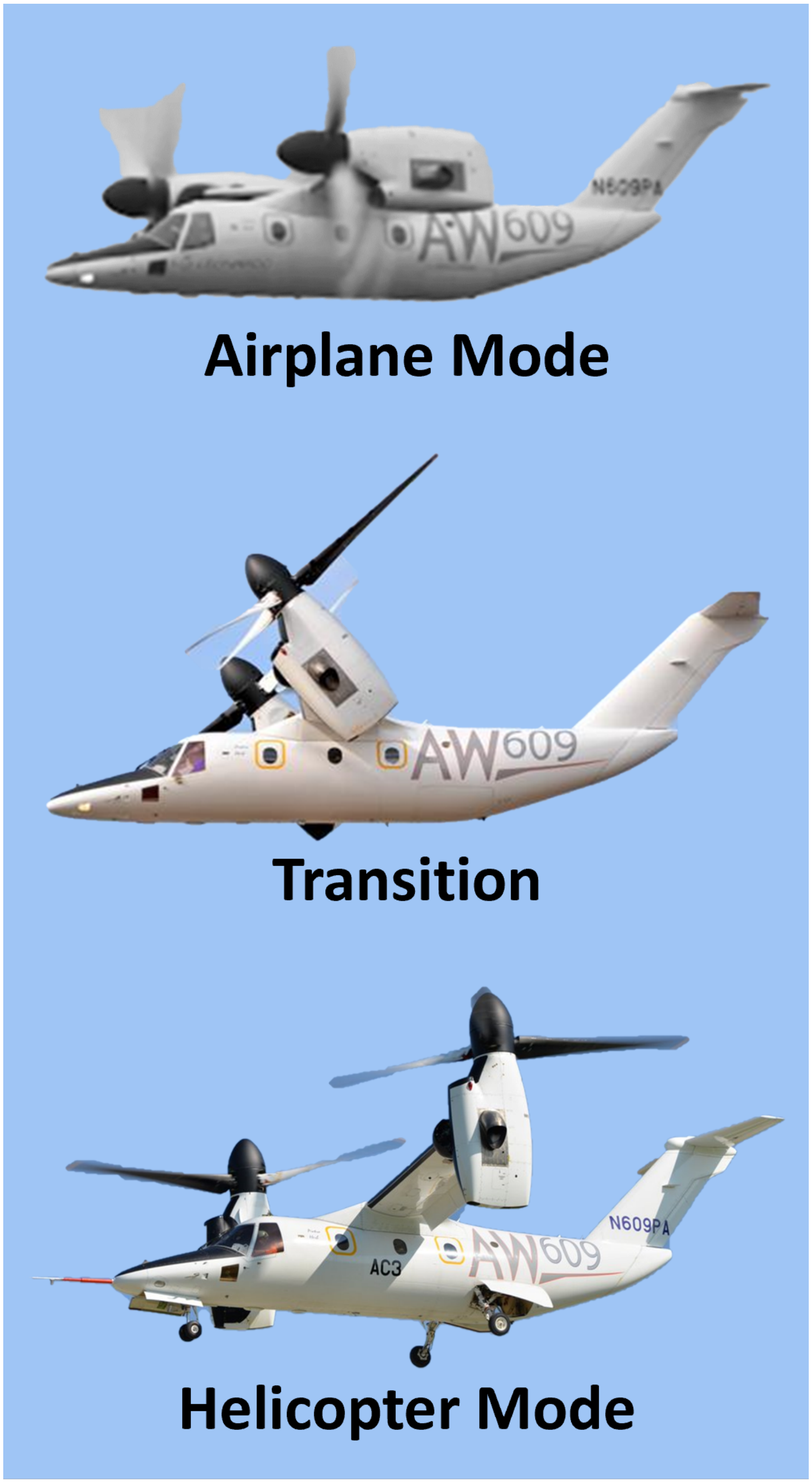

Figure 1.4: A tiltrotor in hover, transition, and cruise (AW-609).

1.2 Objectives

The objective is to develop a brand new research rig at the University of Maryland specially designed to provide parametric variations in blade geometry, hub type, and model flexibility and develop instrumentation to acquire high-quality research data. This dissertation covers the development of this rig with particular emphasis on fabrication, testing, and understanding the impact of a new set of tiltrotor blades with a swept-tip. Wind tunnel tests are carried out with straight and swept-tip blades to measure wing-pylon damping up to 100 knots. The speed of 100 knots in the model-scale (Froude) is equivalent to about 235 knots of the full-scale XV-15 aircraft.

1.3 Fixed-Wing Sweep

The concept of sweep for an aerodynamic surface was first introduced by Adolf Busemann in 1929 for fixed-wing aircraft flying at supersonic speeds [3]. Supersonic flow occurs when the freestream Mach number, defined as the ratio of airspeed to the speed of sound, is above 1. At these speeds, shock waves appear on the wing and the flow pattern changes with a dramatic increase in drag due to the effects of compressibility. When the Mach number is below 0.8, the flow is considered subsonic. Between 0.8-1.0 Mach, the flow is considered transonic. In this regime, as the air accelerates over an airfoil, local areas of the flow exceed the speed of sound and create shock waves.

Busemann reasoned that by sweeping the wing to be at an angle relative to the airflow, the velocity perpendicular to the leading edge and thereby the local Mach number will be reduced. The reduced Mach number will ultimately lead to lower drag and more efficient lift generation due to a higher lift-to-drag ratio. He later presented his work at the fifth Volta Conference titled 'High Velocities in Aviation' in October of 1935. Albert Betz quickly applied the same concept to wings in transonic flow [4]. A wing with a sweep angle of Λ reduces the apparent airspeed over the wing by $\cos \Lambda$. This allows for a fixed wing aircraft to reach higher speeds before encountering shock waves over the surface of the wing.

However, at the time, few aircraft had been able to achieve speeds faster than half the speed of sound, which is about 380 mph (610 km/hr). So the ideas of Busemann and Betz, no matter how forward thinking, did not take hold. The fact that their home country of Germany recognized the military significance of their discovery and marked it as confidential leading into the start of World War II also halted its dissemination. During the war, German scientists and engineers continued to study swept wings eventually building the first jet-powered airplane, sketched in Fig. 1.6 [4]. The jet engines provided enough power for the Messerschmitt Me-262 to reach a maximum speed of 542 knots (1000 km/hr) in a steep dive, coming much closer to the speed of sound. In contrast, the only jet-powered fighter used by the Allies during World War II, Gloster Meteor sketched in Fig. 1.7, had straight wings and was markedly slower [5].

In the United States, R. T. Jones independently derived the idea of swept wings. Initially, the idea was rejected by the publishers who did not believe such a simple change could cause such a significant effect [6]. Only once the war had been won and the Allies harvested research from German laboratories and found the research of Busemann, Betz, and others as well as the aircraft the Luftwaffe had been flying was Jones able to publish his findings [7].

After the end of World War II, jet airplanes began to revolutionize aviation. Propeller aircraft were not able to provide the thrust necessary to meet the ever growing demand for faster aircraft. Supersonic flight was first achieved by Chuck Yeager flying the Bell X-1 aircraft in October 1947, seen in Fig. 1.8. Many American experts, once doubtful of swept wings, were now surprised that supersonic flight was possible with a straight wing [8]. Ultimately, the rocket powered aircraft had more than enough power to overcome the large drag force created by the straight wing as it approached supersonic speeds. However, the rocket was incredibly inefficient compared to jet engines and therefore required the plane to be launched from beneath a B-29 bomber for test flights. The first supersonic flight in a more practical, jet-powered aircraft was completed by George Welch in an XP-86, a prototype for the F-86 Sabre, seen in Fig. 1.9. By some accounts, Welch's first supersonic flight pre-dates Yeager's and could be considered outright as the first supersonic flight [9]. The power of the new jet engines, combined with the reduced transonic drag of swept wings were key breakthroughs which enabled manned aircraft to break the sound barrier.

Progressing into the modern age, nearly all aircraft capable of reaching transonic or supersonic speeds can trace their lineage through the use of swept wings back to Busemann's paper at the fifth Volta Conference.

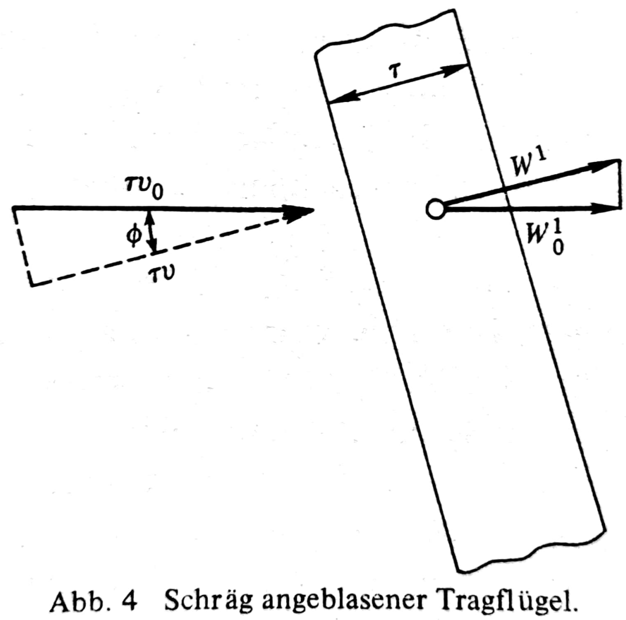

Figure 1.5: Adolf Busemann's diagram of airflow over a swept wing [3].

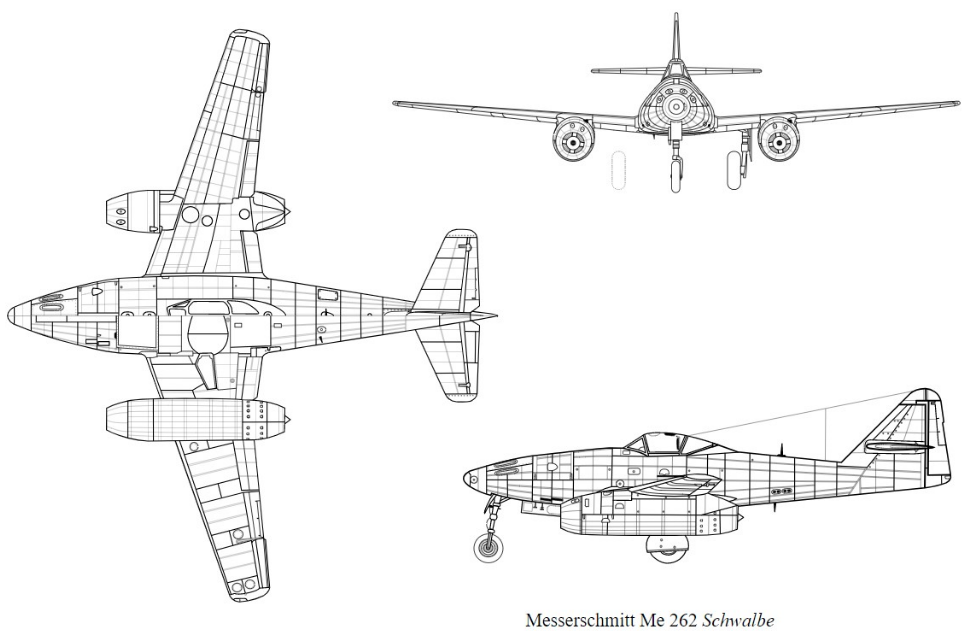

Figure 1.6: Drawing of the Messershmitt Me-262 (1944).

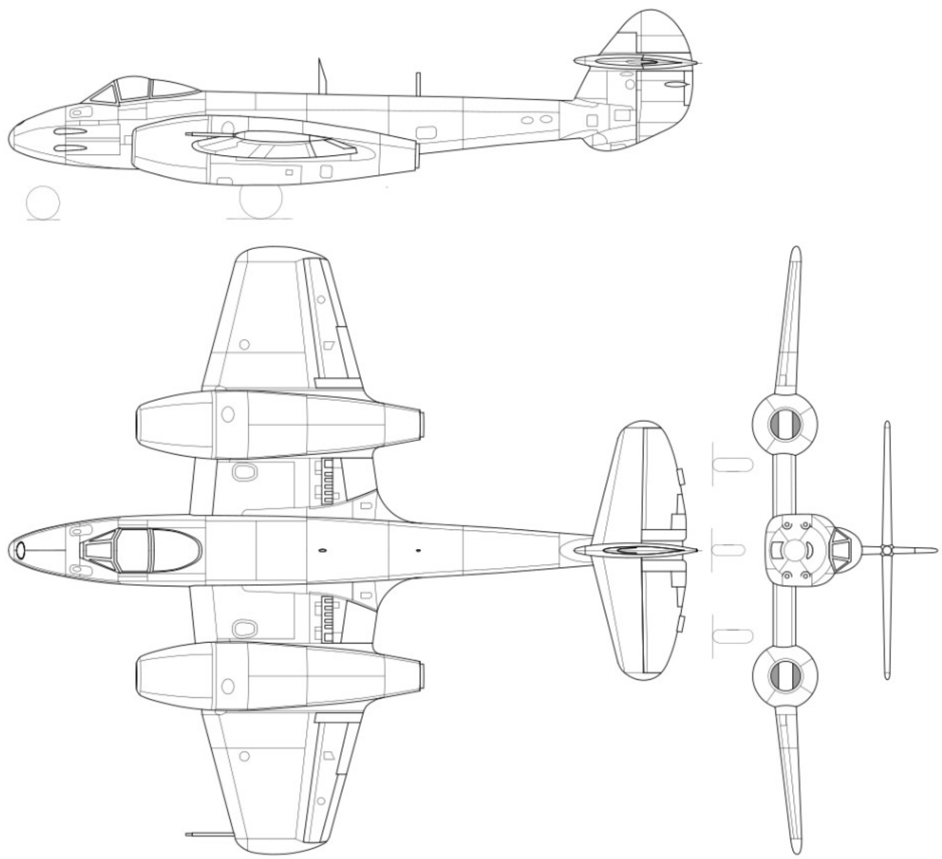

Figure 1.7: Drawing of the Gloster Meteor (1944).

Figure 1.8: Test flight of the Bell X-1 rocked-powered aircraft (1947).

Figure 1.9: Test flight of the North American XP-86 (1947).

1.4 Forward Sweep

Nearly all aircraft with significant wing sweep have the wings swept aft. However, the same principle applies for wings swept forward as well. The most notable example aircraft is the Grumman X-29, seen in Fig. 1.10. A forward swept wing has been shown to offer higher lift-to-drag ratios, lower trim drag, and better stall characteristics than an identical aft-swept wing [10, 11]. However, forward sweep are highly susceptible to aeroelastic limitations known as static divergence [12–15]. The forward sweep moves the aerodynamic center forward so an increase in lift causes the wing to twist up leading to unfavorable bending-torsion coupling. A higher angle of attack results in a positive feedback loop with more lift. At a high enough speed, the effective wing torsional stiffness goes to zero and ultimately fails. It was not until the 1980s after the advancement of composite materials that a specifically tailored composite wing could be designed to eliminate divergence that further experimentation could be done [16, 17]. The Grumman X-29 used composite bending-torsion coupling to compensate for the aerodynamic coupling introduced by the forward sweep [18]. The wings of the V-22 and XV-15 are also forward swept 6.5 degrees. But this was to avoid the danger of the gimballed rotor blades striking the wing [19]. The modern V-280 eliminates this sweep as flapping motion can now be predicted and controlled with high precision.

Figure 1.10: Test flight of the Grumman X-29 (1984).

1.5 Rotary-Wing Sweep

Although helicopters are not able to achieve the same forward flight speeds as fixed wing aircraft, the effects of compressibility and transonic flow are still the same on the tip of the advancing blade. In helicopters, the effect is more complicated by the unsteady nature of the flow. A typical blade tip encounters transonic flow 300 times a minute. This is because in hover, the Mach number at the blade tip is typically about 0.6. When the helicopter begins to fly forward, the aircraft velocity is added to the rotational velocity on the advancing side of the rotor and subtracted from the retreating side. The advance ratio, μ, is defined as the ratio of forward flight speed to hover tip speed. In addition to creating areas of transonic flow on the advancing side, the retreating side also sees reverse flow over a circle of radius μ located at $\frac{\mu}{2}$ on the retreating side; furthermore, there can be dynamic stall near the blade tip. The asymmetry of flow creates a rolling moment which can only be balanced by reducing lift on the advancing side. Thus a helicopter can generate lesser and lesser lift as it flies faster and faster – a fundamental limitation of a single main rotor helicopter.

Extensive research has been performed to study the effect of rotor blade tip shape on performance, as well as acoustics and vibrations [20]. As a part of these experimental and numerical investigations, a variety of tip geometry parameters were studied including taper, anhedral, and sweep [21, 22]. Introducing sweep to the outer 10% of the blade delays the generation and growth of shock waves on the advancing blade tip [23, 24]. The use of sweep in combination with anhedral was shown to reduce the power requirement of the rotor in forward flight [25–27]. As in fixed-wing aircraft, by sweeping the blade tip, the apparent Mach number is reduced, leading to reduced drag and higher lift-to-drag ratios. In addition to performance, sweeping the blade tip may also influence the location of tip vortices and mitigate blade vortex interactions to reduce rotor noise [28–31]. Most tip sweeps are limited to the outer 10% of the blade. This is because of the dynamic effects of the sweep. As the tip sweeps aft, the aerodynamic center and center of gravity also move aft with it, introducing not only the bending torsion coupling of fixed-wings but also inertial couplings due to centrifugal effects and unsteady motion of the helicopter blades. Ultimately, the inclusion of a swept tip alters the aeroelastic response of the rotor and changes its stability in high speed flight [32, 33]. Figures 1.11-1.12 shows a variety of swept-tip rotor blades used on modern helicopters.

One unique attempt to include a swept tip while offsetting the adverse effects of

(a) UH-60 S

(b) CH-53 K

(c) AH-64 A

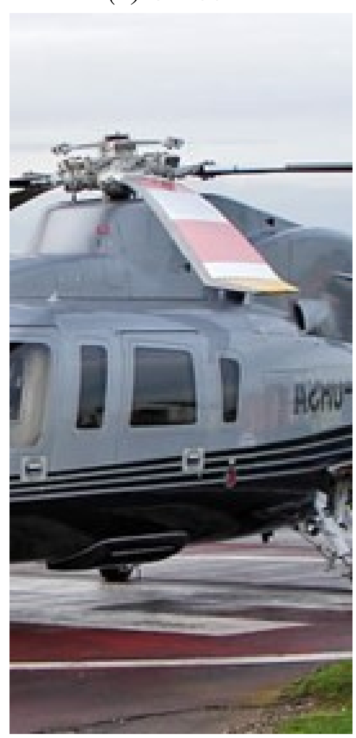

(d) S-76 C

Figure 1.11: Modern helicopter rotors with swept-tips.

(a) S-92 A

(b) NH-90

(c) AW-139

(d) EC-135

(e) G-LYNX (BERP)

Figure 1.12: More modern helicopter rotors with swept-tips.

shifted center of gravity and aerodynamic center is the blade tip developed under the British Experimental Rotor Program (BERP). The blade tip has a curved sweep so that the Mach number along the blade radius remains nominally constant. But, the blade section is shifted forward to ensure the aerodynamic and gravity centers remain on the blade quarter-chord line. The BERP blade tip installed on a Lynx helicopter still holds the World Speed Record of 216 knots (400 km/hr) set in 1986 [34]. The record was not entirely due to the blade, however. An engine upgrade added an extra 700 hp and the exhaust was expelled through a modified exhaust port to generate 600 lb of thrust. In effect, it was a compound helicopter that blasted through the high compressibility drag.

In summary, conventional helicopters apply sweep to the rotor blade tip for similar reasons as fixed wing aircraft: to reduce the apparent Mach number and achieve more efficient transonic flight. But for helicopter rotors, the effect is far more complicated due to the inertial couplings from the rotating and unsteady blade motions. Thus, only modest expansions in speeds are achieved.

1.6 Tiltrotor Development

Tiltrotors are able to avoid the issue of asymmetric lift and the effects of compressiblity by tilting the rotors. This allows the rotors to mostly be in axial flight and limits the compounding effects of high-advance ratio, edgewise flight.

One of the first recorded flights of an aircraft with tilting rotors was a vehicle developed by Henry Berliner in the early 1920s [35]. The aircraft, shown in Fig. 1.13 looks similar to a standard biplane of its time, except for the two exceptionally large diameter propellers were located near the wing tips and mounted on a tilting mechanism. Since the rotors did not tilt completely horizontal, it was only capable of reaching speeds up to 35 knots (65 km/hr) [19]. But the configuration of side-by-side rotors mounted to wing tips persisted as the typical configuration for all current tiltrotor aircraft.

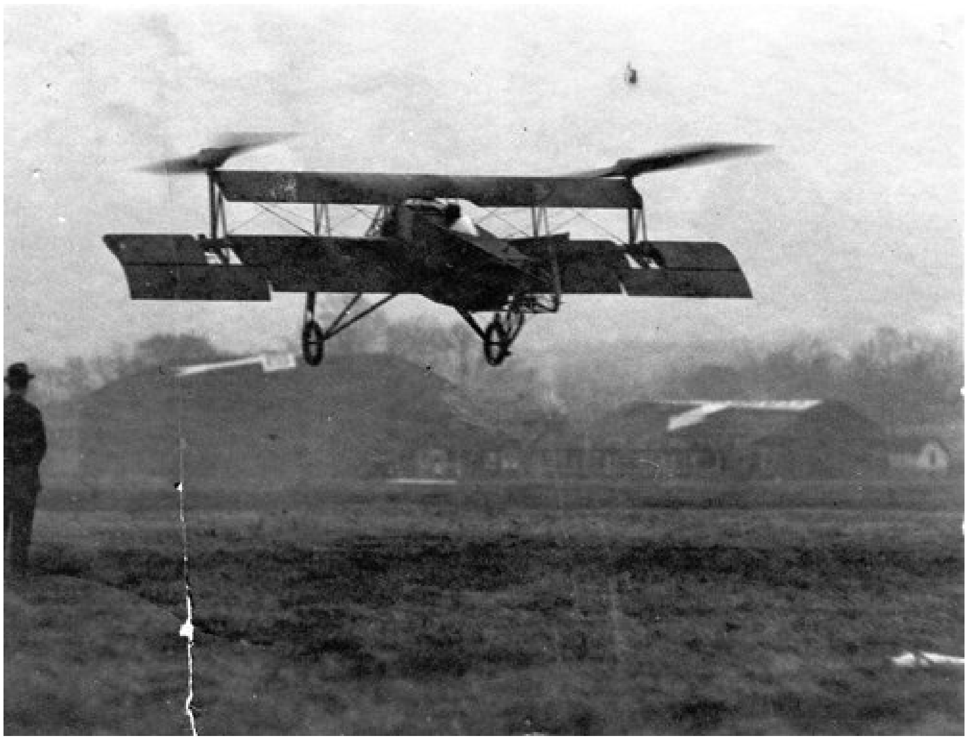

Figure 1.13: Berliner tilt-propeller helicopter hovering over a field (1922).

The next flying tiltrotor was built upon 30 years of aeronautical knowledge. Now featuring a more efficient mono-wing and rotors capable of conversion to complete airplane mode, the Transcendental Model 1-G shown in Fig. 1.14 was the first aircraft to explore the conversion from helicopter to airplane mode. Unfortunately, while attempting flight within 10 degrees of full conversion, the aircraft suffered a major crash, ending the research effort [36].

During the same time period, the Bell XV-3 was developed in response to the U.S. Army/Air Force call for advanced VTOL aircraft: convertiplanes. Initial forays into con-

Figure 1.14: Hover testing of the Transcendental Model 1-G tilt rotor (1954).

version flight resulted in severe instabilities. But, after focused investigation, replacing the original three-bladed articulated rotor (Fig. 1.15a) with a two-bladed stiff-inplane rotor (Fig. 1.15b) the aircraft was able to alleviate the instability [19, 36]. The XV-3 continued flight testing until the program was completed in 1966 after 250 test flights and becoming the first tiltrotor to demonstrate full conversion between helicopter and airplane modes. Though the initial instabilities had been alleviated by replacing the rotors, the problems encountered with the XV-3 revealed inherent aeroelastic stability concerns for the rotor/pylon/wing system that needed to be addressed for any future tiltrotor designs. This instability, commonly known as whirl flutter, is addressed in more detail in the subsequent section. It is fortunate that the XV-3 was only able to reach 115 knots (212 km/hr) in level flight or else it might have also been destroyed [19].

Driven by the promise of an operational tiltrotor capable of flight in helicopter and

(a) Original 3 bladed rotor (1955)

(b) Re-designed 2-bladed rotor (1960)

Figure 1.15: Bell XV-3 hovering in helicopter mode.

airplane modes, tiltrotor development continued. After a series of model scale aeroelastic tests of tiltrotors to address whirl flutter, the XV-15 was developed as a research aircraft and technology demonstrator. The XV-15, shown in Fig. 1.16, conducted flight testing starting in 1977. The XV-15 rotor consists of three blades mounted on a constant-velocity gimbal joint. While no test regiment is not without incidents and mishaps, the shining achievement of the XV-15 was demonstrating stable, flutter-free flight across the entire flight envelope [37–39]. The successful flight testing of the XV-15 aircraft lead directly into design of the V-22 Osprey.

Figure 1.16: Bell XV-15 flying in hover (1977).

The tiltrotors that are flying today: V-22, V-280, and AW-609 are all inspired or derived from technology used on the XV-15. As such, they each have a three-bladed gimballed rotor with straight, highly-twisted proprotor blades. Unfortunately, the vehicle properties and flight data are either confidential or proprietary and so the last tiltrotor wind tunnel and flight test data is from the XV-15 or scale models developed even earlier. The lack of publicly available test data provides a challenge for the development of new analytical tiltrotor models and prediction of whirl flutter instabilities.

1.7 Whirl Flutter Instability

Tiltrotor whirl flutter was first observed during flight testing of the Bell XV-3 tiltrotor and quickly became the subject of focused research [40]. The discovery occurred at a similar time as 2 fatal crashes of Lockheed Electra of which propeller whirl flutter was also determined to be the cause [41].

In propeller whirl flutter, a pitch or yaw perturbation tilts the rotor plane away from the freestream. This changes the effective angle of attack of the propeller blade as it rotates about the shaft. An in-plane force and, in the case of a pitch perturbation, a yaw moment is generated. This yaw moment couples with gyroscopic forces and precesses the shaft in a backward spiral. At large inflow ratios, the spiral becomes unstable and leads to whirl flutter [42].

Whirl flutter in proprotors is inherently different from propeller whirl flutter due to the flexibility of the blades, in particular, the flapping motion of the blades about the hub. This motion changes the nature of the gyroscopic and aerodynamic forces on the rotor. For a flapping rotor, the hub does not carry any moment; for a gimballed hub the moment is exactly zero, for a hingeless hub the moment is non-zero but small. This is deliberate, as the aircraft must support helicopter mode edgewise flow. This design feature now aggravates the instability. When the shaft is perturbed, unsteady aerodynamic forces trigger cyclic flap motion which leads to a change in blade airloads both in and out of the rotor plane. The out of plane components generate a restoring force which tries to

(a) Bell-Boeing V-22 Osprey

(b) Leonardo AW-609

(c) Bell V-280 Valor

Figure 1.17: Tiltrotors flying in the present day.

bring the shaft back, but the in-plane component creates a force in the direction of the perturbation and tries to destabilize the precession of the rotor. At low inflow, this force lies hidden. However, as the cruise speed increases, the in-plane forces destabilize the shaft motion. The shaft is attached to the wing, so shaft motion is essentially wing motion. The damping of the wing motion becomes negative at high cruise speed. Usually, the symmetric wing modes are the culprit so semi-span models suffice to trigger the problem [40, 43–46].

After the discovery of tiltrotor whirl flutter with the XV-3, several key wind tunnel tests were conducted. In competition for the development of what later became the XV-15, two semispan rotors were tested in the NASA Ames 40-by-80-foot Wind Tunnel [44]. The first was a 25-foot diameter Bell rotor with a gimballed hub, which later became the XV-15 hub [47]. The second hub was a 25-foot diameter Boeing soft in-plane hingeless hub similar to the Bo-105 hub [48]. The wing, pylon, and rotor properties were documented and available to the public. However, the dataset was limited. The Bell rotor was ultimately selected and led to the full-aircraft test of the XV-15 in the Ames 40- by 80-foot tunnel [49]. Aeroelastic testing was performed as a part of this wind tunnel entry, however no data is available. Stability tests performed during flight tests also have no data available [39]. Fifty years later, the new NASA Tiltrotor Test Rig is the only other full-scale test article [50]. But this is a proprotor rig with only the rotor, without a wing, so not for flutter. The rotor, once again, is a Bell rotor, a BA-609 rotor, predecessor of the AW-609 before it was sold to Augusta-Westland. Hence no properties are available in the public domain.

In conjunction with full-scale tests, model scale tests were performed to gain a more fundamental understanding of tiltrotor whirl flutter. In 1975, the Boeing Vertol Company built two 2.8-ft Froude-scale models and these were tested in the Wright Brothers wind tunnel at MIT [51, 52]. The models measured gust stability. As part of the V-22 development, Bell conducted a series of systematic tests on a 1/5th scale model [53]. These tests lead to the evolution of the XV-15 hub and ultimately the V-22 hub. The right hand wing and rotor of this model later became the Wing and Rotor Aeroelastic Test System (WRATS) [54, 55]. The WRATS test rig was used to study a number of parametric variations to study their effect on tiltrotor whirl flutter. However, since it was derived from the V-22 scale model, the properties are not available to the public. The two other important tiltrotor scaled models were developed and tested were the Sikorsky's Variable Diameter Tilt Rotor (VDTR) [56] and NASA's Tiltrotor Aeroacoustic Models (TRAM) [57]. But, none of these models were tested for whirl flutter.

Tiltrotor whirl flutter is characterized by negative damping of the coupled wing-rotor elastic bending modes due to destabilizing in-plane forces generated by the rotor. Based on early analysis during the 70s [44], the damping of the wing torsion tends to increase with speed while the wing beam and chordwise modes tend to become unstable. This understanding was tied to the Bell 25-foot diameter rotor. The chordwise damping always decreases with speed for the geometries studied. The behavior of beamwise damping depends on the level of interaction with the rotor modes. For a gimballed or articulated hub, the beamwise damping increases when the wing bending frequency is less than the regressive lag frequency. Since the lag frequency decreases with speed, it ultimately goes below the wing bending frequency and the damping decreases until flutter occurs. Analysis of a hingeless hub shows similar trends. This understanding was tied to the Boeing 25-foot diameter rotor. However, the wing beam bending and regressive flap mode are highly coupled. For the hingeless hub, additional concern of air resonance becomes more important. It is clear these mechanisms are complex, mystified over the years further due to lack of research data. Research data must include detailed model properties, in addition to flutter data, in order to be considered complete. There is a dearth of such data on this complex phenomenon.

Tiltrotor whirl flutter is a complicated instability that has been observed to depend on many factors. The primary influence parameters are the wing frequencies, pylon mount properties, and pitch-flap coupling. The placement of the wing beam frequency is crucial to the onset of whirl flutter. As such, the wing stiffness and pylon mass have a strong influence on when whirl flutter sets in [45]. It has also been shown that increasing the pylon stiffness to be symmetric about pitch and yaw increases the flutter speed [43, 58]. The behavior can also be altered by coupling the pitch and flap rotor modes. Typically, this allows the torsion motion to act as a negative spring to decrease the flap frequency. At the same time, the change in pitch results in airloads that increase the lag frequency. In proprotors, negative pitch-flap coupling, incorporated by a positive δ_3 angle between the pitch link and the flap hinge, is predicted to be beneficial for whirl flutter but leads to flap-lag instability [58, 59]. Therefore, a negative δ_3 angle is used and, for moderate values, has been shown to also delay whirl flutter [45]. As if these were not confusing enough, other effects such as reduced stability with the rotor in windmill or the onset of compressibility add to the mix [60]. Even basic questions such as the impact of wing aerodynamics remain unclear.

For most whirl flutter testing, Mach effects are ignored. Therefore, a Froude scale model is chosen. This is mainly because there are no subsonic tunnels large enough that can safely operate at 300 knots. Froude scale models ensure similitude of the inertial and gravitational effects of the system [41, 61]. Since whirl flutter is a dynamic instability the inertial effects of the rotor and pylon is critical to testing. If the effects of compressibility are important for testing, the model must also be scaled to preserve the Mach number. In air, it is not possible to preserve both Froude and Mach number, but for some length scales, it is possible through the use of a heavy gas such as Freon as was the case with testing of the models in the Transonic Dynamics Tunnel at NASA Langley [54, 58].

1.8 Exciting the Model

Previous wind tunnel tests for whirl flutter have used a variety of methods to excite the model and measure the damping of each mode. Since the wing beam and chord bending modes are most likely participants in the instability, it is ideal to excite each of them individually. Early models plucked a set of strings that were attached in the wing beam and chord bending directions [58]. The pluck excited all frequencies of the wing and the time history of the vibration was recorded. The damping was extracted manually using the logarithmic decrement method. In order to excite specific frequencies, later rigs used gas jets on the wing tip pointed in the two bending directions. Damping was still extracted using the logarithmic decrement method but was supplemented by early implementations of a moving block method [60]. More recent tests sought a more efficient method of exciting the wing. High-bandwidth actuators at the swashplate allowed for control inputs at the desired wing frequency [54]. The moving block method is similar in concept to the text-book logarithmic decrement method but allows for frequency and damping extraction from a multi-mode transient response [62]. If the amplitude and phase are needed, the Prony analysis can be used.

1.9 Swept-Tip Tiltrotor Blades

Recently, numerical studies have shown that sweeping back the outer 15-20% of the rotor blade can delay whirl flutter [45, 63]. The swept tip is a major source of pitch-flap coupling for a rotor blade. Positive pitch flap coupling at the root (negative δ_3) stabilizes flap-lag flutter by separating the flap and lag frequencies but is destabilizing for whirl flutter. A swept tip can counter the positive pitch-flap coupling progressively with increases in speed as the blade lift increases [45]. Thus at low speed, the positive coupling is retained whereas at high speed it is countered. The sweep ultimately forces a negative pitch-lag coupling and aids in whirl flutter stability. This coupling is due to the offset of lift from the elastic axis of the blade so a perturbation in flap, and therefore lift, generates a pitching moment about the elastic axis. The center of gravity of the swept section should be at or ahead of the blade elastic axis so the inertial effects do not subtract from the beneficial aerodynamic effects. In addition to blade tip sweep, small amounts of tip dihedral have been predicted to increase the damping of the wing bending modes [63]. The same pitch-flap coupling achieved through a swept-tip can also be implemented through tailored composite couplings in the blade tip [46, 64]. All of these are conceptual conjectures tested only numerically, with no test data, hence no solid evidence to confirm.

The benefit of swept tips comes at a price. One study has shown blade sweep reduce the hover efficiency by 2.5% [65]. However, another saw small increases in the efficiency of the proprotor in hover and in cruise [45]. The principal effect is the increase in pitch link loads. The additional pitch-flap coupling has been predicted to produce up to a 19% increase pitch-link loads [45]. Higher control loads require stronger, heavier hub structures which ultimately add to the pylon mass. For a relatively small swept tip of the outer 5% of the blade, the weight of the blade increases by 5% [66]. For a larger swept portion of 20%, the blades will require more structure in the swept region and likely increase mass at the tip by a significant amount. This increased mass will generate higher centrifugal loading and, depending on the placement of the mass relative to the quarter chord, dramatically affect the lag loads [45]. The combination of high twist rates and swept tips also poses a potential fabrication challenge. But these challenges are not specific to tiltrotors, they appear for all helicopter rotors, and have successfully been addressed by advanced materials, superior design, and innovative hubs as the examples given earlier show.

There has been no experimental verification of the potential benefit of swept-tip tiltrotor blades nor a clear understanding of the physics. The Advanced Technology Blades (ATB) for XV-15 did include a swept-tip but were only placed on the outer 10% of the blade and tested only in hover [67]. More recently, the ONERA ADYN Blade design was tested in whirl flutter, but there is no parametric data available and the tip utilized a double sweep designed for acoustics, not dynamics [68, 69].

1.10 Thesis Organization

Following the Introduction, Chapter 2 provides an overview of the Maryland Tiltrotor Rig. Chapter 3 introduces the family of blades that were designed and fabricated for testing on the MTR. Chapter 4 presents the detailed blade properties. It also describes a new method to extract sectional stiffness using accelerometers to improve upon the error-prone mirror method. Chapter 5 develops a high-fidelity 3D finite element model and validates it with measured properties. Chapter 6 covers vacuum chamber testing for fan plot and 3-D strains up to 1050 RPM. Chapter 7 further investigates the structural integrity of the blades in hover and forward flight. X3D is used for these pre-test stress and strain predictions. Chapter 8 describes the whirl flutter test results. Chapter 9 ends with summary, conclusions, and recommendations for future research.

Chapter 2: The Maryland Tiltrotor Rig

This chapter provides an overview of the Maryland Tiltrotor Rig starting with objectives and overview and then detailing the major assemblies–wing assembly, pylon assembly, rotor assembly, and finally instrumentational calibration.

2.1 Objectives of the Rig

The objectives of the MTR is to provide a test-bed for basic research on aeromechanics of high-speed tiltrotors. A vision for the next generation of these aircraft is 400 kt flutter-free cruise with a turboprop-like thin wing (14% thickness to chord ratio) and a lightweight, low-vibration, high-performance proprotor. The objective of MTR is to enable this vision through systematic parametric variation of blades, hub, and wing spar. MTR is a research rig, not a scaled-down version of a particular aircraft. The immediate goals of the rig are to measure and eliminate whirl flutter, to be expanded thereafter to air-resonance of hingeless hubs, vibratory loads in conversion mode, and closed loop control of loads and instabilities. The MTR makes this possible with four key features:

1. A hub with interchangeable gimballed and hingeless options.

2. A 40 hp electric drive capable of powered and unpowered operations.

3. High bandwidth electric actuators for high frequency inputs to the swashplate.

4. The rig and hub designed to support up to Mach-scale rotors of 4.75-ft diameter operating at tip Mach numbers of up to 0.60.

5. A pylon that can be statically tilted from 90° (helicopter mode) to 0° (airplane mode) at increments of 5°.

2.2 Overview of the Rig

The Maryland Tiltrotor rig is a 3-bladed, semi-span, floor mounted rig utilizing the floor of the wind tunnel test section to approximate the aircraft fuselage. The baseline configuration includes a gimballed hub and a solid aluminum spar to achieve similar characteristics of a 1:5.26 scale XV-15. Figure 2.1 shows the dimensions of the MTR and the rotor axis system depicted in Fig 2.2. An overview of the important dimensions and features of the baseline MTR is found in Table 2.1

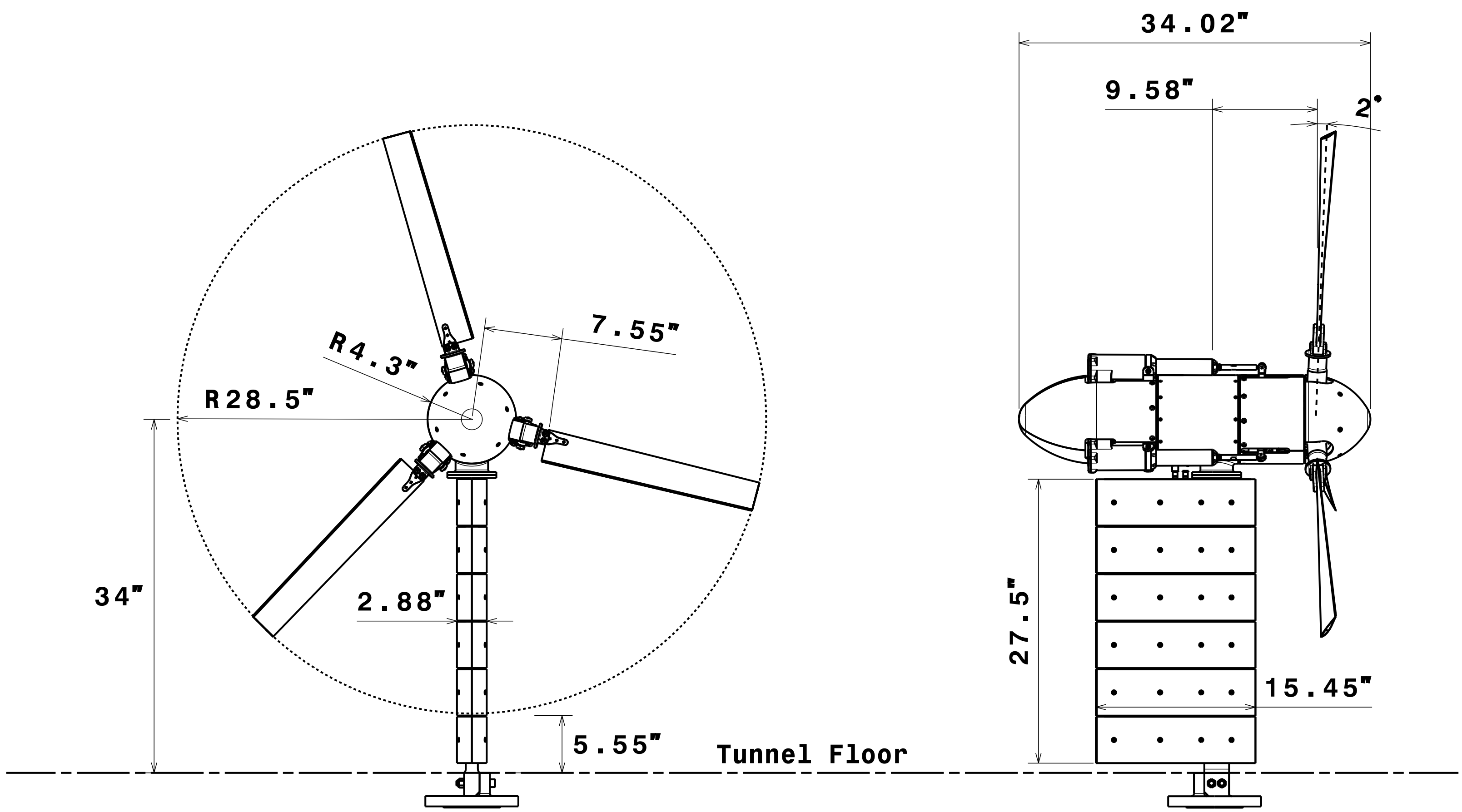

Figure 2.1: Dimensioned drawing of MTR in airplane mode.

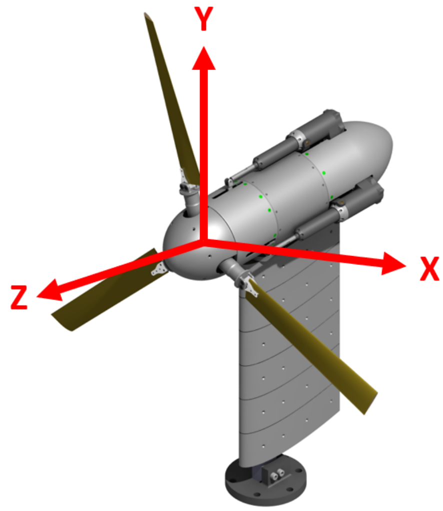

Figure 2.2: MTR coordinate axes.

The MTR is comprised of three major assemblies: the wing, pylon, and rotor. Each of which will be described in detail over the subsequent sections. Beyond the physical components of the rig, there is a full suite of sensors, data acquisition system, and flutter actuation mechanism that were required to be verified, calibrated, and developed.

2.3 Wing Assembly

The wing assembly supports the pylon and houses the power and sensor cables as well as hoses required to run the motor and collect sensor data from the MTR. The wing is straight, unlike the forward swept wings of the XV-15 and V-22, with no twist and comprised of three main components: the fairings, ribs, and spar. A schematic view of the wing is shown in Fig. 2.3 and the physical wing assembly is shown in Fig. 2.4.

The wing fairings are a NACA 0018 airfoil (18% thickness to chord ratio) with a 15.45 inch chord length and 27.5 inch span. While the wing airfoil is thinner than

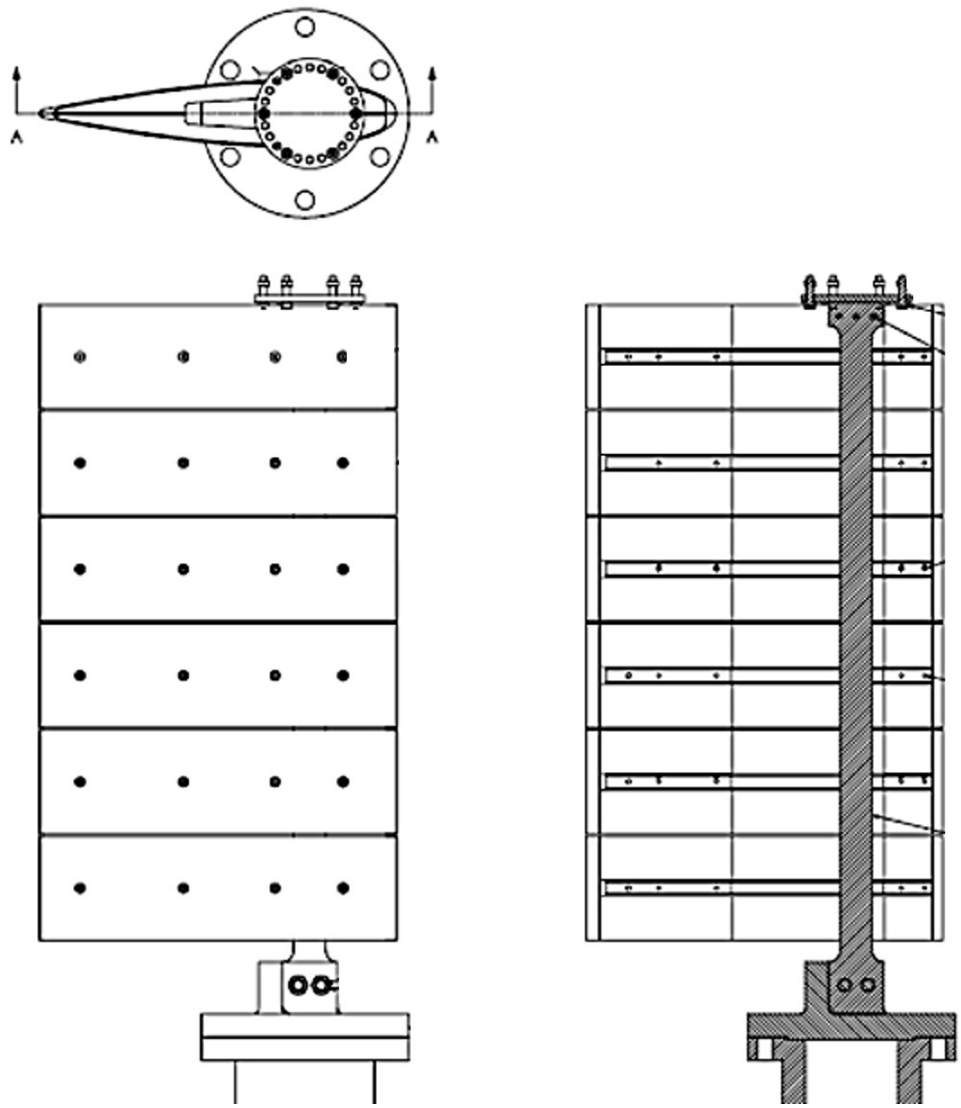

Figure 2.3: Wing assembly section view.

Table 2.1: Features and dimensions of the Maryland Tiltrotor Rig (MTR).

Model Feature	Description
Number of blades	3
Radius	28.5 in
Blade airfoil	VR-7
Wing airfoil	NACA 0018
Wing chord	15.44 in
Hub type	Gimballed
Pylon weight	71.17 lb
Static pylon tilt	0° : 5° : 90°
Electric Motor	40 hp

the flying tiltrotors, even thinner wings (14% thickness ratio) are targeted for the next generation of aircraft. Since wing stiffness is the key factor in whirl flutter, not the specific airfoil, the MTR can simulate thinner wings by designing a new spar with lower stiffness. The airfoils can also be changed in the future by changing the fairings as long as they are fabricated to have the same interface.

The wing fairings have a foam core with an outer shell made of fiber glass and are fabricated in 6 discrete sections so as not to add to the wing stiffness. The segmented wing leaves small gaps between each section to allow for spar deflection, which are covered with flexible tape to reduce adverse aerodynamic effects on the wing. The fairings are bolted to individual ribs through three #10-32 x 3/8 inch flat head bolts and one #10-32 x 3/16" along the span. The trailing edge of the two fairing halves is closed with two smaller bolts connecting the two fairings. The ribs are mounted to the spar, prior to attaching the fairings, with two #10-32 x 1-5/8 inch socket head bolts that pass through and screw into

(a) Side view of wing assembly with top fairing removed.

(b) Section of wing fairing mounted to the rib.

Figure 2.4: MTR wing assembly.

socket nuts installed in the opposite rib to clamp down on the spar between them. There are an additional four #10-32 x 3/4 inch socket head bolts that secure the ribs together located near the trailing and leading edges.

The spar is designed to be interchangeable and attaches to the base plate and pylon through bolted connections. In order to accommodate multiple cross sections, a CNC machined adapter is attached to the spar with a single counter-sunk bolt before attaching the ribs. These two sets of strain gauges were placed at 4.38% span to measure the beam and chord bending moments and a third set located at 6.93% span for torsion measurements. The spar cross-section was designed so that the fully assembled rig, excluding blades, would have similar natural frequencies to previous tiltrotor aircraft and test rigs. The natural frequencies of the spar mounted to the base plate with and without the fairings and

Table 2.2: MTR wing frequencies for the spar only and full wing assembly.

Mode	Spar Only	Wing Assembly
Beam (Hz)	40.5	23.9
Chord (Hz)	78.3	43
Torsion (Hz)	200	83

ribs were measured via a rap test; the results are shown in Tab. 2.2.

2.4 Pylon Assembly

The wing pylon is mounted to the pylon via a coupling plate shown in Fig. 2.5. The plate attached to the spar has two guide pins and bolt holes arranged every 15°; the coupling plate on the pylon has holes arranged every 20°. So, in mating the two together with 6 bolts, the verniered arrangement can statically tilt the pylon in 5 ° increments.

The pylon is comprised of an aluminum shell and fiber glass fairings which contain several key components of the MTR. Figure 2.6 shows engineering drawings of the pylon assembly. The 3 linear actuators provide high bandwidth swashplate control. The 64-channel slip ring carries all sensor data from the rotating frame. And the electric motor can be optionally powered to allow for both freewheeling and powered cruise flight.

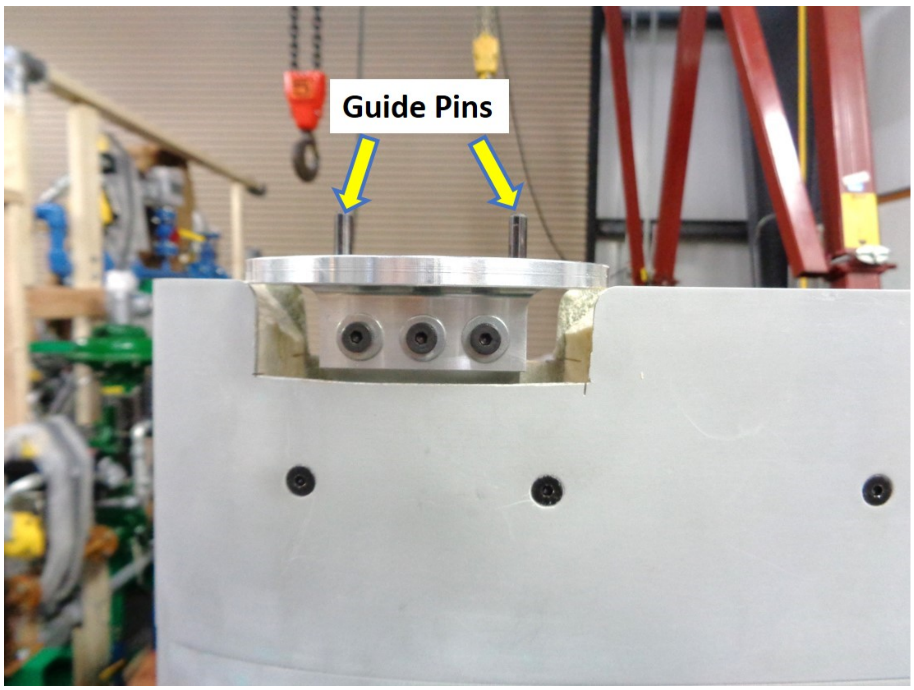

Figure 2.5: Spar coupling plate bolted to spar tip.

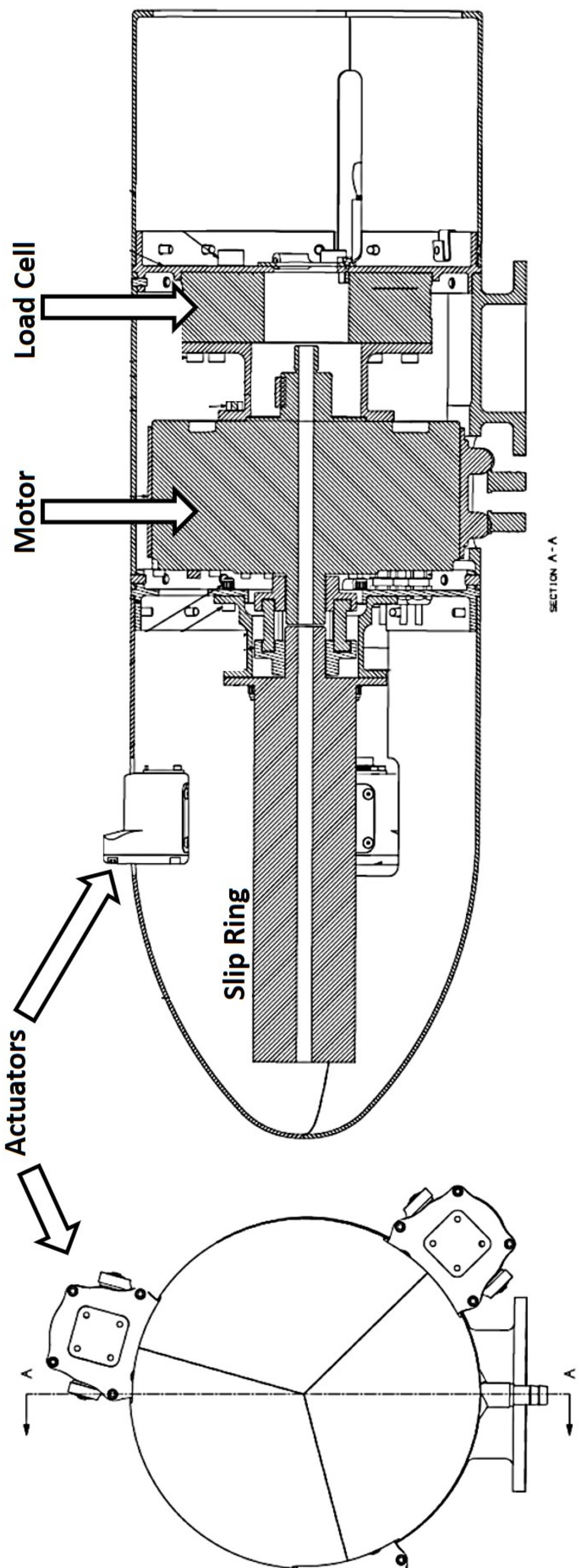

Figure 2.6: Engineering drawings of pylon assembly.

2.4.1 Pylon Mass, Center of Gravity and Moment of Inertia

The center of gravity (CG) and mass moment of inertia (MOI) of the pylon and rotor assemblies were measured using a Space Electronics CG/MOI machine at NASA Langley, shown in Fig. 2.7.

The machine is a rotating table resting on an air spherical bearing, which makes friction negligible, and is connected to a vertical torsion rod which allows the table to rotate. A moment transducer at the base of the rod measures the CG and MOI. To measure the CG location, the moment is measured at four points, each a 90° rotation of the table apart. For a known pylon mass and location relative to the machine's central axis, the CG can be calculated from the static moment measurements. To measure the MOI, the torsion rod is clamped at its base, given an initial torsional deformation, then released. The clamped rod act as a torsional pendulum and the moment of inertia can be calculated from the period using the following equation:

$$I = \kappa \left(\frac{T}{2\pi} \right)^2 \tag{2.1}$$

where κ (N-m/rad) is the known torsional stiffness of the rod, T (s) is the period of oscillation, and I (kg-m^2) is the mass moment of inertia of the entire system. Subtracting the previously measured inertia of the machine only provides the pylon MOI relative to the center of the machine. With the known CG location, the parallel axis theorem can be used to calculate the pylon inertia about the CG. In order to precisely know the location of the pylon relative to the machine, a special interface plate, shown in Fig. 2.8 was designed to mount the rig in both yaw and pitch directions. The mass, CG, and MOI of

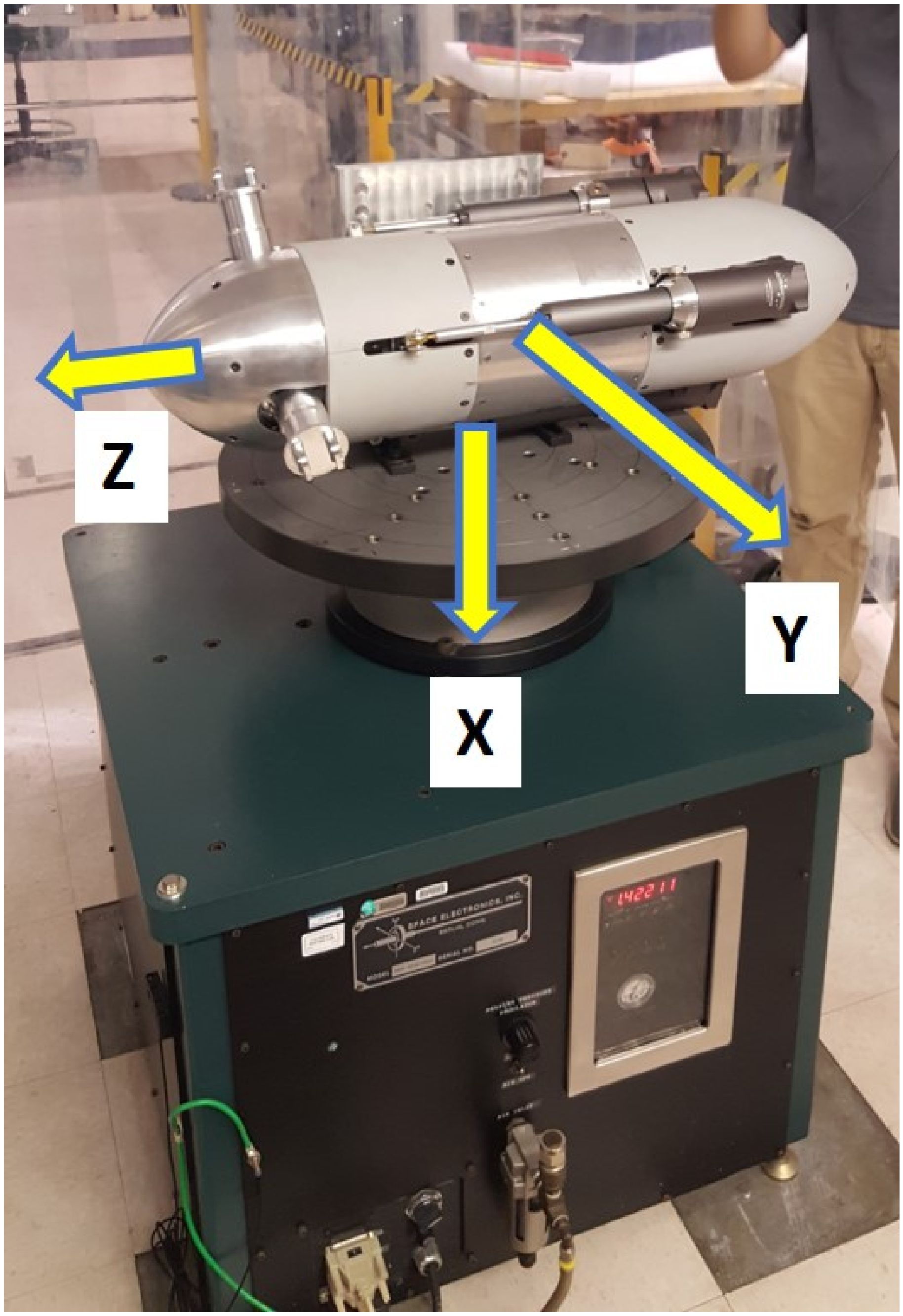

Figure 2.7: KSR CG/MOI machine at NASA Langley; Pylon in yaw configuration.

Table 2.3: Wing-pylon frequencies normalized with cruise r.p.m.; MTR r.p.m. shown is Froude-scale r.p.m. for flutter tests.

	V-22	XV-15	Bell 25 ft	Bell M301	MTR
				1/8.89 XV-15	1/5.26 XV-15
Radius R ft	19	12.5	12.5	1.4	2.375
Cruise r.p.m.	333	517	458	1366	1050
Beam per rev	0.53	0.45	0.42	0.38	0.29
Chord per rev	0.80	0.86	0.70	0.66	0.55
Torsion per rev	1.04	1.07	1.30	1.36	0.82

the interface plate were tared out of the final measurements. Table 2.4 shows the final measured properties of the pylon and hub assemblies with CG location with reference to an origin located at the intersection of the center of the shaft axis and wing spar, shown in Fig. 2.9. Table 2.3 provides a comparison of the measured MTR natural wing frequencies with the pylon installed on the wing. The wing frequencies were measured via a rap test and recording the wing strain at the root while the MTR was installed in the US Naval Surface Warfare Center, Carderock Division Subsonic Wind Tunnel. The baseline spar was designed using initial estimates for pylon mass and inertia. The measured values are lower than the initial targets because the pylon components are heavier than a scaled full-scale vehicle.

2.4.2 Electric Motor

The MTR is driven by a Plettenburg NOVA 30 motor connected directly to the rotor shaft. The motor is a brushless DC, water-cooled, permanent-magnet, electric motor. It is contained within the aluminum section of the pylon. The motor operates at 80-140 V,

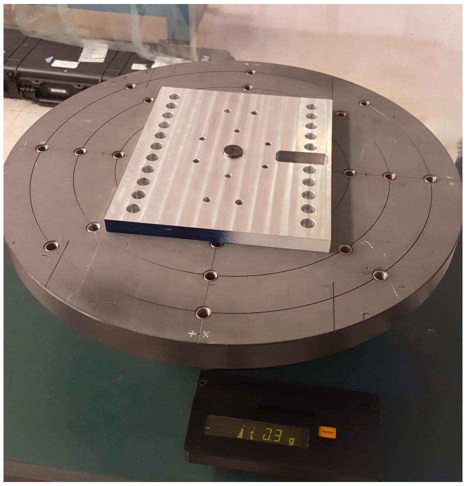

(a) Interface plate in pitch configuration.

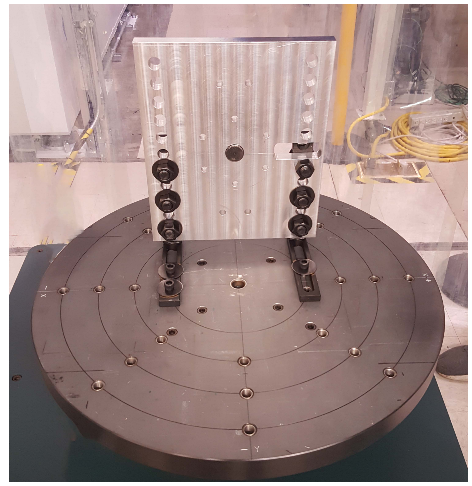

(b) Interface plate mounted to steel brackets for yaw configuration.

Figure 2.8: Tare runs on the interface plate and brackets.

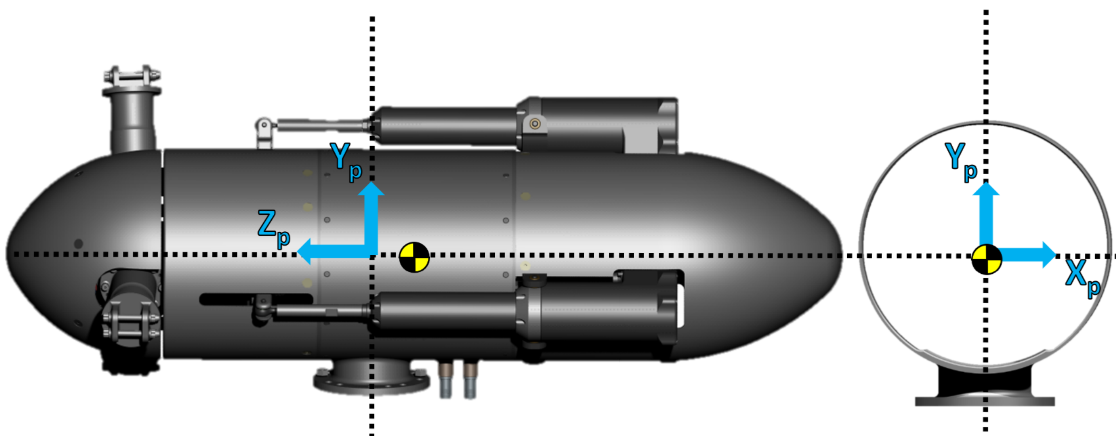

Figure 2.9: CAD rendering depicting the pylon CG location with pylon axes labeled.

Table 2.4: Pylon assembly properties.

Parameter	Value (unit)	$/R$
Mass	32.38 (kg)	
Z_{cg}	3.27 (cm)	4.5%
Y_{cg}	-0.147 (cm)	-0.2%
X_{cg}	0.06 (cm)	0.08%
I_{px}	1.286 (kg-m^2)	
I_{py}	1.289 (kg-m^2)	

has a maximum speed of 5000 r.p.m., maximum torque of 80 Nm (59 ft-lbf), maximum continuous power of 30 kW (22.4 hp), efficiency of 90%, diameter of 20.2 cm (7.56 inches), and total weight of 6.8 kg (15 lb). The three-phase electric cables and water cooling hoses run out of the bottom of the pylon and down through the wing. The motor inverter and control box is located in the tunnel control room and powered by a pair of DC power supplies connected in series to achieve the required voltage and current. The motor controller allows for freewheeling test conditions with no electrical load by driving the motor to a zero-current state. The motor throttle is controlled by the throttle knob on the control box. It can be locked in the freewheeling condition by using the toggle switch for extra safety. The physical emergency stop button used during wind tunnel testing also forces the motor to zero throttle and applies 40% of the electronic brake within the motor.

The motor requires a water flow rate of at least 4 L/min (0.26 gal/min) and a minimum 0.5 bar (7.25 psi) and maximum of 2 bar (30 psi) pressure at the water inlet port. This is achieved by connecting the water inlet hose to a typical wall spigot. The water flows through a pressure reducing valve to limit the pressure in the motor, and monitored with a pressure gauge. It is important to note the change in elevation from the pressure gauge to the motor as the test rig is typically installed one floor above the water supply connection. One meter of height difference corresponds to nearly 0.1 bar (1.5 psi) of pressure loss. After the pressure reducer, the water flows through an analog flow meter that must be oriented vertically to read. Once the water flow is confirmed to meet the cooling requirements, it runs to the motor. After cooling the motor, the water outlet hose is connected to a standard drain. The motor status, including temperature of the motor and the controller, is read through a serial port and monitored through a LabVIEW Virtual

Interface (VI).

2.4.3 Electric Actuators

The swashplate is actuated by three Ultramotion A2 linear actuators. These actuators provide collective and cyclic pitch control by changing the height and tilt of the swashplate by holding a controlled position.

The actuators are controlled by prescribing an analog voltage from 0-10 Volts. An internal PID controller follows the commanded voltage signal as closely as possible. The minimum stroke is limited by a physical stop on the actuators and the maximum stroke (7.2 V) is set in the LabVIEW control software to prevent colliding the swashplate into the rotor hub. For collective pitch control, the collective knob is turned on the control box and all three actuators move in unison, changing the height of the swashplate along the shaft. The swashplate motion translates to a collective root pitch of 17° to 75° at 0.265 R. For a blade with a linear twist rate of -37° per span, $r/R = 0.75$ θ_{75} is -1° to 57°.

In order to provide cyclic control, the joystick serves as a rate controller to command the actuators to tilt the swashplate about two orthogonal axes. Figure 2.10 shows the location of the actuators relative to the X and Y axes of the pylon coordinate system. The actuators are 0.133 m (5.25 in) from the center of the shaft and spaced evenly 120° apart with the first actuator 15 degrees below the X-axis. The change in stroke length required to tilt the swashplate about the Y-axis can be calculated using the sketch in Fig. 2.12. The change in stroke length, A_i for a specified tilt of θ_X is calculated as: $A_i = r \sin\psi_i \tan\theta_X$. Where r is the distance from the center of the shaft to the actuator and ψ_i is the azimuthal location of the actuator. The tilt required for a tilt about the Y-axis, θ_Y is done in a similar way. However, tilting the swashplate directly about the X-axis or Y-axis does not provide a pure θ_{1S} or θ_{1C} cyclic pitch. This is because the δ_3 angle causes the pitch links to be located approximately 73° of azimuth behind the blade. Therefore, in order to provide the correct cyclic controls, the swashplate must tilt about a pair of axes that are rotated 73° clockwise. By superimposing the two tilt requirements about each axis and including the azimuthal offset of the pitch links, the change in actuator stroke to achieve any arbitrary swashplate tilt is:

$$A_i = r\sin\left(\psi_i - 73°\right)\tan\theta_X - r\cos\left(\psi_i - 73°\right)\tan\theta_Y \tag{2.2}$$

The swashplate tilt angles, θ_X and θ_Y, are no longer strictly rotations about the X and Y axes but instead correspond axes that induce cyclic pitch oscillations of the rotor blades, θ_{1C} and θ_{1S}. The relationship from swashplate tilt angles to cyclic pitch can then be approximated from the location of the pitch link connections. The base of the pitch links are located $r_b = 3.0$ inches from the center of the shaft. The top of the pitch links are located $r_t = 2.6$ inches from the pitch axis. Assuming the pitch horn is parallel to the swashplate, then:

$$\theta_{1C} = -\sin^{-1}\left(\frac{r_b \sin\theta_Y}{r_t}\right) \tag{2.3}$$

$$\theta_{1S} = \sin^{-1}\left(\frac{r_b \sin\theta_X}{r_t}\right) \tag{2.4}$$

However, since the MTR has a large collective range, it is not reasonable to assume

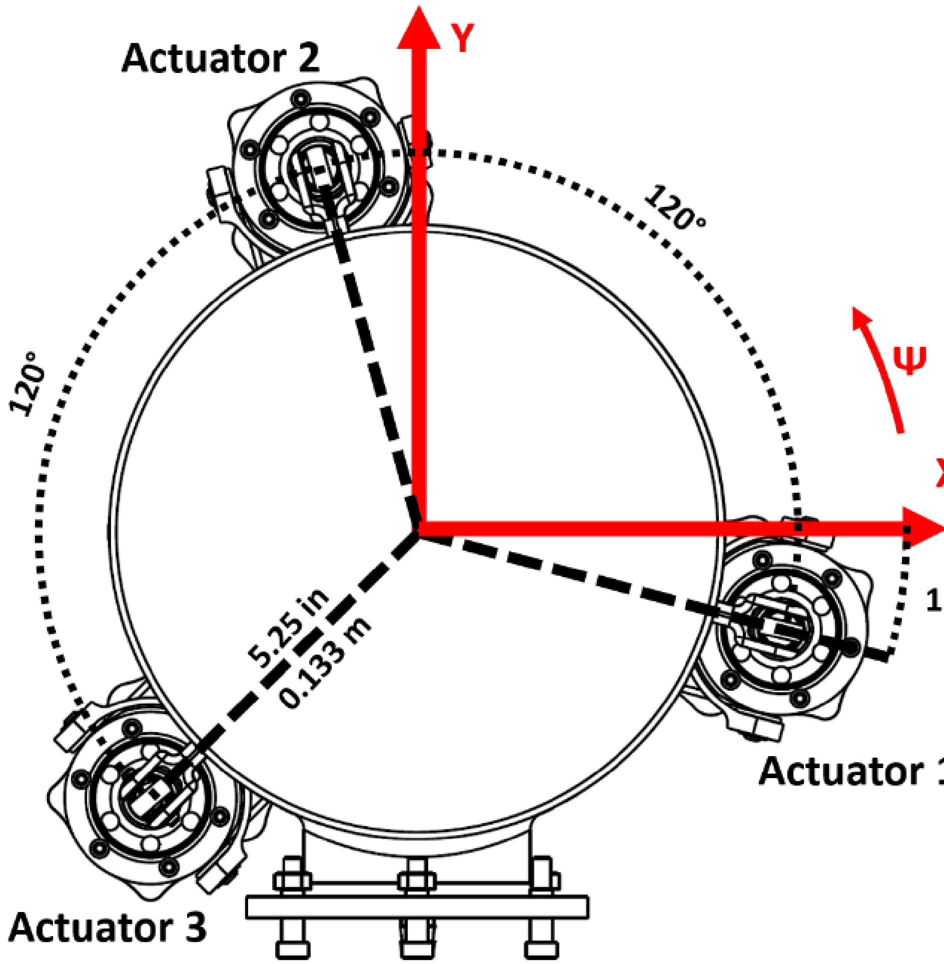

Figure 2.10: Drawing of actuator locations around the pylon looking down from the rotor.

the pitch horn is parallel to the swashplate. For the purposes of trimming the rotor during wind tunnel testing, it is not necessary to calculate the rotor control angles based on the actuator position. It is instead sufficient to use the control box joystick to make precise adjustments to the swashplate tilt angles while monitoring the measured gimbal angle and phase.

In addition to providing rotor trim, the actuators are also used to excite the rig as a part of the whirl flutter test procedure. A sinusoidal input can be added to the current actuator position in order to excite the rig at a specific frequency. Since the perturbation

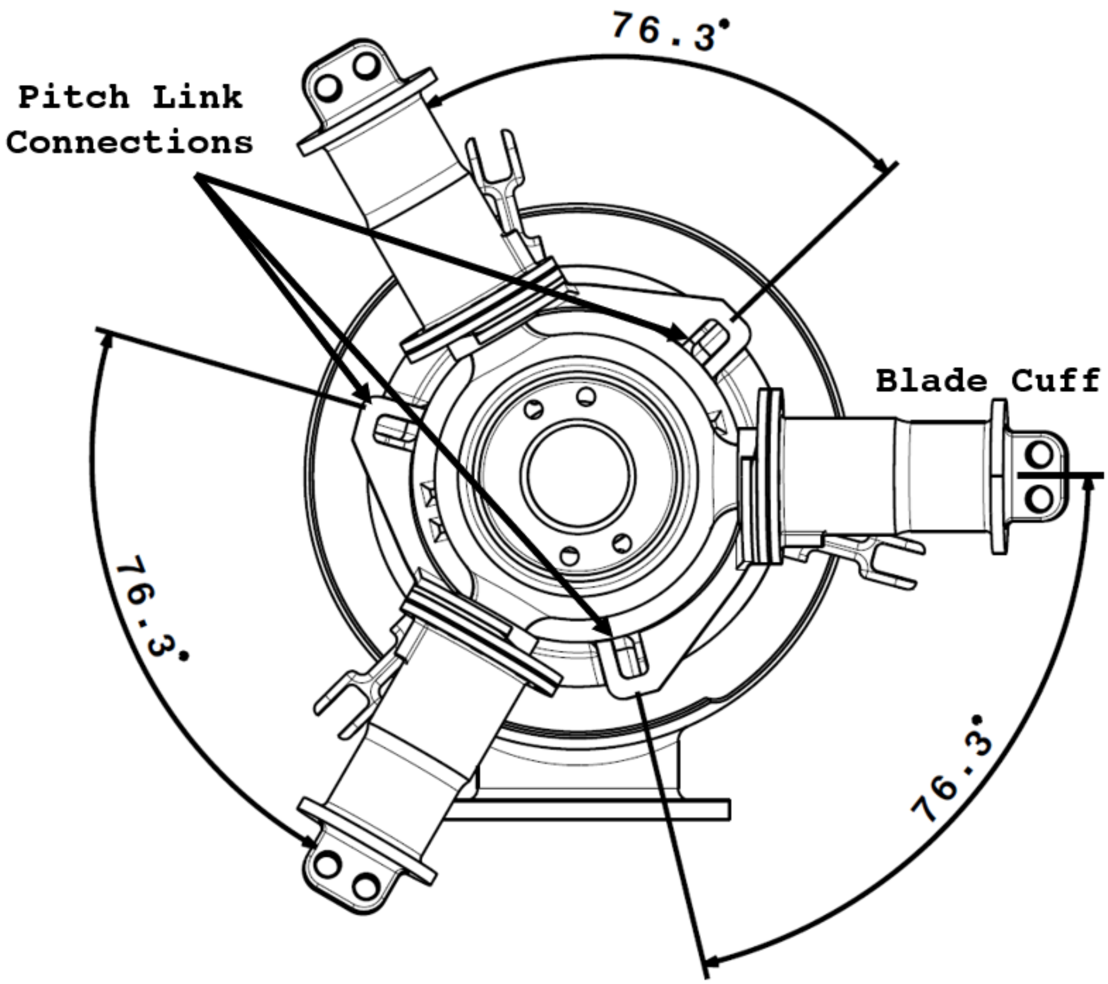

Figure 2.11: Drawing of pitch link locations around the pylon looking down from the rotor.

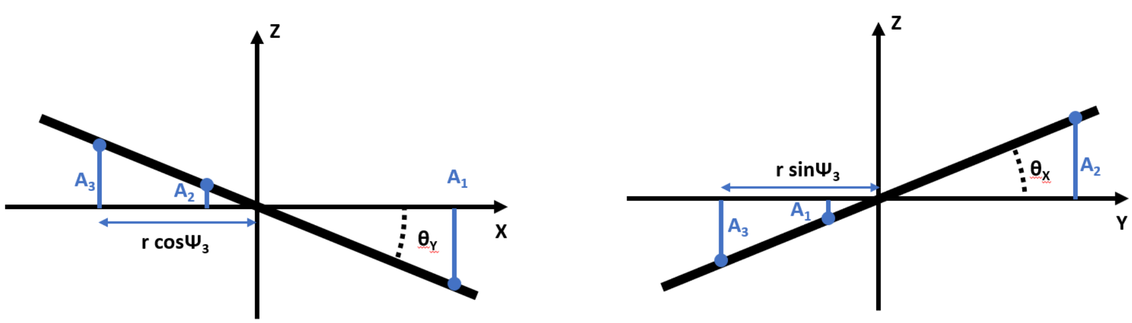

(a) Tilt about Y axis

(b) Tilt about X axis

Figure 2.12: Sketches of the geometry required to calculate the change in actuator length, A_i, for a desired swashplate tilt angle.

is passing from the fixed frame to the rotating frame, exciting the actuators at a /rev results in a blade pitch perturbation of $|a \pm 1|$ /rev. The blade pitching motion generates a perturbation of aerodynamic forces which direction depends on the direction of the swashplate motion. As the aerodynamic force passes from the rotating frame back to the wing in the fixed frame, where the primary frequency is again a /rev. Therefore, to excite the rig at the wing beam, chord, and torsion frequencies, the actuators must be given a sinusoidal input at the wing frequencies.

The flutter actuation controller allows for the selection of collective or cyclic pitch perturbations, actuation frequency, number of cycles, and amplitude. To excite the wing chord bending mode, the collective pitch is perturbed at 0.55 /rev to cause a perturbation of thrust. The beam bending mode is excited by prescribing a longitudinal cyclic oscillation at 0.29 /rev which creates a perturbational force in the X direction. The elastic torsion mode can be excited with the same longitudinal cyclic oscillation but at the wing torsion frequency of 0.82 /rev since the perturbational X-force at the hub also induces a torsional moment about the wing elastic axis.

In order to ensure sufficient bandwidth of the actuators to excite the wing modes, a single actuator was set up with a laser point distance gauge measuring the distance to the actuator shaft. A 1 V amplitude sine wave was input to the actuator and Fig. 2.13 shows the resulting stroke amplitude approximating the pitch change due to the linear displacement of the actuator. The peak to peak change in pitch drops off quickly after 0.2 /rev (3.5 Hz at the nominal 1050 RPM) but remains over 2° past the chord frequency. The limited peak to peak amplitude is thought to be due to the actuator's internal PID controller and could potentially be increased by tuning the gains to achieve a faster rise

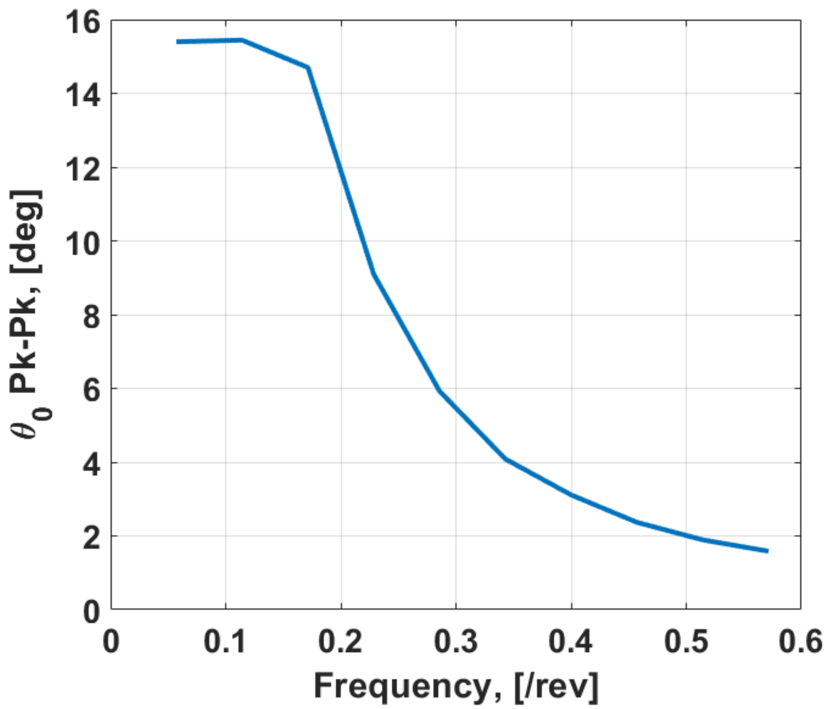

Figure 2.13: Peak to peak collective amplitude due to actuator motion as an excitation frequency increases.

time. During wind tunnel testing at the Subsonic Wind Tunnel, the wing torsion mode could not be actuated either by rap test or pitch perturbations.

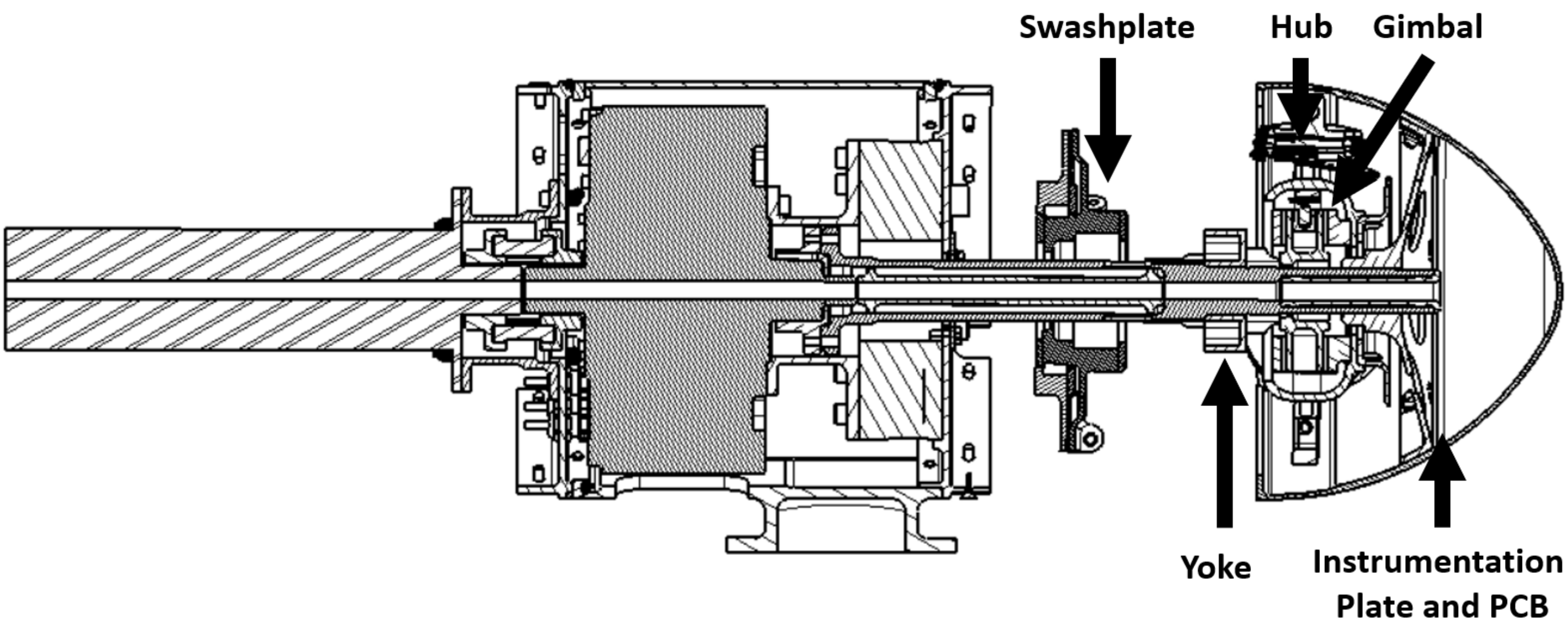

Figure 2.14: Each major component of the rotor assembly labeled on a drawing.

2.5 Rotor Assembly

The rotor assembly is visualized in Fig. 2.14 and the components are laid out in Fig. 2.15. It is comprised of the swashplate, yoke, gimbal, hub with pitch cases, pitch horns, and pitch links attached, and instrumentation plate with mounted printed circuit board (PCB). The gimbal lock plate can be wedged between the hub and yoke to lock the gimbal in place. The gimbal is a spider with bearings along two axes, creating a universal joint for the hub. The hub holds three blades and includes 2°of built in pre-cone. The pitch links are located behind the pitch case to create a -15°angle with the gimbal flap hinge. This angle, known as the δ_3 angle creates a coupling between the blade pitching and flapping motion such that a flap up perturbation of $\Delta\beta$ creates a pitch control input of $\Delta\theta = \tan\delta_3\Delta\beta$.

2.6 Instrumentation

Since the MTR is a research rig, a full suite of instrumentation is installed to monitor hub and pitch link loads, blade pitch, gimbal angle, rotor speed, and azimuth. Each sensor is shown in Fig. 2.16.

2.6.1 Load Cell

The ATI Omega 160 6-axis load cell is located in the aluminum shell near the electric motor and is more easily observed in Fig. 2.6. The static calibration of the load cell was performed by Tsai and discussed in detail in his dissertation [70]. Unfortunately, during testing, there was too much electro-magnetic interference between the motor and

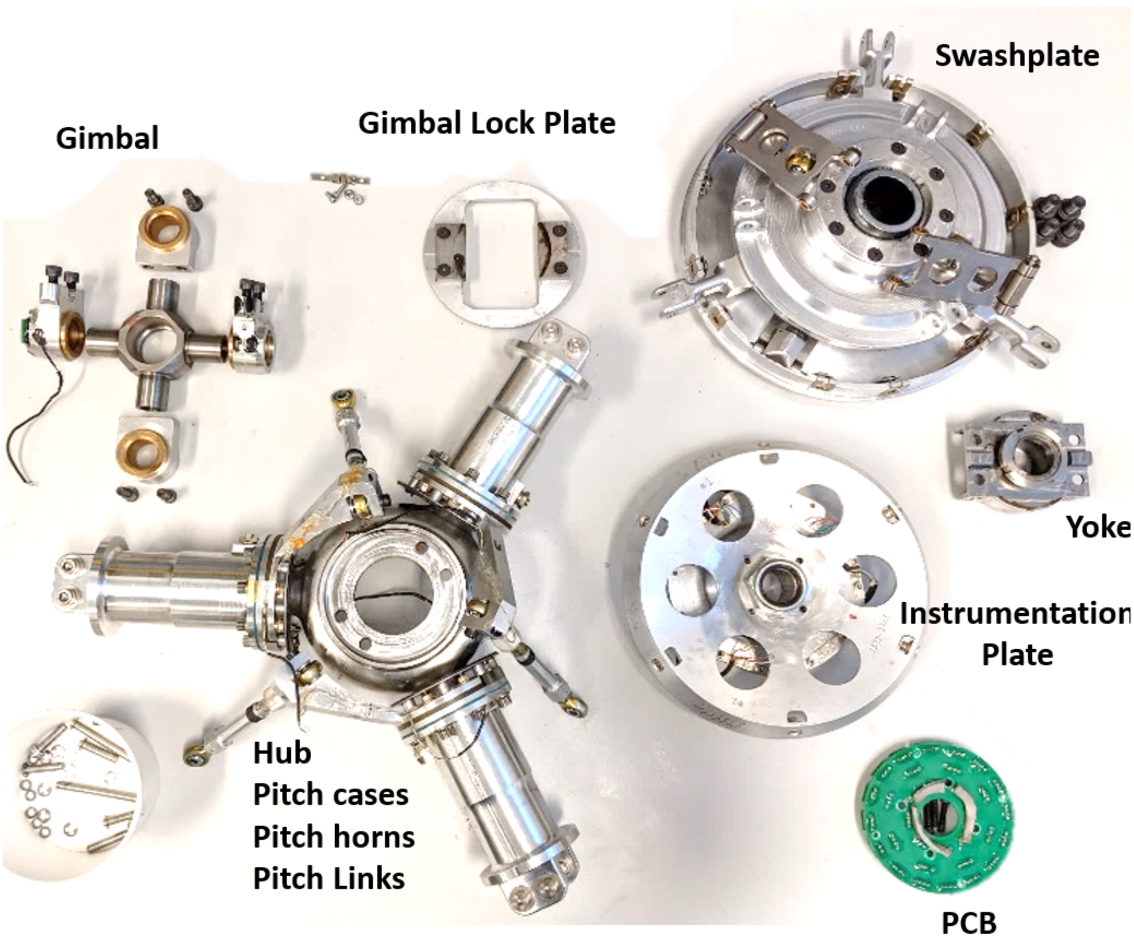

Figure 2.15: Each major component of the rotor assembly laid out on a table.

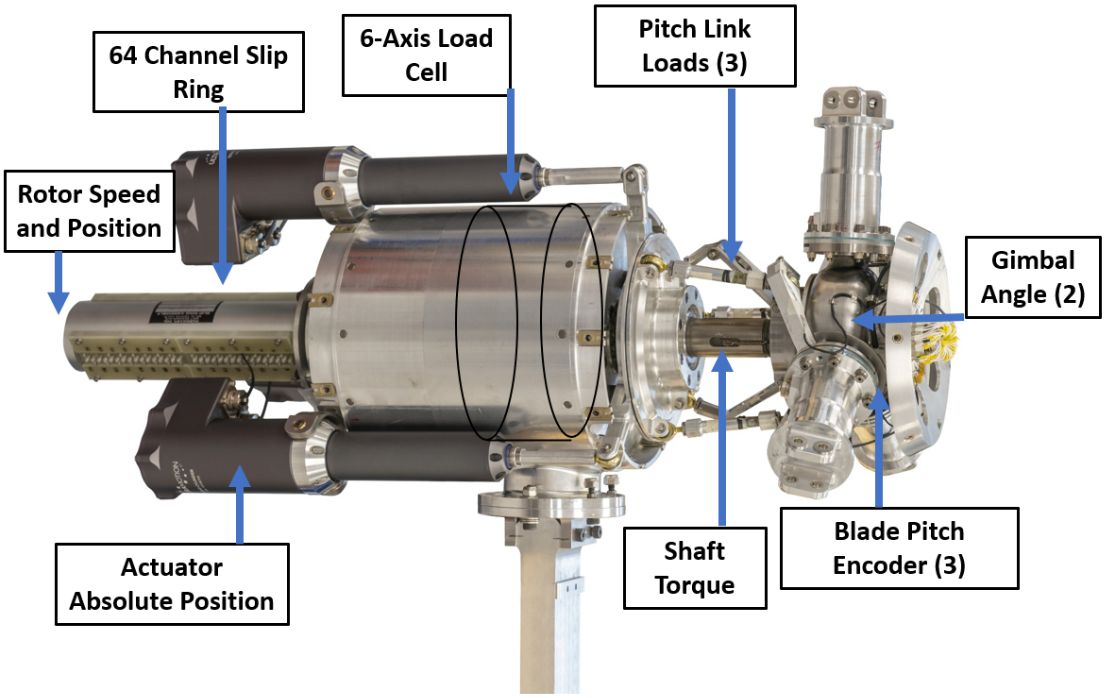

Figure 2.16: MTR with fairings removed and all instrumentation labeled.

the load cell to process meaningful data. This problem is currently being investigated and part of future work. For the flutter tests, the load cell was not essential.

2.6.2 Pitch Link Load

The pitch links have a full strain bridge installed to measure the axial forces due to blade pitching moments. In order to calibrate the strain gauges, the pitch links were suspended with incrementally larger weights hanging below. Figure 2.17a shows the test setup while Fig. 2.17b shows the final calibration results. Each pitch link is similar but the calibration factor differs slightly between them: [-0.5699, -0.6262, -0.5778] lbf/$\mu\epsilon$ respectively.

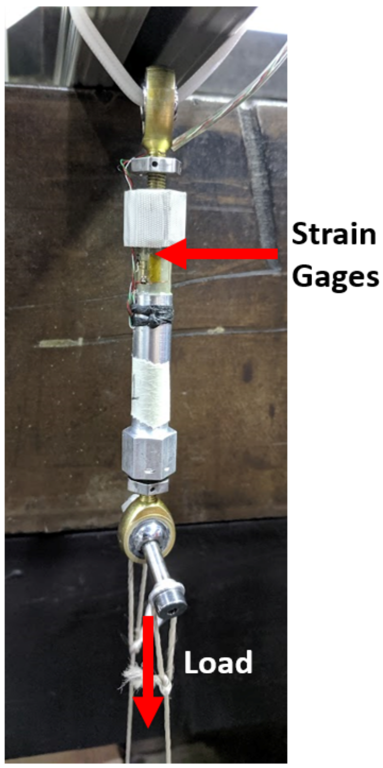

(a) Test setup for pitch link load calibration.

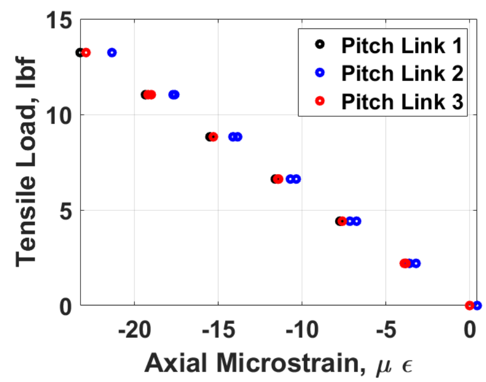

(b) Results of calibration for each pitch link

Figure 2.17: Calibration of pitch link tensile load.

2.6.3 Blade Pitch

The blade pitch is measured with a magnetic rotary encoder. The encoder is mounted to the rotor hub with a magnetic track placed on the pitch case. The magnetic track has pulses placed every 0.01153° which are read by the encoder. This provides highly precise pitch measurements relative to the initial position, but there is no absolute reference point inherent to the magnetic track. Therefore, an initial angle must be used as a reference and the LabVIEW VI must be started in this initial angle in order to measure the blade pitch. The initial angle is defined when the actuators are at the minimum stroke length and a pitch-up torque has been applied by hand to the pitch cases to remove any free play. The initial angle of each pitch case is measured individually using a digital inclinometer while the rig is oriented vertically and the gimbal locked. This initial reference is used for all pitch measurements.

Additionally, the pitch of each blade cuff was measured as the swashplate traveled incrementally from maximum pitch to minimum pitch and returned back to maximum pitch. Figure 2.18 shows the difference between the true angle, measured by an inclinometer at the blade cuff, and the reading from the blade pitch encoder. The results show that the difference between the true angle and reported angle maintains a linear relationship over the sweep of collective angle. Additionally, minimal backlash is observed between the forwards and backwards sweeps.

Ultimately, the actual blade root angle differed from the angle of the pitch case due to slight differences in the fabrication of the blade root. Thus, the reading on the pitch encoder was not the true blade root pitch. The discrepancy is due in part to the tolerances

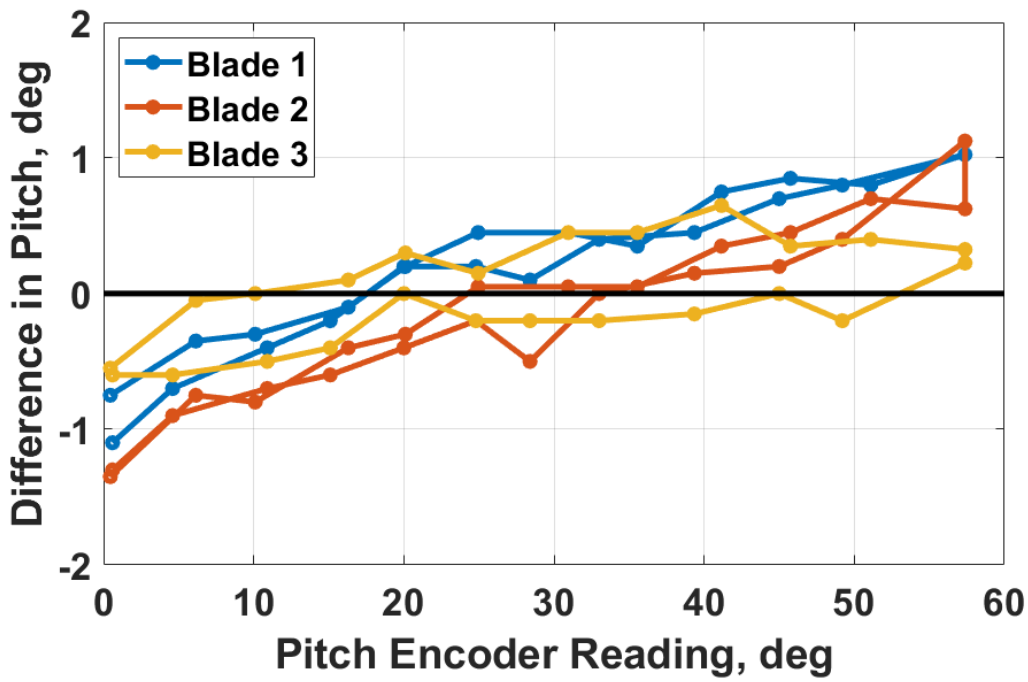

Figure 2.18: Difference between measured root cuff angle and pitch encoder reading.

of the fabricated root insert as well as the fact that the root insert is placed by hand into the blade spar. In order to account for the discrepancies, a series of measurements were taken on each blade used for wind tunnel testing. With the MTR mounted vertically and the gimbal locked, the blade pitch was measured at the blade cuff, $0.5R$, and $0.75R$ for each blade. Although each individual blade had its own variations, an averaged value from the entire blade set is used. Baseline blade set 1, fabricated by Morin [71], requires an average offset of 0.4°. Baseline blade set 2, fabricated by Akinwale requires an offset of 2.1°. The swept-tip blades, fabricated as part of this thesis, require an offset of 0.2°.

2.6.4 Azimuth Sensor

The rotor rotational speed and azimuth is measured using a hall effect sensor and diametrically magnetized magnet placed on the back of the slip ring as shown in Fig. 2.20a.

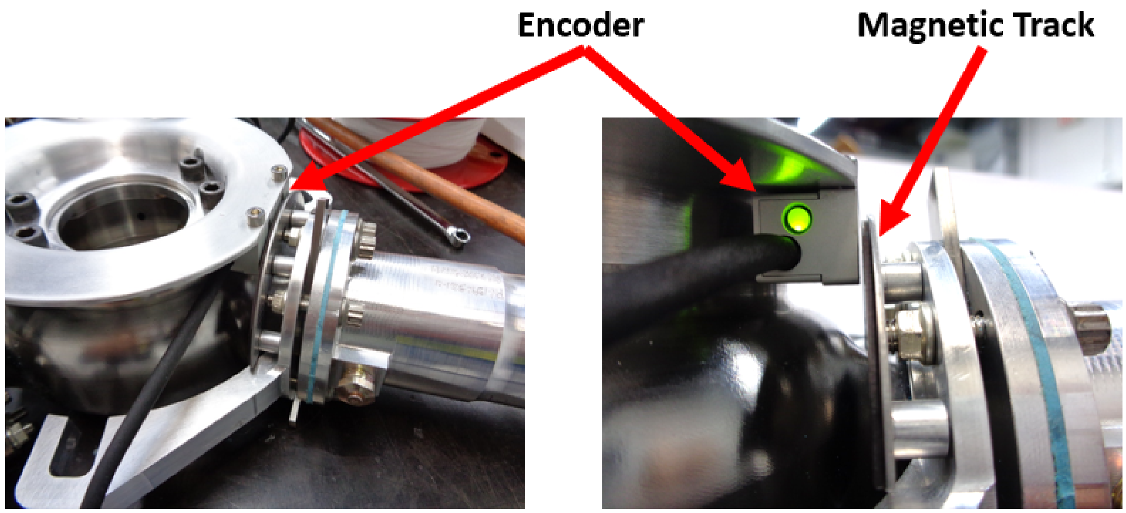

Figure 2.19: Close-up view of the rotor hub with pitch encoder labeled.

The Melaxis rotary position sensor senses the absolute angular position of a magnetic field in the plane of the board and is mounted in the fixed frame. A diametrically magnetized magnet is a magnet whose poles are oriented across the diameter instead of having a north and a south end of the cylinder. As it rotates, the hall effect sensor outputs an analog voltage from 0.5-4.5 V based on the orientation of the magnet field. Figure 2.20b shows the resulting output of the azimuth sensor with the magnet mounted on a CNC mill as it rotates at 2100 RPM. The rotor speed is calculated from a LabVIEW VI which measures the width of the saw-tooth pattern, representing the time for a single revolution.

2.6.5 Gimbal Angle

The gimbal angle measurement uses the same hardware as the azimuth sensor except there is one mounted on each axis of the spider as depicted in Fig. 2.21a. In order to map the output analog voltage to the corresponding axis tilt, each sensor needed to be calibrated. With the hub mounted vertically, a digital inclinometer capable of measur-

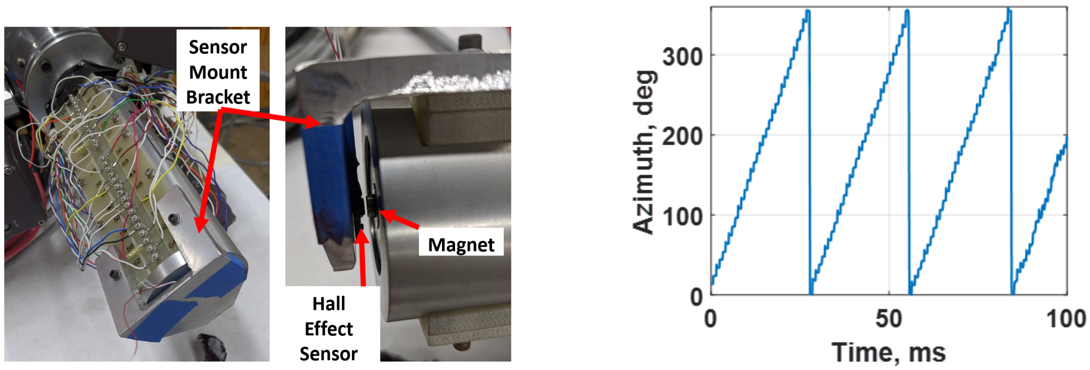

(a) Installation of the azimuth sensor.

(b) Results of a verification test of the azimuth sensor.

Figure 2.20: Hall effect sensor to measure rotor speed and azimuth.

ing both tilt angles simultaneously was placed on a flat portion of the hub. As the hub was statically tilted between level and maximum gimbal angle, the sensor voltage was recorded as shown in Fig. 2.21b. This provides the gimbal angle of the hub about two orthogonal axes in the rotating frame, θ_1 and θ_2. The angles the rotor disc tilts in the fixed frame are β_{1C} and β_{1S}. Since the spider is installed with an angle of -46.25° to the first pitch cuff, the cyclic flap angles can be calculated from the θ_1, θ_2, and the current azimuth, ψ:

$$\beta_{1C} = -\theta_1 \sin(\psi - 46.25) - \theta_2 \cos(\psi - 46.25) \tag{2.5}$$

$$\beta_{1S} = \theta_1 \cos(\psi - 46.25) - \theta_2 \sin(\psi - 46.25) \tag{2.6}$$

There is no sensor to measure the coning angle, β_0. This measurement is difficult, and almost impossible, as the coning blade motion sees a hingeless hub which is very stiff. Measuring it would require camera sensors on the wind tunnel capable of tracking the blade tip.

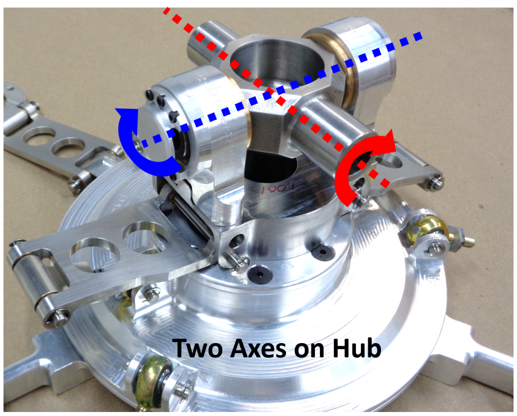

(a) Depiction of the two axes the gimbal angle is measured about.

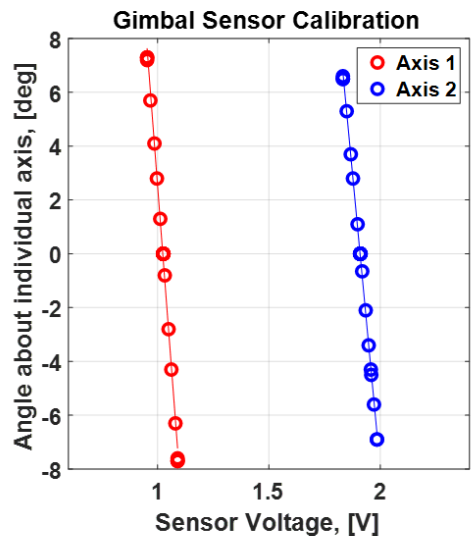

(b) Calibration of the two gimbal sensors.

Figure 2.21: Hall effect sensor to measure hub gimbal angle.

Chapter 3: Composite Blade Design and Fabrication

This chapter describes the design and fabrication of the composite tiltrotor blades. It covers the details of the blade geometry including airfoil section, planform, and geometric twist. Next, the design process of the blade cross-section and final results are described. The tip section of the swept blade does not have a spar and discussion is provided for the rationale. The chapter concludes with a detailed description of the fabrication process for the straight blades and additional steps required for the swept-tip blades.

3.1 CAD Geometry

There are three distinct blade geometries that make up the family of blades developed in this work. The blades are shown in Fig. 3.1.

The blades are designed to have a uniform cross section and still maintain similarity to previous tiltrotor blades. Each blade is comprised of a uniform VR-7 airfoil cross section. The trailing edge of the blade has been modified slightly to include a small tab for ease of manufacturing. The first blade, Fig. 3.1, is the baseline blade which has a straight quarter chord and each section is twisted -37° over the span. High twist is necessary for tiltrotor blades due to the high inflow experienced during cruise. The next blade, Fig. 3.1b and referred to as the untwisted blade, is also straight but untwisted and is used only for structural property measurement. The final blade geometry, Fig. 3.1c and referred to as the swept-tip blade, is twisted and adds a tip sweep of 20° starting at 80% radius. The airfoil section and geometric twist for the swept-tip are defined in reference to the swept quarter-chord line. The planform and cross section for the straight and swept-tip blades are shown in Fig. 3.2.

The swept-tip blade planform has three distinct sections. First is the straight section, which is identical to the baseline blade and extends to 80% R. Next, there is a rounded transition region. It follows a circular arc of 20° because a sharp corner cannot be fabricated accurately and can lead to local ply separation. Finally, the swept region extends from the end of the transition region to the blade tip at an angle 20° backwards from the pitch axis. The angle of 20° and length of 20% radius was selected based on the results of [45, 63] which demonstrated that 10°- 20° of backward sweep over the outer 15-20% of the blade has the strongest effect on wing damping, without leading to other potential instabilities.

In the transition and swept regions, the linear twist rate is defined with respect to the local quarter-chord line. Additionally, the twist in the transition region must be reduced to ensure a clean transition at the trailing edge of the airfoil as it sweeps around the arc. Figure 3.3a shows the trailing edge of the transition region if the same linear twist were to be forcibly maintained. Figure 3.3b shows the final design. A linear twist rate leads to large curvature at the trailing edge and could lead to ply separation and should be avoided. Therefore, the twist in the transition region has a reduced twist rate. The designed twist distribution is listed in Table 3.1 and shown in Fig. 3.4 with markers indicating the locations of prescribed twist angles.

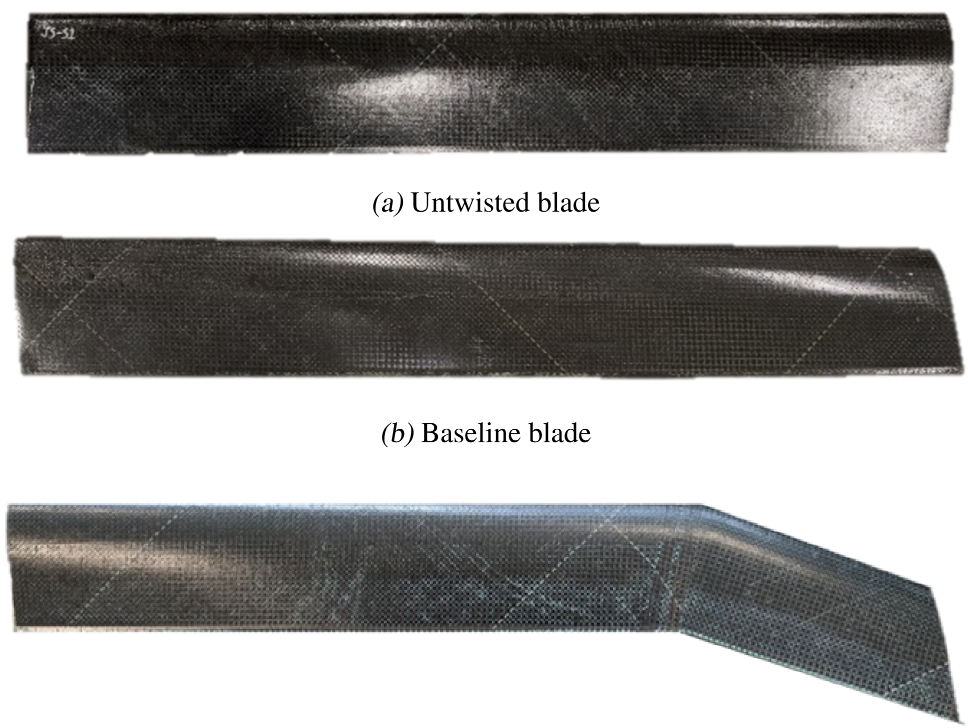

(a) Untwisted blade

(b) Baseline blade

(c) Swept-tip blade

Figure 3.1: The family of blade geometries designed and built for testing on the MTR.

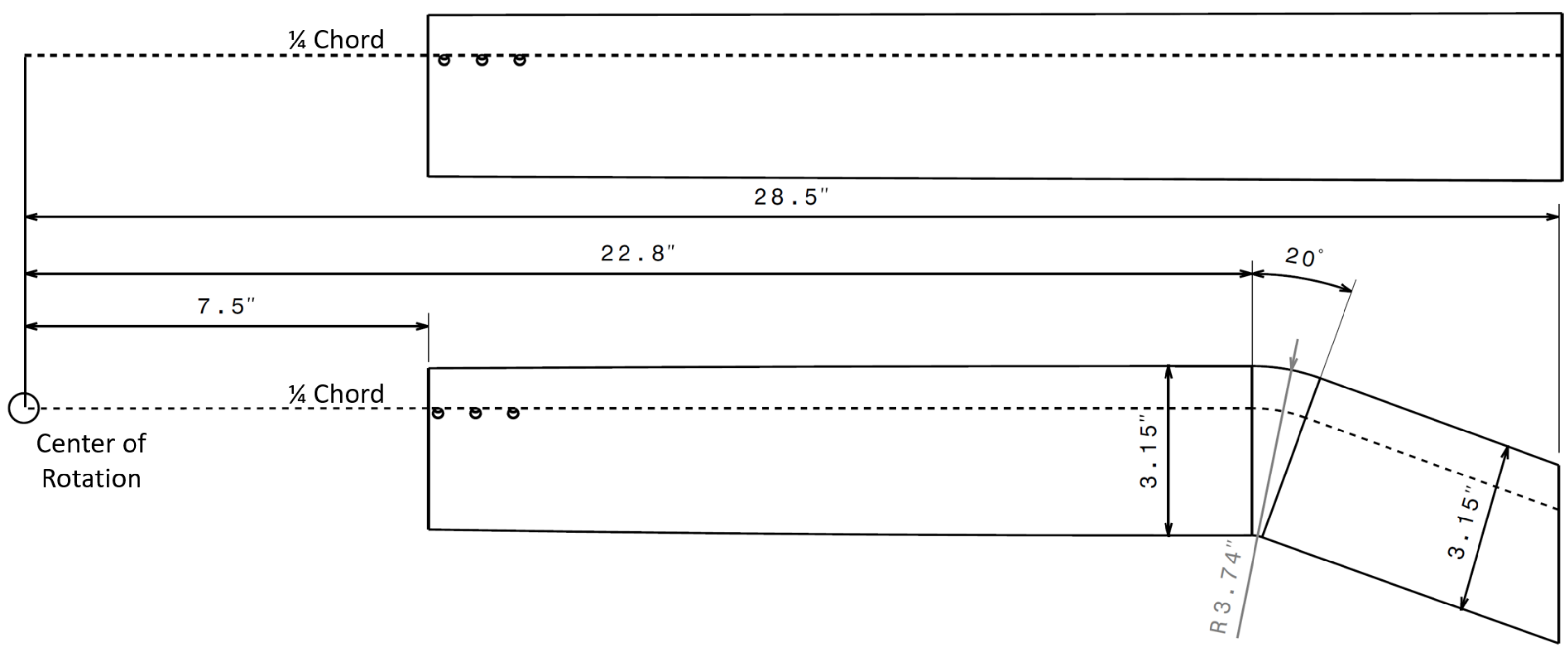

Figure 3.2: Planform dimensions of the straight and swept-tip blades. Dimensions in inches.

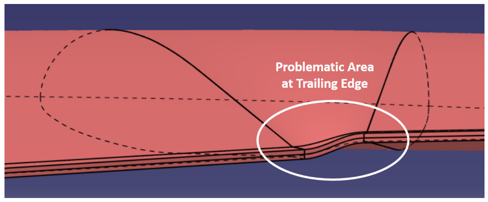

(a) Constant linear twist

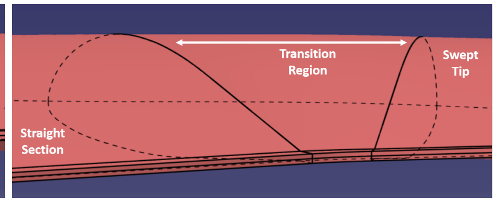

(b) Designed twist

Figure 3.3: Views of the trailing edge of the transition region with different twist distributions.

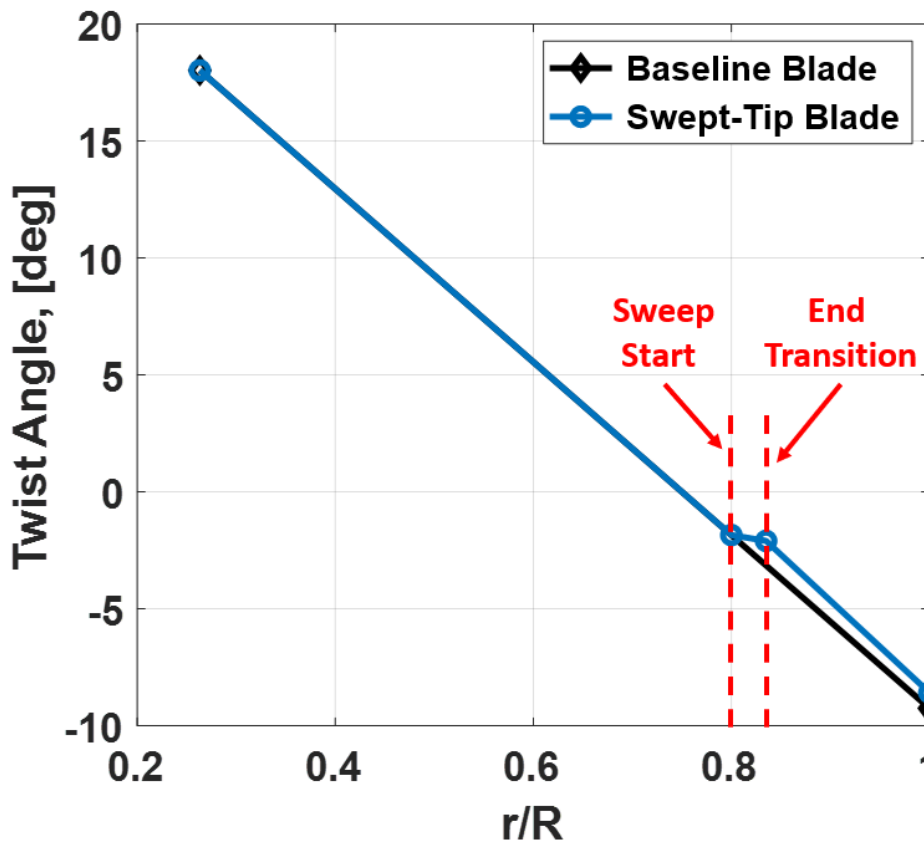

Figure 3.4: Geometric twist of the baseline and swept-tip blades.

The geometric twist is the twist of the airfoil about the chord line. Thus, the aerodynamic twist is the geometric twist. As a part of the cross section design, the spar is also designed and fabricated to follow the same twist. Thus, nominally, the structural twist is also the geometric twist. Strictly, the structural twist is the twist of the principal axes of the cross section. Because the airfoil is not symmetric, the axes will not in general

Table 3.1: Geometric Twist Distribution

r/R	θ, deg	
	Straight	Swept-Tip
0	–	–
Blade Root: 0.265	18	18
Sweep Start: 0.800	-1.85	-1.85
Transition End: 0.835	-3.15	-2.10
Blade Tip: 1.000	-9.25	-8.59

coincide with the chord axis. It is difficult to extract the principal axes at this scale and no such attempt will be made. It is expected that this discrepancy will be made negligible compared to the high twist of the blades.

3.2 Cross-Section Design

While the MTR and the rotor blades are not designed to match any specific aircraft, the 1/5.26 Froude-scale XV-15 blade properties are used as loose targets [44]. The Froude-scale rotational speed is 1050 RPM. To achieve the scaled cross-section properties, an in-house 2-D sectional analysis, SectionBuilder [72], was used to parametrically evaluate the cross section. SectionBuilder takes the airfoil shape, skin thickness, spar geometry, and location of leading edge weights to automatically generate the 2-D triangular mesh shown in Fig 3.5. Then, applying the specified material properties, the 6×6 stiffness matrix for the cross-section are calculated. The material for the blade skin and spar was donated by The Boeing Company for this work and the skin was fixed at 1 ply. Then the design study could focus solely on the spar geometry. A D-shaped spar was selected to be representative of past tiltrotor blades. The two parameters used in the SectionBuilder study are the number of plies in the spar, varying from 1 to 5, and the total length of the

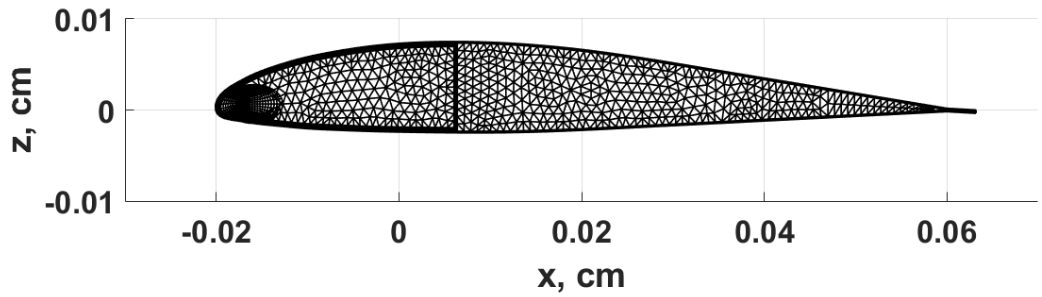

Figure 3.5: Mesh generated by SectionBuilder for cross-section analysis.

D-shaped spar as a percentage of chord length. The results of the study, seen in Fig. 3.6, show that with the material used in the blades, it is not possible to match the chord stiffness target. Since the rotor response is primarily in flap, the normal stiffness target must be maintained. Therefore, a 2-ply spar ending at 33% chord was selected to at least match the target normal stiffness while achieving the lowest chord stiffness possible. The cross-sectional center of gravity (c.g.) is placed near 25% chord using $^{9}/_{64}$-in tungsten-carbide leading edge weights. The final cross-section design is shown in Fig. 3.7.

3.3 Swept-Tip Cross-Section

The cross section of the swept-tip is comprised of the foam core and blade skin. The spar core and leading edge weights do not extend into the swept or transition portions of the blade as shown in Fig. 3.8. Extending the leading edge weights into the swept region would cause an inertial coupling that might oppose the negative aerodynamic coupling introduced by the swept-tip and reduce its potential effectiveness. The spar is not necessary in the swept region and is avoided to prevent additional complexity to the structure

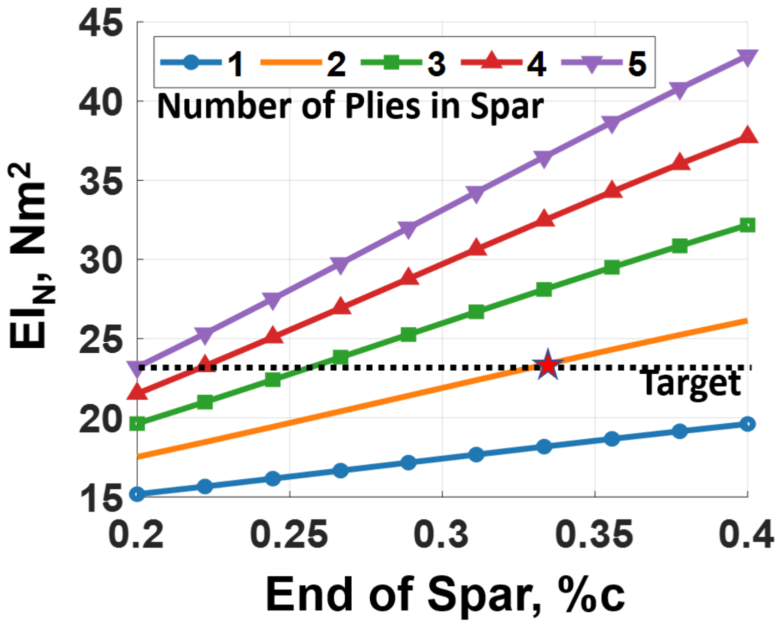

(a) Normal bending stiffness

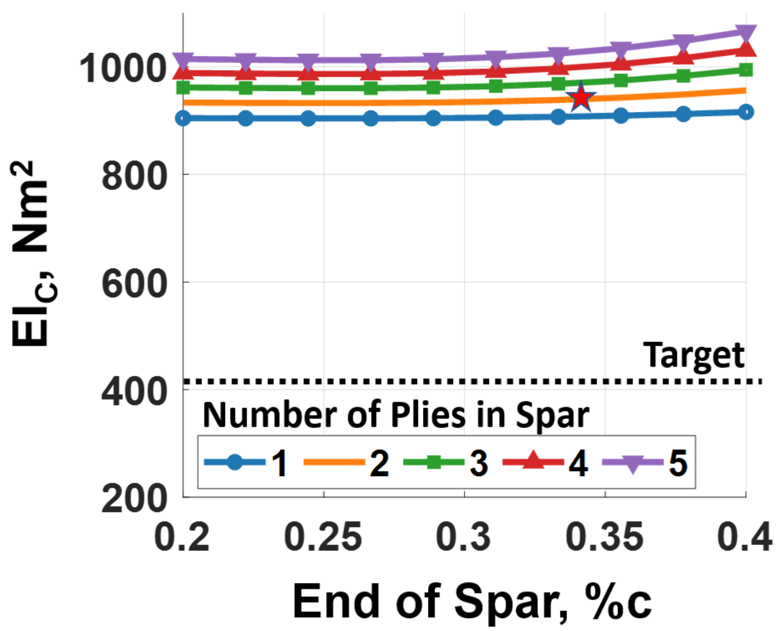

(b) Chord bending stiffness

Figure 3.6: Variation of bending stiffness for the blade cross section due to parametric changes to the spar width and number of plies in the spar. The selected design is depicted with a star.

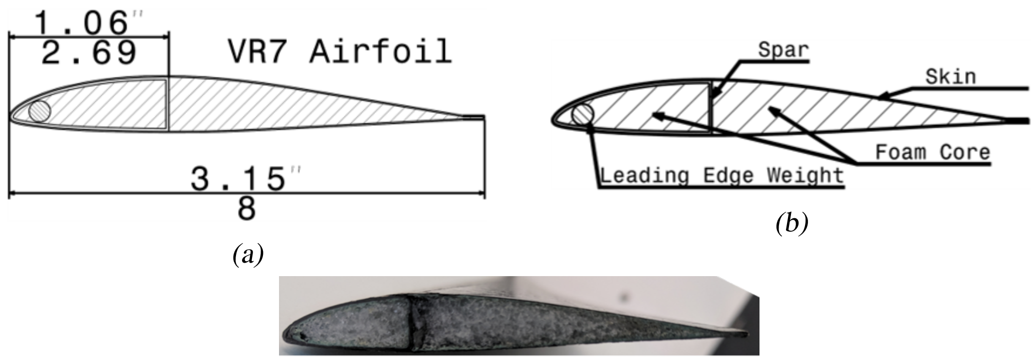

(c)

Figure 3.7: Overview of the cross section for the parametric blade family: (a) dimensions, (b) materials, (c) actual.

and concerns of center of gravity placement for pitch-flap flutter.

3.4 Fabrication Process

Each blade undergoes a similar fabrication procedure, with the exception of the swept-tip blade, which requires additional steps to create the tip.

The fabrication begins by cutting a section of 0.5 inch thick Rohacell IG 31 closed-cell foam to the desired planform shape. The rectangular prism of foam is placed into a two-part mold and compressed into shape by closing the mold. In order to evenly close the mold, the bolts are tightened in a star pattern. Once closed, the blade mold and foam are heated in an oven to 350 °F for 90 minutes so that the compressed foam retains its shape.

After removing the foam from the mold, it is cut into two pieces: a spar core and aft core section using a CNC mill as shown in Fig 3.8. A 1/32 inch end mill cuts the foam core along a straight line 1.049 inches from the leading edge where the back face of the spar will be located. For the swept-tip blade, the spar does not extend the full length of the blade and instead ends 15.3” from the blade root. The spar core is then mounted in the CNC mill with the leading edge oriented vertically. A 9/64 inch diameter end mill cuts 2.5 inches long and 0.34 inch deep slots along the leading edge. Seven tungsten-carbide leading edge weights with 9/64 inch (3.5 mm) diameter and 2.5 inch (6.3 cm) length were installed along the straight blade spar. Five leading edge weights were installed along the swept-tip blade with the same spacing. The leading edge weights are wrapped in a single layer of film adhesive and placed in slots of the spar. The root insert is machined using the CNC mill to match the upper surface of the blade, drill the three bolt holes, and cut it to the final size. The root insert is wrapped in film adhesive then placed in the corner of the spar core, which places the bolt holes along the quarter-chord line.

The spar core with leading edge weights and root insert in place is seen in Fig. 3.9a. Figure 3.9b shows the spar then wrapped in a layer of film adhesive. The aft core is wrapped in a single layer of film adhesive as seen in 3.9c that requires similar steps to the application of the skin detailed in the next paragraph. Then two layers of $\pm 45°$ IM7-8552 woven carbon fiber pre-preg fabric are carefully wrapped around the spar core to ensure no air pockets or wrinkles are present. The spar as it is being wrapped in carbon fiber is shown in Fig 3.9d. The spar is then butted against the aft core to complete the internal structure of the blade as shown in Fig. 3.9e.

The skin around the swept-tip requires additional fabrication steps. It is impossible to wrap the prepreg fabric around the airfoil and sweep at the same time without wrinkling or cutting in the fabric. The fabricated blade places the cut at the start of the swept region and rotates the fabric to be in line with the swept axis. This ensures that in the local frame, the fiber weave is $\pm 45°$ instead of an unbalanced $+65°/-25°$ that would occur

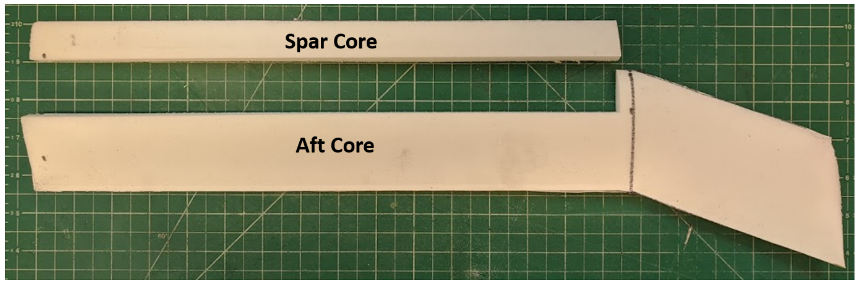

Figure 3.8: Spar and aft cores of the swept-tip blade.

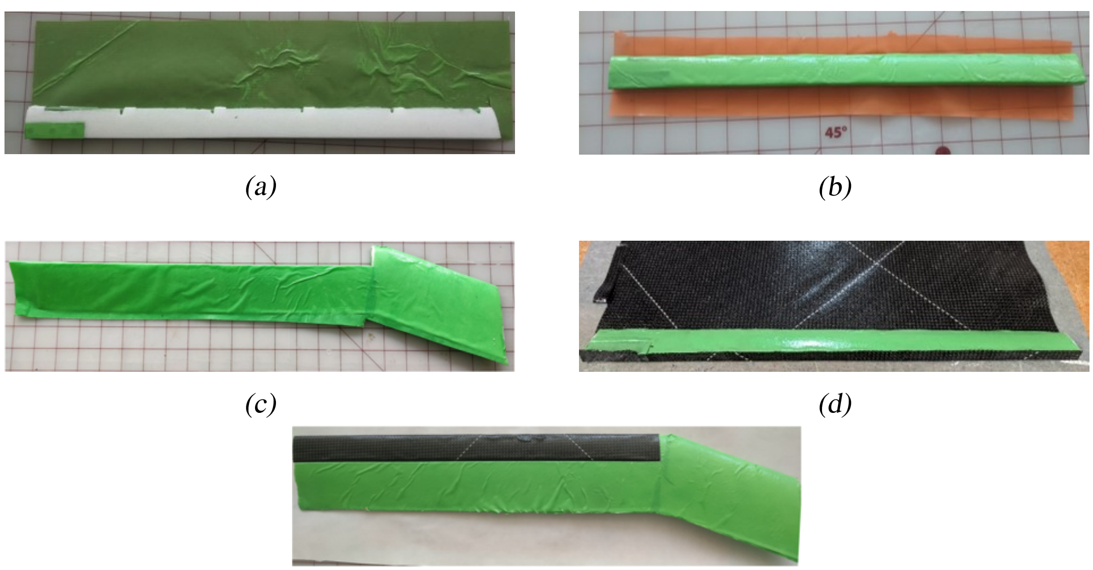

(a) *(b)*

(c) *(d)*

(e)

Figure 3.9: Fabrication steps for the spar of the swept-tip blade.

without this rotation. However, this cuts radial fibers that carry the centrifugal load. For this reason, an additional wide strap is placed over the seam to create a lap joint and ensure load transfer between the straight and swept regions. Fig. 3.10 shows the process in detail. It consists of five steps: (a) the skin fabric is cut to shape using an aluminum cutout template, (b) the internal structure of the blade is placed with the leading edge on the centerline, (c) the end is rotated to align with the swept leading edge, (d) both straight and swept portions are tightly wrapped around the leading edge of the airfoil, and (e) an additional 0.5 inch strap is placed over the seam. Similar steps are taken for the film adhesive wrap around the aft core and the outer release ply using the template to cut out the required shapes to wrap around the swept-tip as shown in Figs 3.11a and3.11b.

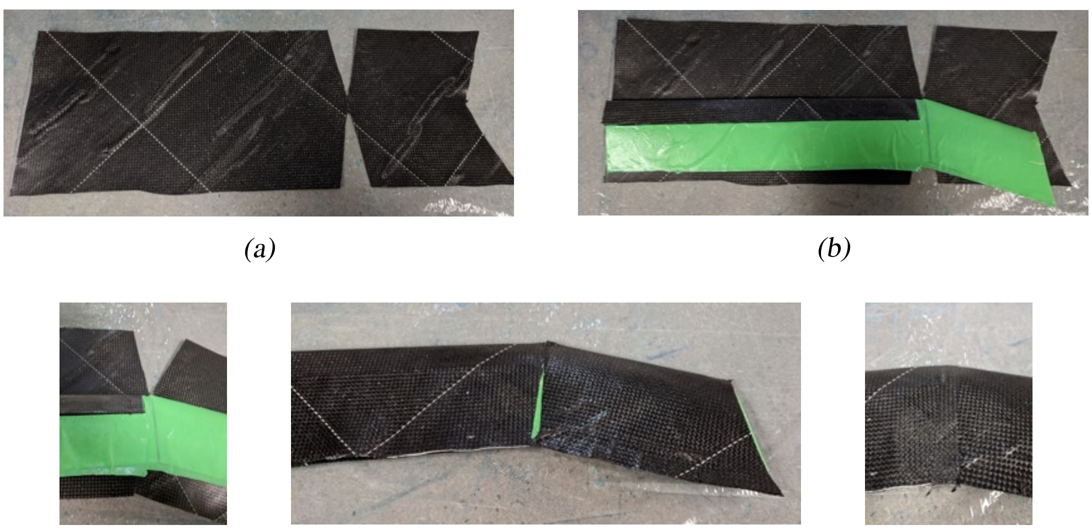

(a) *(b)*

(c) *(d)* *(e)*

Figure 3.10: Fabrication steps for the outer skin of the swept-tip blade.

Once cured, the blade is removed from the mold after it has cooled. The compression of the mold creates flashing along the leading and trailing edges which is visible in Fig 3.11c. The flashing is removed first with a Dremel tool for a rough pass, then finished with a hand file to achieve a round leading edge and the correct chord length. The next

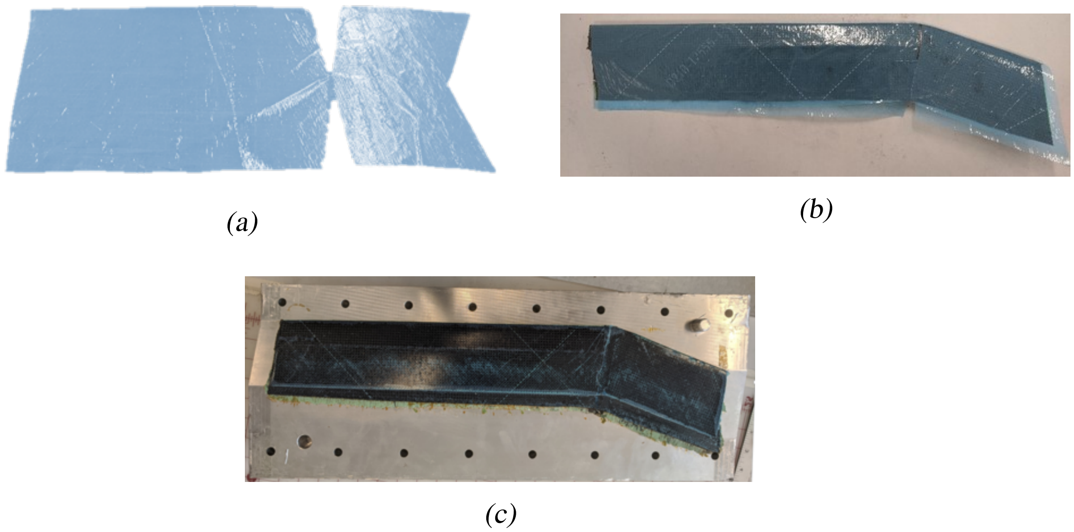

Figure 3.11: Final fabrication steps for the swept-tip blade.

Table 3.2: Weight Distribution

Component	**Mass (g)**	**Percentage of Total Mass (%)**
Leading Edge Foam	4.2	3
Trailing Edge Foam	13.9	9
Leading Edge Weight	51.6	34
Root Insert	12.3	8
Film Adhesive	5.3	4
Spar Fabric	33.4	22
Skin Fabric	30.9	20
TOTAL	152	100

step is to locate the three holes in the root insert and, using a cordless drill and drill bits of increasing diameter, drill holes through the carbon fiber material. Finally, the blade should be trimmed to be 20.63 in. long from the center of the first bolt hole to ensure the proper rotor radius. The completed blade is pictured in Fig 3.12 and Table 3.2 provides a breakdown of the weight of each component.

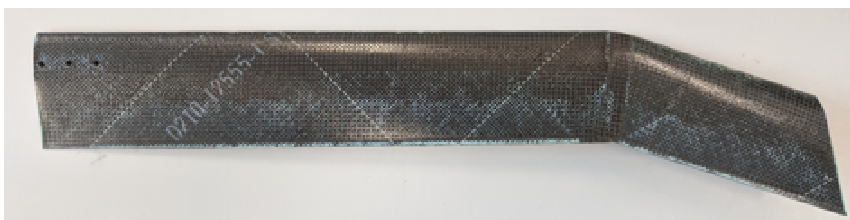

Figure 3.12: Fabricated swept-tip blade.

Chapter 4: Blade Properties

This chapter outlines the measurement of the structural and inertial properties of the blades. The first section provides a brief overview. Afterward, the theory and formulation for making sectional stiffness measurements are presented. The blade stiffness is first measured by a mirror method. The measurements are repeated using accelerometers as tilt sensors for more reliable data. These measurements are performed for bending stiffness in two directions and torsional stiffness. In addition, the blade center of gravity, sectional mass, and moment of inertia are measured. The final section describes the measurement of the blade non-rotating frequencies.

4.1 Overview

In order to predict the behavior of the rotor blades, it is crucial to measure its properties and ensure the finite element model built later matches them. Non-destructive, bench-top tests are performed to measure the blade mass, center of gravity, flap inertia, bending and torsional stiffness, and non-rotating frequencies. A summary of the measured sectional blade properties of the untwisted blade can be found in Table 4.1 as well as the predicted value from the model developed in Chapter 5. The non-rotating frequencies can be found in Table 4.2.

4.2 Stiffness Measurement

The cross-sectional stiffness tests are performed on the untwisted blade to ensure the measured data is as accurate as possible. The high twist of the baseline blades strongly couples the normal and chordwise directions in the global flap and lag axes. Measurements on the twisted blade were attempted, but the results were not of high enough repeatability to be considered reliable, hence were discarded. Instead, a special untwisted mold and corresponding blades were fabricated to serve as a surrogate for all structural property measurements in the normal and chordwise directions.

The bending stiffness of the blade section, EI, is calculated from the measured curvature, w'', and applied moment, M, according to Eqn 4.1 derived from Euler-Bernoulli beam theory. Using this theory assumes that a plane cross section normal to the beam axis remains plane and normal after bending and there is no other cross sectional deformation. These assumptions hold true for a straight blade with a quasi-isotropic layup under small deflections.

$$M = EIw'' \tag{4.1}$$

For a single, uncoupled degree of freedom, w, the EI can be calculated with relative ease where the bending moment is known from the applied tip load, P, and distance from the blade tip to measurement point, a. The bending moment is calculated at the midsection between two points along the blade:

$$M = \frac{P}{2}(a_1 + a_2) \tag{4.2}$$

The curvature is approximated from bending slope measurements at two points:

$$w'' = \frac{w_1' - w_2'}{a_1 - a_2} \tag{4.3}$$

Therefore, Eqn 4.1 can be reformulated as:

$$\frac{P}{2}(a_1 + a_2) = EI\frac{w_1' - w_2'}{a_1 - a_2}$$

$$EI = \frac{P(a_1 + a_2)(a_1 - a_2)}{2(w_1' - w_2')}$$

$$EI = \frac{P(a_1^2 - a_2^2)}{2(w_1' - w_2')} \tag{4.4}$$

Measuring the slope at two points removes any influence from an imperfect clamping condition, which is an improvement over rudimentary tip deflection measurements.

However, the baseline, twisted blade introduces coupling between the flap and lag bending modes. At a single section, the normal and chordwise bending modes are uncoupled, but the twist rotates each section along the blade. So, as one moves along the blade length, the EI in the flap and lag directions vary over the entire span. The coupling is clearly evident in Fig. 4.1. Under a 1 kg load in the chordwise direction, the blade deflects in the chordwise direction but also more than one blade thickness in the normal direction.

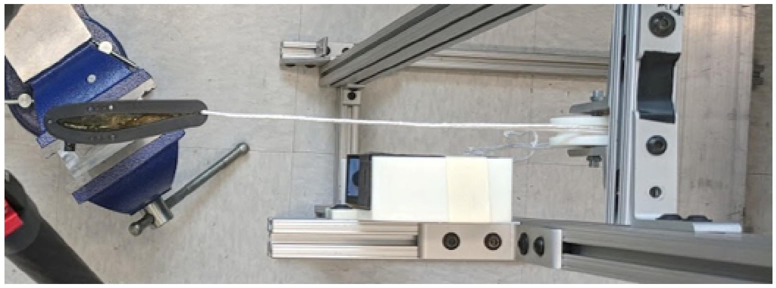

(a) Position of the blade tip with no load applied.

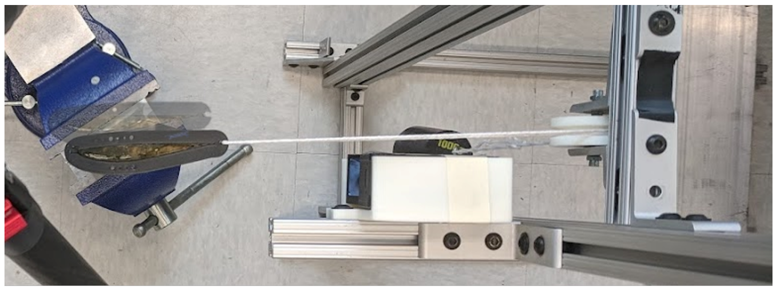

(b) Deflection of the blade tip under 1 kg load overlayed with initial position.

Figure 4.1: Coupled bending deflection of the twisted blade.

Therefore, a 2 x 2 set of equations is required.

$$\begin{bmatrix} M_C & 0 \\ 0 & M_N \end{bmatrix} = \begin{bmatrix} -EI_N & 0 \\ 0 & EI_C \end{bmatrix} \begin{bmatrix} n'' & 0 \\ 0 & c'' \end{bmatrix} \tag{4.5}$$

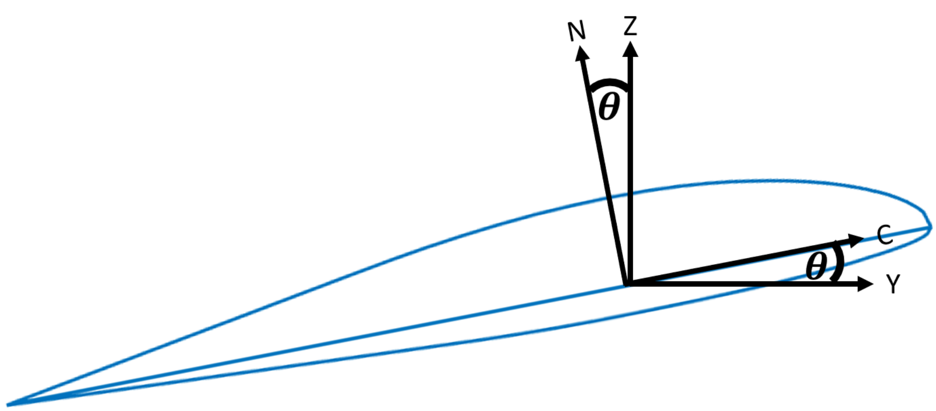

Figure 4.2: Local and global coordinate system for the blade section.

Where N and C denote the normal and chord directions and n'' and c'' are the curvature in those directions. Now during measurement, loads and deflections are measured in the global flap, Z, and lag, Y, directions. Using θ, the angle between the blade section and the global coordinate system shown in Fig. 4.2, the bending moments and deflections in Eq. 4.5 can be written in terms of the global frame:

$$\begin{pmatrix} n'' \\ c'' \end{pmatrix} = \begin{bmatrix} \cos\theta & -\sin\theta \\ \sin\theta & \cos\theta \end{bmatrix} \begin{pmatrix} w'' \\ v'' \end{pmatrix} \tag{4.6}$$

$$\begin{pmatrix} M_C \\ M_N \end{pmatrix} = \begin{bmatrix} \cos\theta & -\sin\theta \\ \sin\theta & \cos\theta \end{bmatrix} \begin{pmatrix} M_Y \\ M_Z \end{pmatrix} \tag{4.7}$$

And so, plugging into Eq 4.5,

$$\begin{bmatrix} \cos\theta & -\sin\theta \\ \sin\theta & \cos\theta \end{bmatrix} \begin{pmatrix} M_Y \\ M_Z \end{pmatrix} = \begin{bmatrix} -EI_N & 0 \\ 0 & EI_C \end{bmatrix} \begin{bmatrix} \cos\theta & -\sin\theta \\ \sin\theta & \cos\theta \end{bmatrix} \begin{pmatrix} w'' \\ v'' \end{pmatrix} \tag{4.8}$$

Thus,

$$-EI_N = \frac{M_Y \cos\theta + M_Z \sin\theta}{w'' \cos\theta - v'' \sin\theta} \tag{4.9}$$

$$EI_C = \frac{M_Z \cos\theta - M_Y \sin\theta}{v'' \cos\theta - w'' \sin\theta} \tag{4.10}$$

These equations for EI_N and EI_C are used to calculate the uncoupled sectional stiffnesses from measurements of flap and lag bending slopes at two points on the blade under a known applied moment in any direction.

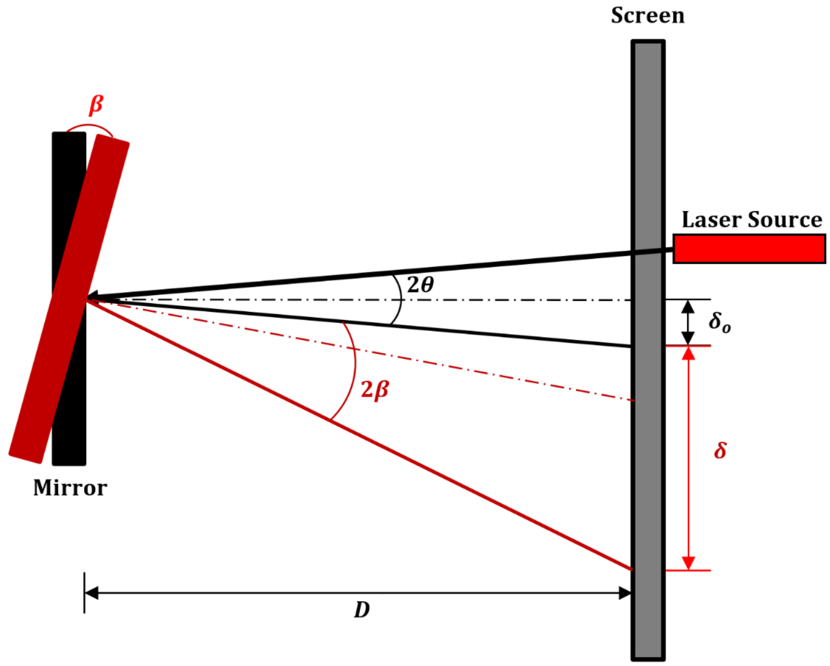

Figure 4.3: Diagram of mirror method theory; red depicts the result after deforming under load.

4.2.1 Mirror Method

The mirror method uses sets of mirrors placed along the blade surface to reflect a laser light. The bending slope is measured from the deflection of the laser along a surface. The technique is derived from the same method performed on the HART I blade set in Ref [73]. Figure 4.3 depicts the geometry of the laser reflecting onto a screen a distance, D, away. The undeflected mirror and laser path are shown in black, where δ_0 is the deflection of the laser with no load applied due to an initial incidence angle, θ. This angle is calculated as:

$$\theta = \tan^{-1} \frac{\delta_0}{D} \tag{4.11}$$

Once a load is applied, the mirror rotates by an angle β, and the image of the laser on the screen then moves an additional distance, δ. The bending angle is calculated as:

$$2\beta = \tan^{-1}\left(\frac{\delta + \delta_0}{D}\right) - \theta \tag{4.12}$$

and the bending slope is simply

$$w' = \tan\beta \tag{4.13}$$

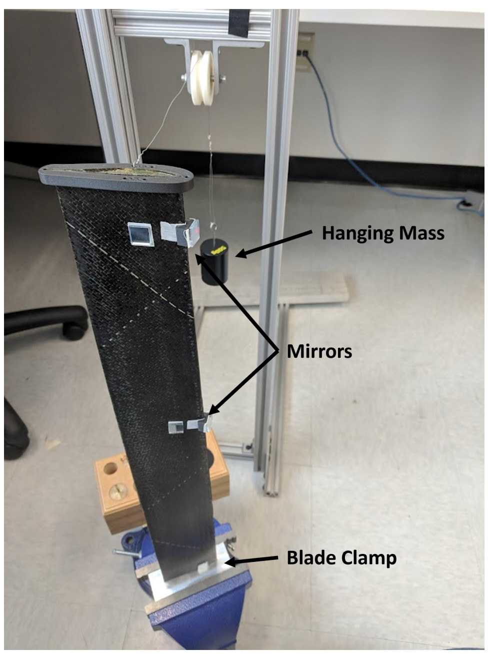

(a) Clamped blade with mirrors mounted and tip load applied.

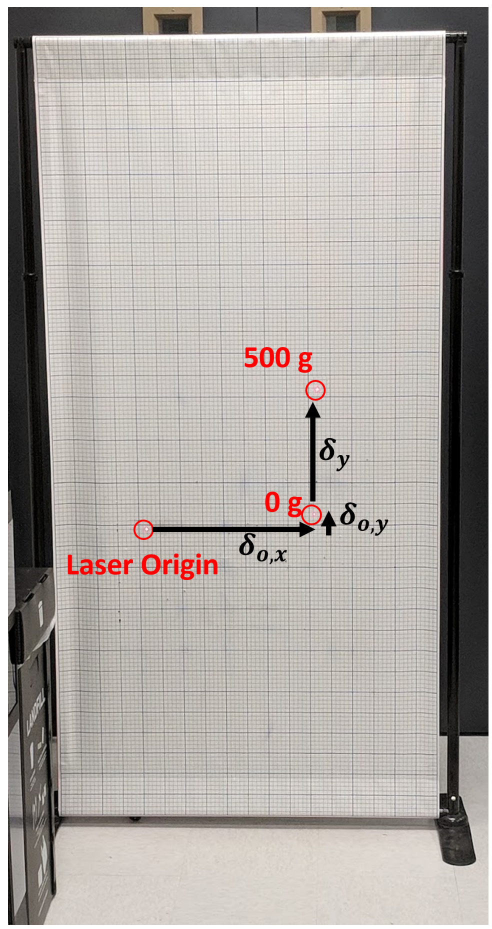

(b) Displacement of the laser reflection under load

Figure 4.4: Experimental setup for mirror method testing.

After multiple iterations and refinement, the final physical setup is shown in Fig

4.4. Measurements were initially performed on the baseline, twisted blade since it was desired to measure the blades that would be installed on the MTR. However, the large twist causes structural coupling of the normal and chordwise bending modes. The blade is clamped in a vertical orientation and load applied to the tip through hanging masses over a pulley. Mirrors are mounted at two points along the blade surface using double-stick tape. Mirrors on the top surface are mounted at the 25% chord location. The mirrors at the leading-edge, placed to measure the chord bending stiffness, are attached to 3D printed grips which conform to the leading edge of the blade. A laser is mounted to a tripod and carefully aimed at one of the mirrors on the top surface of the blade. A large screen with a 1 cm grid is placed in front of the laser and a small hole is punctured to allow the laser to pass through. The grid is used to accurately measure the deflection of the laser image in the vertical and horizontal direction due to either normal or chordwise deflections. Simultaneously, a second laser and screen are setup orthogonally to measure the bending deflection of the mirrors along the leading edge.

Once the two lasers are aimed at one pair of mirrors and the reflection falls on the screen, the test procedure can begin. First, the distance from the mirror to the grid screen is measured using a tape measure. Then, the initial laser image is measured relative to the location of the laser origin (where it shines through the screen) in both vertical and horizontal directions using the grid markings. The 1 cm grid allows for approximation up to 1 mm in precision. These measurements are repeated on both the normal and chordwise screens.

Next, weights varying in mass from 500g to 1 kg in 100 g increments are attached to the blade tip and hung from the pulley in the normal bending direction. For each mass, the resulting position of the laser reflection onto the screens is recorded. The test is typically limited to 900 g of load due to the mirror deflecting out of the path of the laser and no longer able to be measured. Once the full range of tip loads has been applied, the lasers are repositioned to measure the deflection of the next pair of mirrors along the length of the blade. After both sets have been measured for the normal bending load, the entire test procedure is repeated again with the load applied in the chordwise direction. The final result is measurements of the normal and chordwise bending slope at two radial stations under normal and chordwise bending moments, including the coupled effects.

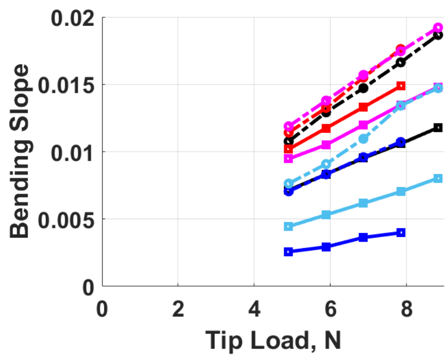

(a) Lag bending due to a lag load.

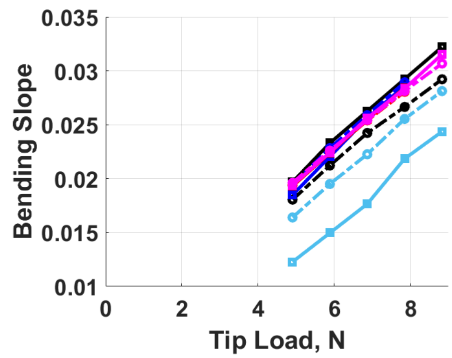

(b) Lag bending due to a flap load.

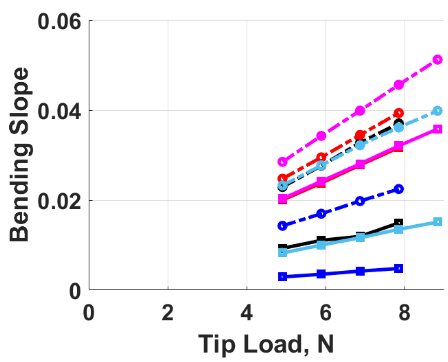

(c) Flap bending due to a lag load.

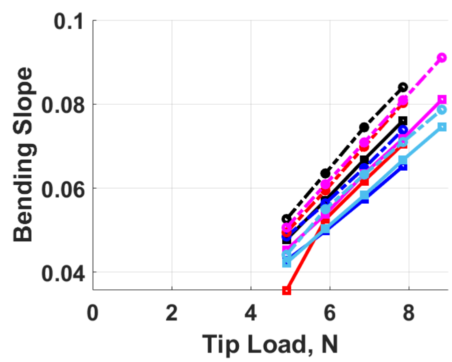

(d) Flap bending due to a flap load.

Figure 4.5: Measured bending slope of each mirror across 5 separate trials.

When performing five trials of the same test with the same experimental setup, the results were found to be non-repeatable. Figure 4.5 shows the measured bending slopes in the flap and lag directions due to flap and lag loads. The dotted line shows the measured slope of the mirror at the blade tip (56 cm from the clamp). The solid line shows the measured slope of the mirror placed 34 cm from the clamp. Each color indicates a different trial that was performed. For a single trial, it is expected for the slope at the tip to be larger and to be increasing at a higher rate than the lower mirror. This should be especially noticeable in Fig. 4.5d where the flap bending due to a flap load causes much larger deflections than in any other direction. However, the solid and dotted lines have quite similar slopes. Additionally, there is so much scatter between each trial that no meaningful conclusion can be made from this data.

In order to acquire more meaningful data, two decisions were made. The first was to fabricate a straight, untwisted blade to eliminate any coupling. The second was to determine an alternative method of measuring the bending slopes since the mirror method was too slow and tedious to troubleshoot and refine.

4.2.2 Accelerometer Method

The new method used to measure the bending slope along the blade utilizes 3-axis accelerometers as tilt sensors to allow for rapid digital measurement. As seen in Fig. 4.10, the accelerometers are placed on the bottom surface of the blade with their x-axis pointed towards the leading edge. Under static conditions, the accelerometer outputs a $1g$ signal in the y-axis, the direction of the Earth's gravitational field. As the accelerometer rotates, the orientation can be calculated from how the $1g$ signal is divided between the three axes using the equations below:

$$\frac{\mathrm{d}n}{\mathrm{d}r} = \frac{g_z}{g_y} \ , \ \frac{\mathrm{d}c}{\mathrm{d}r} = \frac{g_z}{\sqrt{g_y^2 + g_z^2}} \tag{4.14}$$

where g_i is the normalized accelerometer output vector in x, y, z coordinates, n and c are the deflections in the normal and chordwise directions, and r is the spanwise location along the clamped blade.

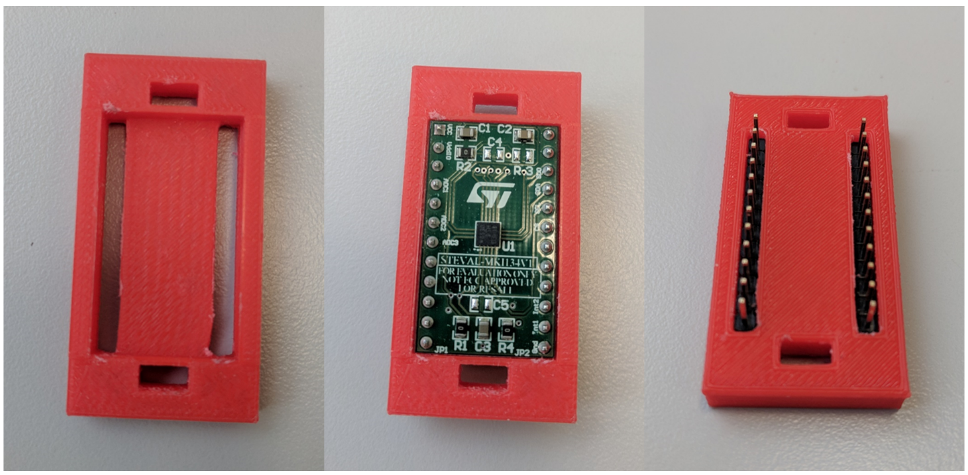

Figure 4.6: LIS3DSH Accelerometer and evaluation board placed inside 3D printed case.

The accelerometers used are LIS3DSH 3-axis accelerometers on a manufacturer supplied evaluation board with pins to allow for simple wire connections. In order to mount the accelerometers on the blade, they are placed in a 3D printed case shown in Fig. 4.6. The accelerometer chip communicates with an Arduino UNO microcontroller through serial I^2C over the SCL and SDA lines and requires 3.3 V of power. The wiring diagram is shown in Fig. 4.7. The serial address of the chip can be chosen by connecting the SDO pin to either ground or the supply voltage. This allows up to two accelerometers to be connected to the same microcontroller. The Arduino reads the data from each device

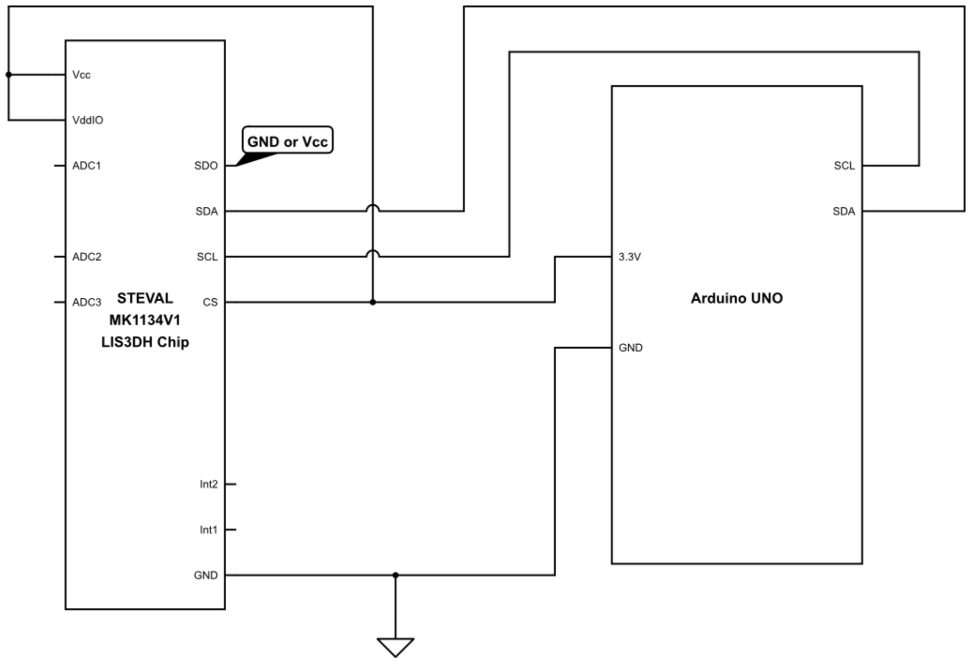

Figure 4.7: The wiring diagram for connecting each accelerometer to the microcontroller.

and streams it to a computer connected via USB.

Once a tip load is applied, the orientation of the accelerometers, recorded over a 5 second interval and subtracted from their original position, gives the bending slope in the chord and normal directions at each point. After repeating the measurement for several tip loading conditions, the EI is calculated from Eqn. 4.4 rearranged to utilize the slope of the curves in Fig. 4.11 in units of bending slope, $\frac{\mathrm{d}n}{\mathrm{d}r}$ or $\frac{\mathrm{d}c}{\mathrm{d}r}$, per tip load, P, in Newtons:

$$EI_N = \frac{1}{2}\left(a_2^2 - a_1^2\right)\left(\frac{P}{\frac{\mathrm{d}n}{\mathrm{d}r}_2} - \frac{P}{\frac{\mathrm{d}n}{\mathrm{d}r}_1}\right) \tag{4.15}$$

$$EI_C = \frac{1}{2}\left(a_2^2 - a_1^2\right)\left(\frac{P}{\frac{\mathrm{d}c}{\mathrm{d}r}_2} - \frac{P}{\frac{\mathrm{d}c}{\mathrm{d}r}_1}\right) \tag{4.16}$$

Where a is the distance from the tip load to each accelerometer in meters. Subscripts 1 and 2 denote values for each individual accelerometer. Equations 4.15 and 4.16 are not simplified completely to not factor out the applied load, P. Since measurements are taken over a sweep of applied tip loads, the ratio of applied to bending slope, $\frac{P}{\frac{dn}{dr}}$, is used to take an average measurement across all test points.

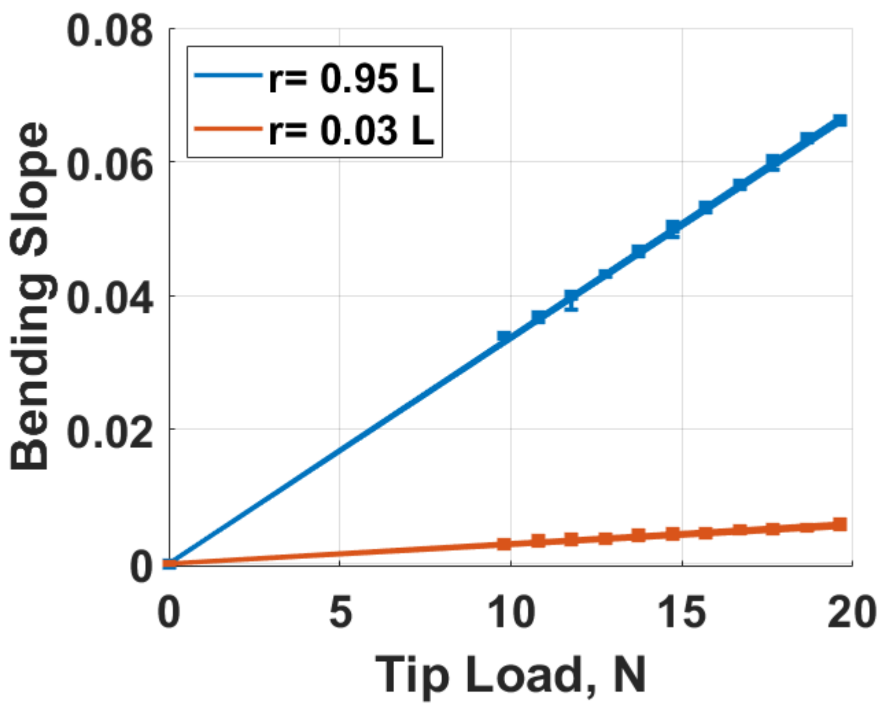

Figure 4.8: Measured bending slopes, w', of the aluminum beam as bending moment increases.

Before measuring the stiffness of the composite blades, the accelerometer method was first validated with an aluminum beam with a cross section of 1 inch x 1/4 inch. The beam was mounted vertically and accelerometers were placed 2.3 cm and 49.1 cm from the tip. Figure 4.8 shows the measured slopes at each point as the bending moment is increased across three trials. The results are plotted with 95% confidence intervals derived from the 500 samples collected for each individual data point. Figure 4.9 shows the height of the confidence intervals are independent of the applied load. The confidence intervals are representative of the level of noise in the accelerometer signal. The solid lines are lines

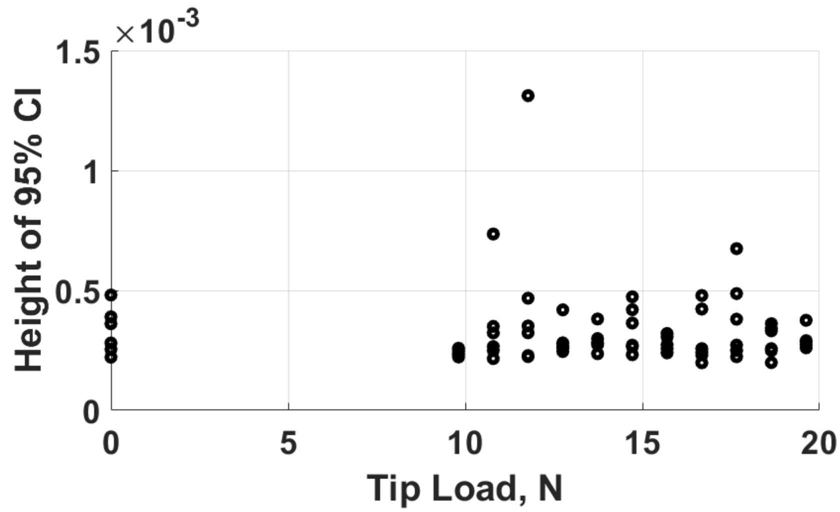

Figure 4.9: Height of the 95% confidence intervals of each data point for both radial locations.

of best fit for each trial. The results across three trials are indistinguishable and the noise is very low compared to the mean value. Additionally, there is a clear separation between the upper and lower measurement points and the slope close to the tip is increasing at a much higher rate. There is a clear improvement in repeatability and precision over the mirror method. The slopes of the blue and red lines in Fig. 4.8 are 0.034 1/N and 0.003 1/N respectively. This results in a measured bending stiffness of $EI = 38.9$ Nm^2 which is within 3% of the theoretical value of $EI = 37.8$ Nm^2. For further confirmation of the beam properties, the beam was left cantilevered and the first natural frequency was measured with a rap test. The frequency was measured to be 19.3 Hz, still within 3% of the analytical value of 19.9 Hz. The results of the accelerometer method on the aluminum beam assured its accuracy and precision for measuring the bending stiffness of a beam and allowed for testing on the composite blades.

The results of the straight, untwisted blade are shown in Fig. 4.11. The flap and lag directions are expected to be uncoupled, but the flap bending due to a lag load and vice versa are plotted for completeness. The small amount of curvature seen is most likely due to the load not being applied perfectly orthogonally to the blade section. Figure 4.11d shows the measurement for normal bending stiffness of the cross section. In Fig. 4.11a, the chordwise bending slope is more than an order of magnitude lower. This causes small variations in the test setup for each trial and signal noise to play a larger role as evidenced by the relatively wider confidence intervals. This ultimately leads to the larger measurement error in Table 4.1. Using Eqns 4.15 and 4.16 and the slopes of the lines shown in Figs. 4.11a and 4.11d, the normal bending stiffness, EI_N, is measured to be 20.1 $\pm$ 0.1 Nm^2 and the chordwise bending stiffness, EI_C, is measured to be 937 $\pm$ 33 Nm^2.

For a direct comparison of the mirror method to the accelerometer method, Fig. 4.12 overlays the results of Fig. 4.5b and Fig. 4.11b, the flap bending slope due to a flap load for both methods. It should be noted that the accelerometers and mirrors were not located at the same length along the blade for each method. Thus, a direct comparison of the measured slopes is not possible. However, the issues of the mirror method's repeatability as well as inability to differentiate the two mirror locations are starkly contrasted with the nearly identical trials of the accelerometer method.

When the blade is mounted vertically, pitch deformations cannot be measured by the accelerometers unless there is significant deflection of the blade section. This is because rotations about the vertical axis do not alter the components of gravity along any accelerometer axis. In order to measure GJ using the accelerometer method, the blade must be clamped in a horizontal orientation. Then, with the application of a pure torque

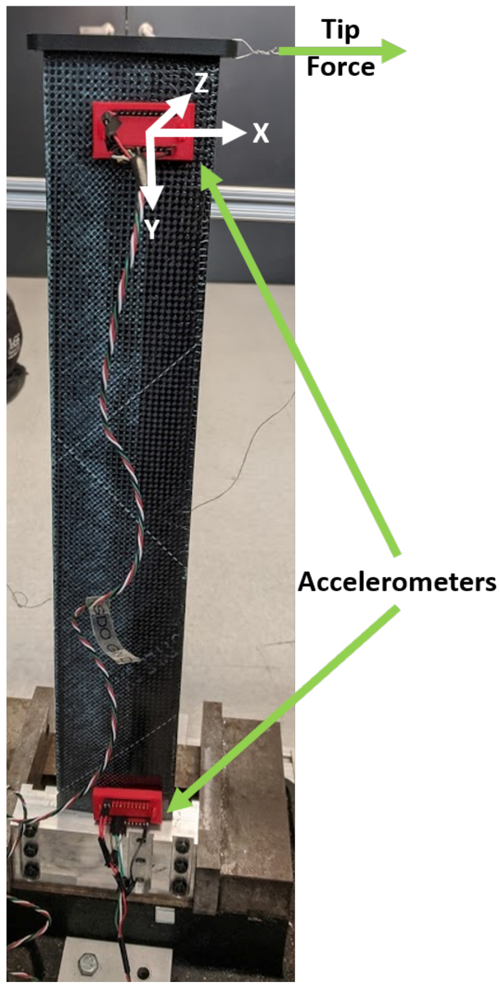

Figure 4.10: Test configuration for the accelerometer method of measuring blade stiffness with the accelerometer coordinate frame labeled.

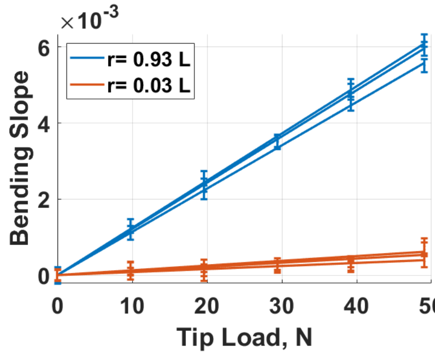

(a) Lag bending due to a lag load.

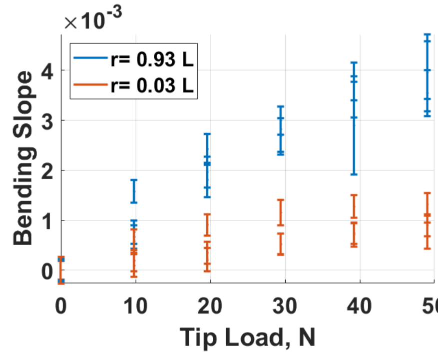

(b) Lag bending due to a flap load.

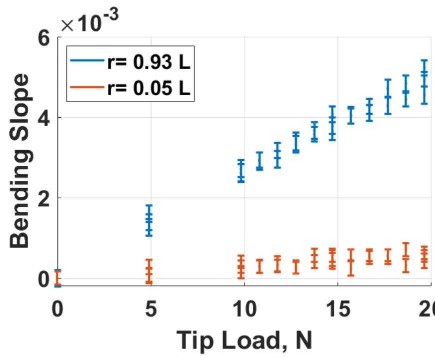

(c) Flap bending due to a lag load.

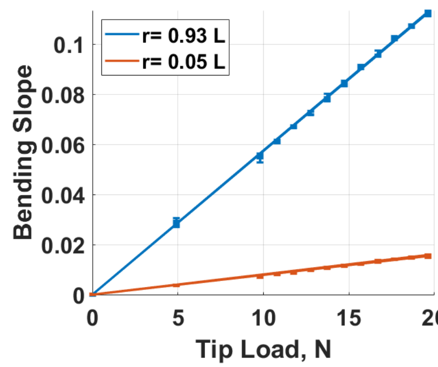

(d) Flap bending due to a flap load.

Figure 4.11: Measured bending slope of each accelerometer over a range of applied tip loads and three trials.

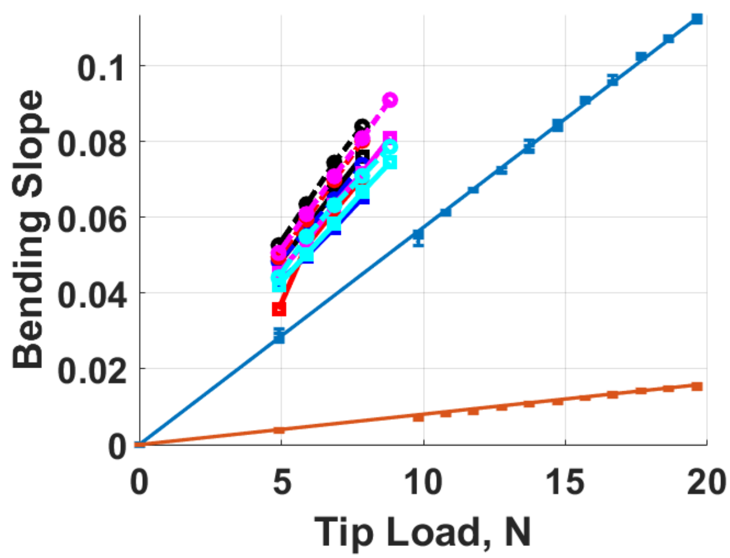

Figure 4.12: Measured flap bending slope due to a flap tip load for mirror and accelerometer methods.

at the tip, the GJ can be calculated in a similar way to EI from the results in Fig. 4.13:

$$GJ = (r_2 - r_1)\left(\frac{T}{\phi_2} - \frac{T}{\phi_1}\right) \tag{4.17}$$

where T is the applied torque at the tip, in Nm, and ϕ is the torsional deflection of each accelerometer, in radians. The GJ was measured to be 62 $\pm$ 3 Nm^2/rad.

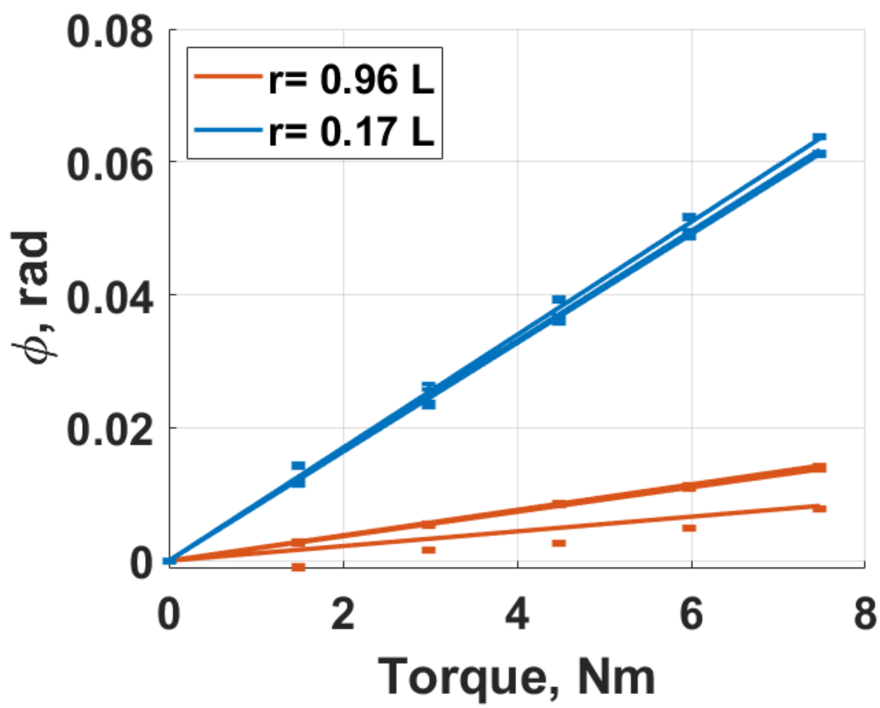

Figure 4.13: Measured torsional deflection under an applied torque for two points along the blade.

4.3 Inertial Measurements

The blade mass per span is calculated from the overall mass, measured by a scale and measured length of the blade and assumed to be uniform across the entire blade.

Several methods were attempted to measure the overall blade center of gravity. The first method was to balance the blade on a sharp edge along two separate axes. The overall center of gravity will lie at the intersection of these two axes, as shown in Fig. 4.14. Marking this point, the c.g. location was confirmed by balancing the blade on a 1/8-in diameter rod and measured to be 27.5 %c ± 2 %c. Since the result is behind the quarter-chord location, and the rod results in 2 %c error, two additional methods were used to measure the c.g. location. Figure 4.15a shows the blade balanced at 3 points, each supported by a scale. The c.g. location can be calculated from the reaction forces and locations of each support to be 27.3 %c ± 0.6 %c. Figure 4.15b shows a similar setup except the leading edge is supported by a sharp edge and only a single point at the trailing edge. This method only measures the chordwise location and not the spanwise location, but provided the highest precision measurement of 27.6 %c ± 0.2 %c. Having repeated the measurement with three separate methods, the center of gravity was confirmed to be located at 27 %c ± 1%c.

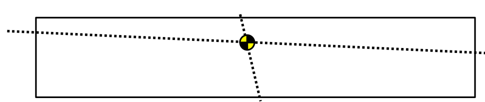

(a) Diagram of 2 axes for c.g. measurement

(b) Straight blade balanced on a single sharp edge

Figure 4.14: Test setup to measure the blade's center of gravity.

To measure inertia, the blade is hung vertically as a pendulum as shown in Fig. 4.16a. The inertia in the lag plane was measured because of the reduced effect of drag on the swinging pendulum. The lag inertia is approximately equal to the flap inertia. A lightweight plastic grip that is the same overall length of the rotor hub was used to

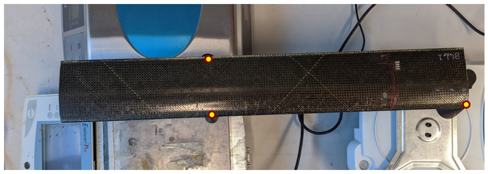

(a) Blade balanced on 3 scales, with yellow circles highlighting the balance points

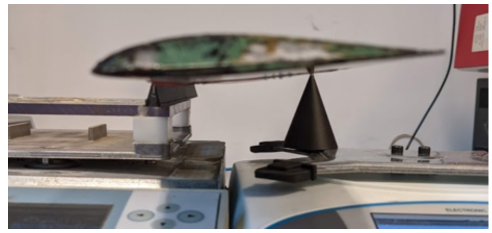

(b) Blade balanced on a single edge at the leading edge and a single point along the trailing edge

Figure 4.15: Test setup to measure the blade center of gravity.

attach the blade to a ball bearing. The period of the pendulum was measured using a laser distance gauge to record when the pendulum reached the bottom of its swing. Using the pendulum period and spanwise c.g. location, the inertia is calculated as:

$$I_b = mgL \left(\frac{T}{2\pi} \right)^2 \tag{4.18}$$

where m is the blade mass in kg, g is acceleration due to gravity in m/s^2, L is the distance from the center of rotation to the blade c.g. in m, and T is the period of the pendulum in seconds. Subtracting the measured inertia of the grip itself, the blade moment of inertia about the center of rotation is measured to be 0.041 ± 0.01.

Table 4.1: Measured properties of the fabricated untwisted blade compared to 1:5.26 Froude-scale XV-15 target.

Blade Property	Target	Measured
Mass (kg/m)	0.325	0.33 $\pm$ 0.005
Center of Gravity	25%	27% $\pm$ 1%
I_b (kg-m^2)	0.035	0.041 $\pm$ 0.01
EI_N (Nm^2)	23	20.1 $\pm$ 0.1
EI_C (Nm^2)	350	937 $\pm$ 33
GJ(Nm^2)	–	62 $\pm$ 3

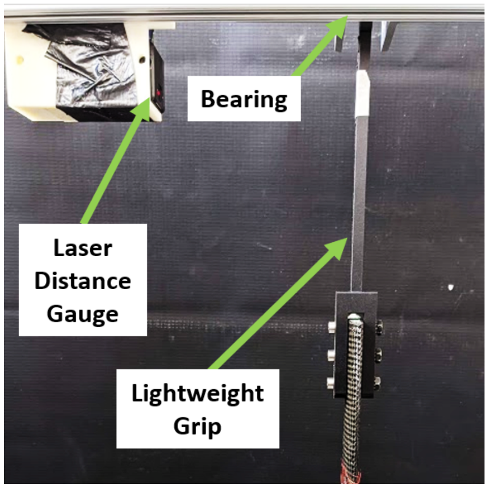

(a) Untwisted blade swung as a pendulum to measure inertia about hub center.

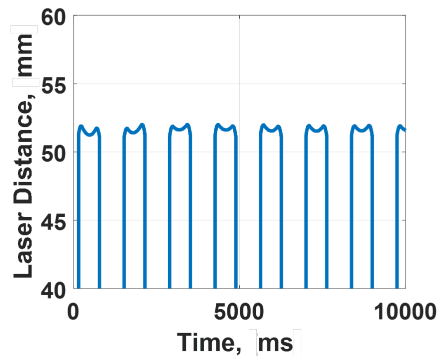

(b) Measured distance to pendulum as it passes in front of the laser distance gauge.

Figure 4.16: Test setup and measurements of the blade's inertia.

4.4 Non-Rotating Frequencies

To measure the non-rotating frequencies, a blade was clamped at the root and the flap and lag bending strains were measured after a tip impulse (rap test). Taking the Fast Fourier Transform (FFT) of the signal in time provides the natural response of the blade in the frequency domain.

Figures 4.17 and 4.18 show sample results for the untwisted blade. While vibrations at the first frequency sustain for several seconds, the higher frequency vibrations are quickly damped. For this reason, two separate measurements are taken. The first records the strain after a large tip deflection for 5 seconds and the first few cycles are shown in Fig. 4.17. The long duration allows for high resolution in the FFT. As expected from the gauge placement, some leakage of the flap signal into the lag strain measurement is observed. The second measurement, in Fig. 4.18 records 0.5 seconds of data after lightly rapping the leading edge. This captures the higher frequency modes before they damp out, but at the cost of lower resolution frequency data. The measured frequency for all three blade geometries are listed in Table 4.2.

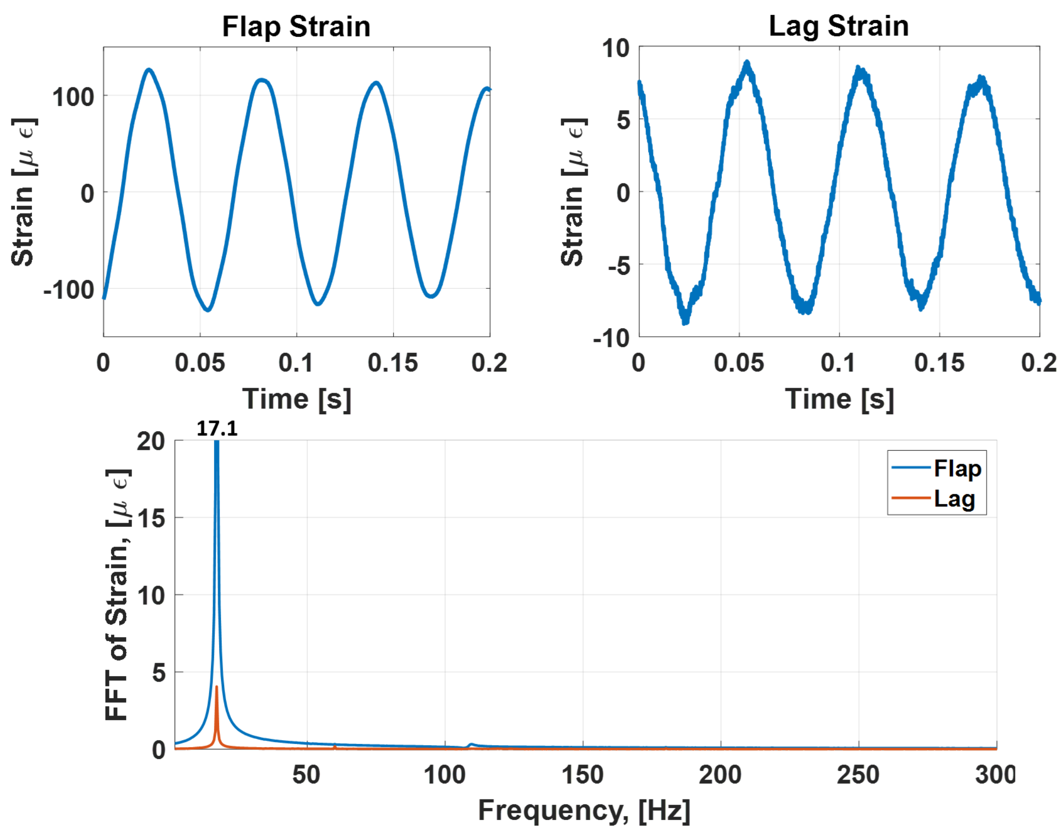

Figure 4.17: Recorded bending strains and FFT of strain after a tip deflection.

Table 4.2: First three measured non-rotating frequencies (Hz) for each blade geometry.

Untwisted	Twisted	Swept-Tip
17.2 ± 0.1	17.5 ± 0.1	24.2 ± 0.1
109.5 ± 1	90 ± 1.5	113 ± 2
119.3 ± 1	133 ± 1.5	185 ± 2

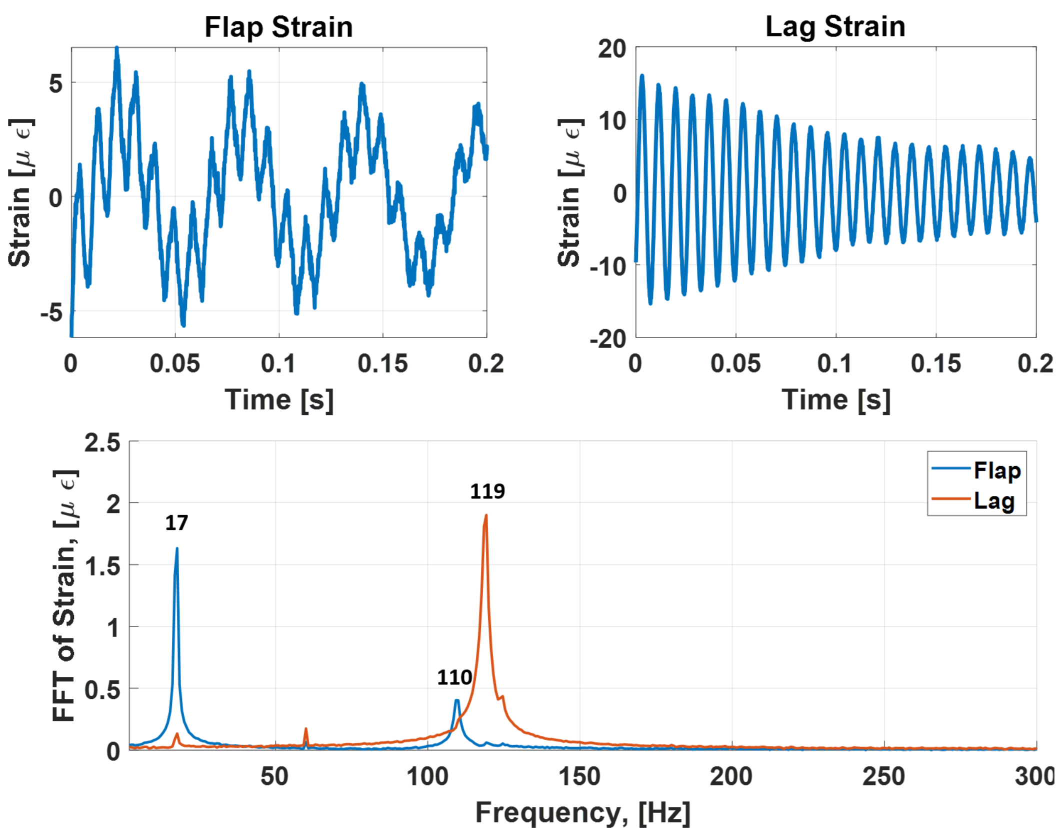

Figure 4.18: Recorded bending strains and FFT of strain after a light rap on the leading edge.

Chapter 5: 3-D Finite Element Modeling

Three-dimensional (3-D) rotor analysis is performed using X3D, an in-house 3-D finite element aeroelastic solver for rotors developed by UMD and the US Army TDD (Technology Development Directorate) [74]. X3D models isolated rotors in trimmed conditions and prescribed maneuvers to predict dynamic 3-D stresses and strains. X3D includes lifting-line aerodynamics with its structural solver but also has the interfaces for coupling with CFD. The structural solution is found by solving the 3-D governing equations of motion derived in the rotating frame using generalized Hamilton's Principle. The internal lifting-line model combines thin airfoil theory with 2-D airfoil tables and Maryland free wake for induced inflow. Each finite element can be assigned a full anisotropic 6×6 material matrix and is required to be a 27-noded hexahedral with internal nodes to prevent shear locking of thin elements.

This chapter describes the process of building the 3-D model for use in X3D. The first section covers the detailed CAD model and meshing. Next, the structural analysis model and material properties are described. Finally, the structural and inertial properties of the model are compared to the measured values.

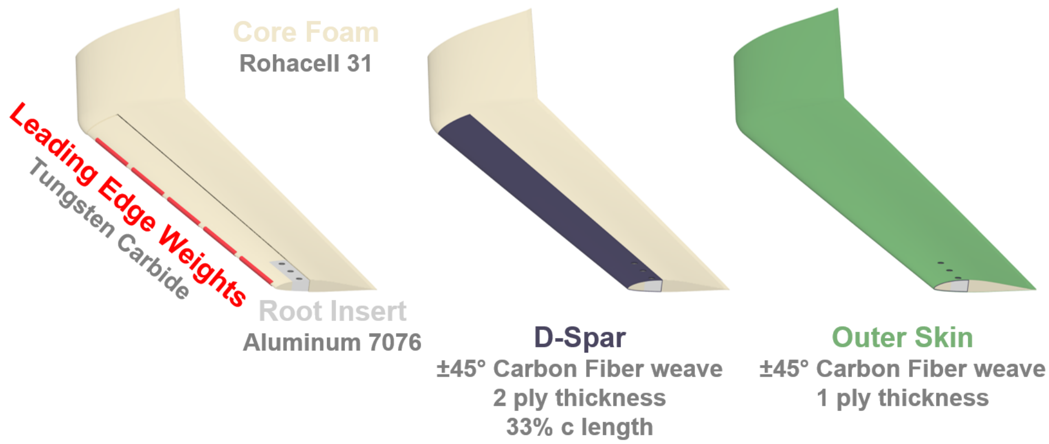

Figure 5.1: Overview of each component in the CATIA model of the swept-tip blade.

5.1 Structural Mesh Generation

In order to perform the analysis in X3D, a high-fidelity 3-D model must be built for each blade. To generate the geometry, the blade is first modeled in CATIA starting with the outer mold line. The model, shown in Fig. 5.1 includes each component of the blade with the exception of the film adhesive used between the foam and carbon fiber layers. This is because after curing, the film adhesive seeps into the foam and takes up no additional volume.

The geometry from CATIA is subsequently meshed in Cubit, a mesh generation tool from Sandia National Laboratories. Cubit was chosen to generate the mesh because it has a robust solid hexahedral meshing capability, including 27-noded elements. The Cubit mesh of the baseline blade is shown in Fig. 5.2. While each element can have its own material in Cubit, they are assigned to specific blocks which can be assigned material properties in X3D. In order to account for the orientation of the carbon fiber layup as it wraps around the airfoil and sweeps along the blade, the spar and skin are divided into

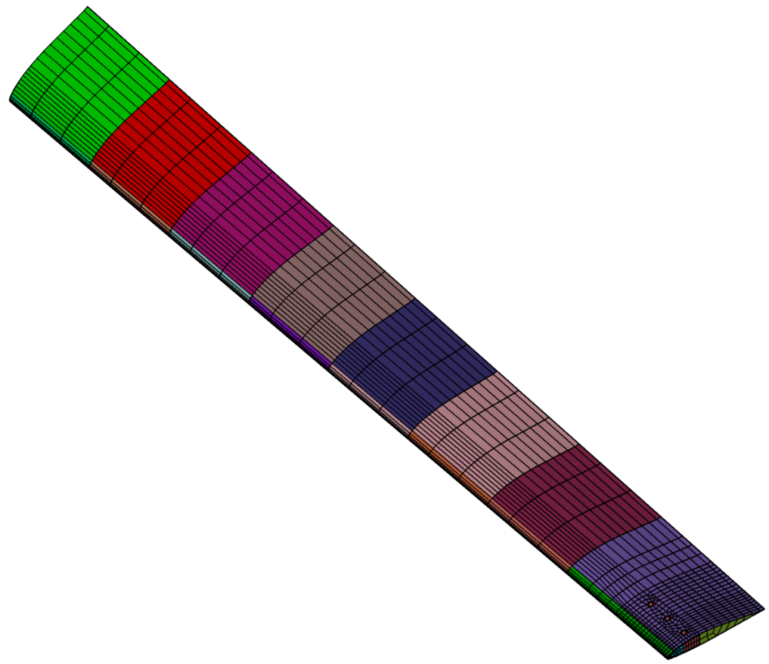

Figure 5.2: Cubit mesh of the baseline blade with colored material blocks.

multiple chordwise and spanwise blocks. The final meshes are shown in Fig 5.3. The untwisted blade mesh has a total of 25,992 nodes, the baseline blade mesh has 26,442 nodes, and the swept-tip blade mesh has 25,290 nodes. Thus, they all have approximately the same resolution.

5.2 Material Properties

The material properties applied to each block are outlined in Table 5.1. The density of the foam is prescribed to match the measured values of the fabricated blade to account for the mass of the film adhesive as well as compression in the mold. The properties for the carbon fiber are based on coupon tests performed in Ref. [75] of cured material from the same roll used for the blades. The data sheets do not provide all the necessary properties. The shear modulus, G, was tuned from the measured value of 5.54 MPa to

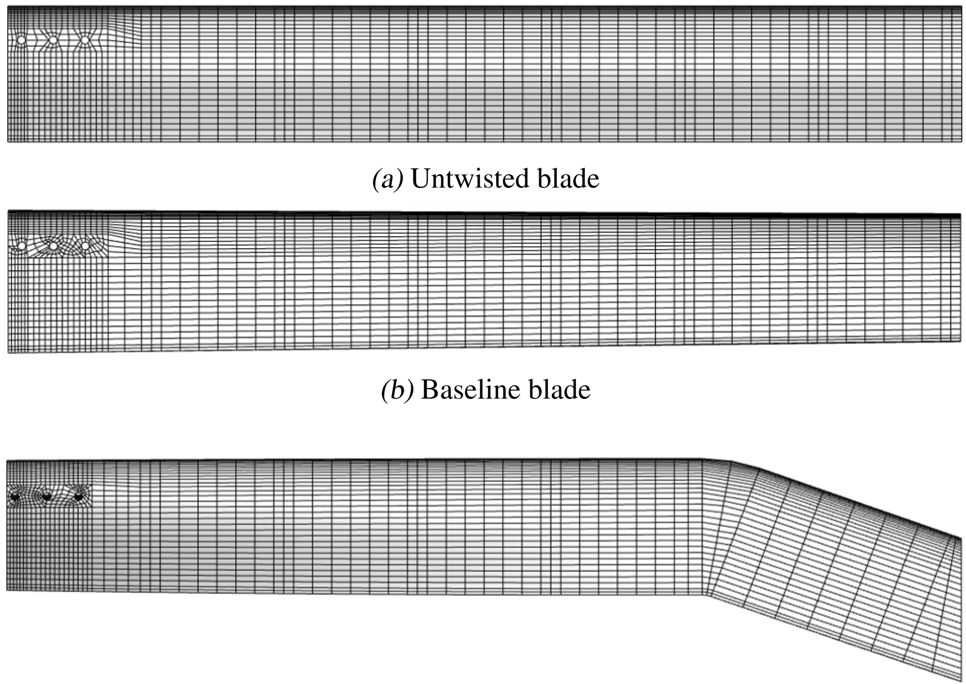

(a) Untwisted blade

(b) Baseline blade

(c) Swept-tip blade

Figure 5.3: Input meshes generated by Cubit for X3D analysis.

8.31 MPa in order to better match the blade natural frequencies as a part of [75]. All other properties are taken directly from material data sheets.

5.3 Structural Analysis Model

While X3D is capable of analyzing multiple flexible parts of the hub, the current model is focused on the blade. The blade is a single flexible part which has a root joint connecting the bolt holes of the root insert to the center of rotation. For hover and axial flow, the gimballed hub is a hingeless hub so the joint at the center of rotation is locked in flap and lag. The pitch is input through the joint. With the gimbal locked, the blade flapping is outboard of the pitch bearing so there is no control system kinematic delta-3.

Table 5.1: Material Properties

	ρ	ν	E_1	E_2	G	G
	kg/m^3		GPa	GPa	GPa	GPa
Source:		Coupon Measurement				Adjusted
IM7/8552 Carbon Fiber	1685	0.076	81.5	72.9	5.54	8.31
Source:		Material Data Sheet				
Rohacell Foam	194	0.3	0.36	–	0.140	
Tungsten Carbide	14,994	0.2	650	–	270	
Aluminum 7075-T6	2810	0.33	71.7	–	26.9	

5.4 Static Property Validation

To perform a rudimentary check on the measured blade properties with the X3D model, a set of tip deflection cases is setup. The overall mass, c.g, and inertia are calculated by X3D when reading in the structural analysis model. Dividing the blade mass by the blade length gives the cross-sectional mass distribution. For the static loading cases, all nodes on the blade root are locked and the nodes surrounding the 1/4-chord at the tip are loaded. Three separate cases are used to apply loads in the positive lag direction, Y-axis, positive flap direction, Z-axis, and pitch, X-axis.

The sectional bending stiffness, EI, is calculated from the deformations of each cross section along the span. First, the bending slope between each section is numerically differentiated from the deflection. Then, the flap and lag deflections, w and v, due to flap and lag loads are converted to a normal and chordwise coordinate system based on the geometric twist. After transforming the applied loads into the same coordinate system, the EI_C and EI_N can be calculated along each spanwise element of the blade. A similar method was used to calculate the GJ along the blade.

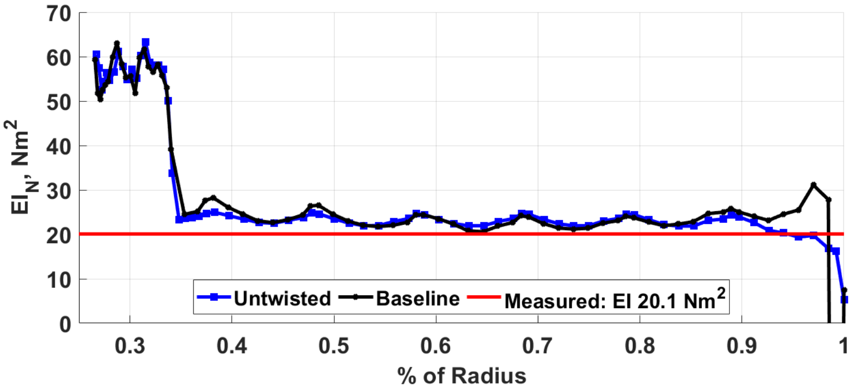

(a) Normal bending stiffness

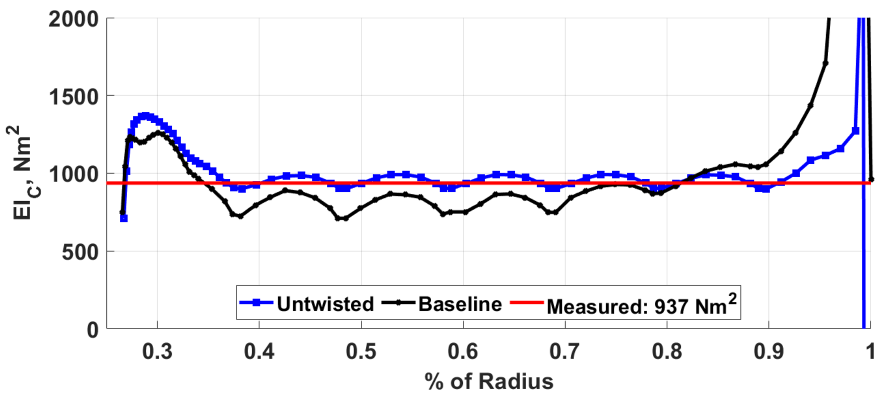

(b) Chordwise bending stiffness

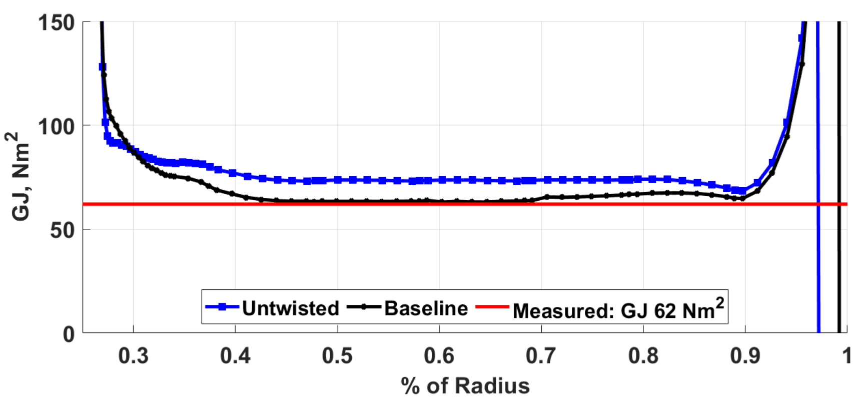

(c) Torsional stiffness

Figure 5.4: Calculated structural stiffness of each cross-section along the blade.

The results for both the untwisted and baseline blades are shown in Fig. 5.4. For comparison, the measured value is a single data point plotted as a horizontal line. Overall, the untwisted blade and baseline blade models both show very similar properties and correlate very well to the measured structural properties of the fabricated blade. The aluminum root insert lies from 26% - 35%R and causes an observable increase to EI_N and EI_C. The sudden jumps at the end are due to 3D effects at the blade tip where the load is applied. The seven leading edge weights placed along the blade, while designed to be non-structural, do cause a waviness in the spanwise distribution. Focusing on the stiffness between 35% R and 95% R, the finite element model well represents the measured stiffness of the physical blade. All cross-sectional properties are listed in Table 5.3

The eigen-frequencies and eigen-mode shapes of the system are calculated from the assembled mass and stiffness matrices. The first three predicted frequencies for all blades are listed in Table 5.2. Each frequency matches closely with the measured frequencies in 4.2 with the exception of the 3rd swept-tip blade mode. This error might be due to discrepancies between the perfect clamping condition of the modeled blade and the physical test setup. The associated mode shapes for these frequencies can be found in the Figs. 5.5, 5.6, and 5.7. Each figure depicts the first three non-rotating modes for the untwisted, baseline, and swept-tip blades. The undeformed mesh is shown in gray and each mode-shape is overlayed in black. Comparing the mode shapes of the untwisted and baseline blades reveals how strongly the -37° twist couples the flap and lag modes. Adding the swept-tip introduces additional coupling with the torsion mode.

Using the measured properties of the straight blade and the predicted properties from X3D, Table 5.3, gives the sectional blade properties of the swept blade.

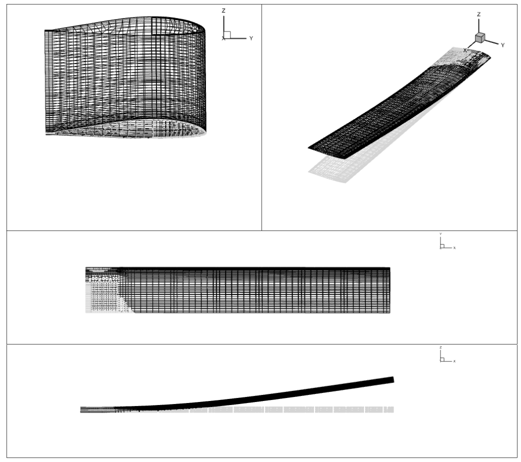

(a) First Mode: 20.6 Hz, 1st Flap

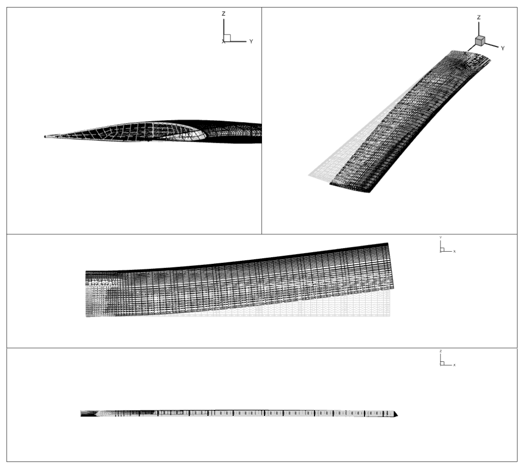

(b) Second Mode: 112 Hz, 1st Lag

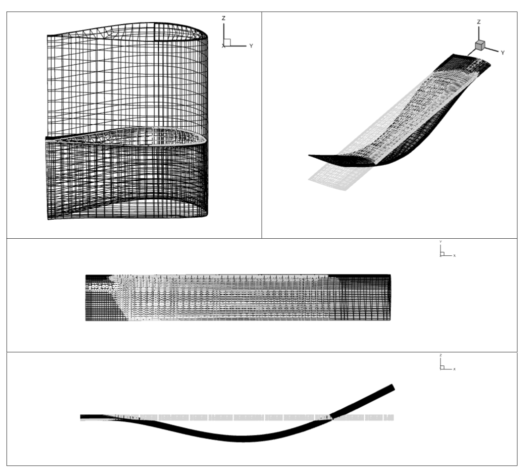

(c) Third Mode: 129 Hz, 2nd Flap

Figure 5.5: First three mode shapes for the untwisted blade, predicted frequency, and approximate mode labels.

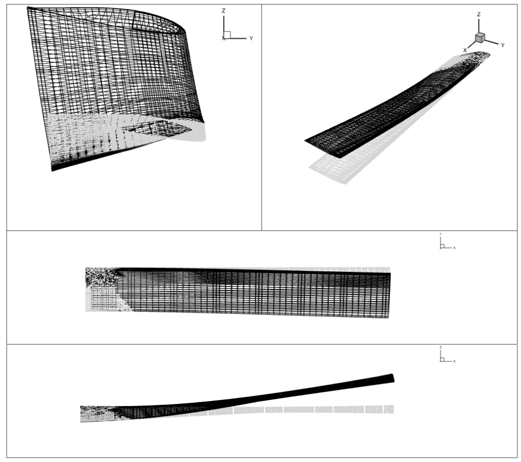

(a) First Mode: 20.9 Hz, 1st Flap

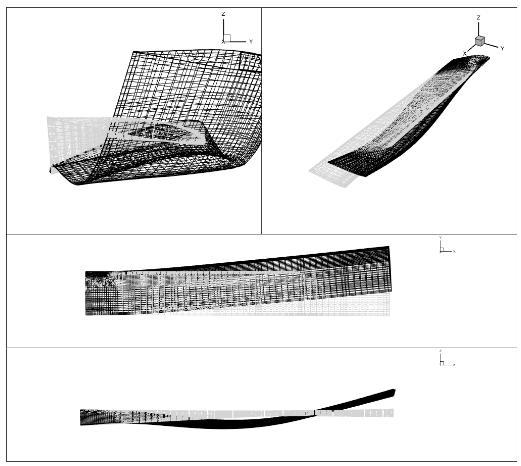

(b) Second Mode: 100 Hz, 2nd Flap / 1st Lag

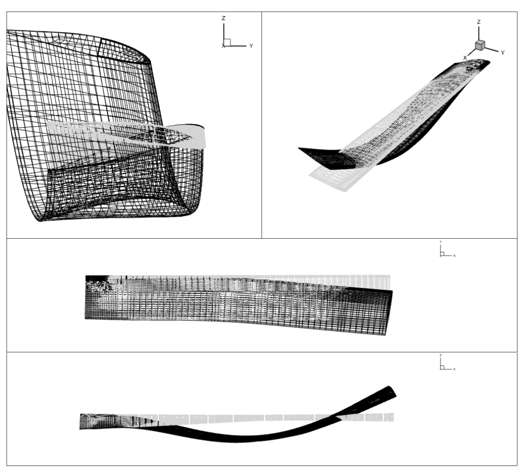

(c) Third Mode: 148 Hz, 2nd Flap / 1st Lag

Figure 5.6: First three mode shapes for the baseline blade, predicted frequency, and approximate mode labels.

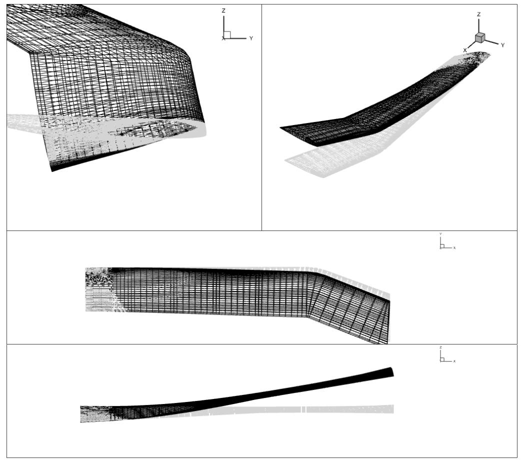

(a) First Mode: 25.3 Hz, 1^{st} Flap

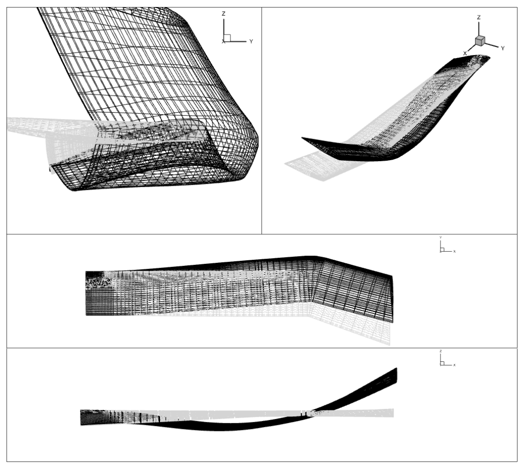

(b) Second Mode: 114 Hz, 2^{nd} Flap / 1^{st} Lag

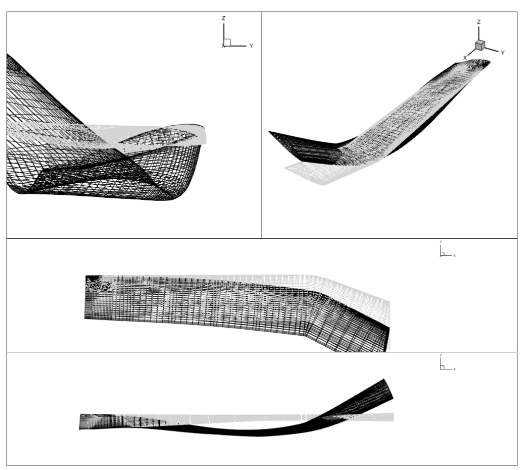

(c) Third Mode: 153 Hz, 2^{nd} Flap / 1^{st} Lag

Figure 5.7: First three mode shapes for the swept-tip blade, predicted frequency, and approximate mode labels.

Table 5.2: First three non-rotating frequencies (Hz) and modes for each blade geometry measured and predicted in X3D.

Untwisted		Baseline		Swept-Tip	
Primary Mode	Predicted	Primary Mode	Predicted	Primary Mode	Predicted
1F	20.6	1F	20.9	1F	25.3
1L	111.9	2F/1L	100.2	2F/1L	113.6
2F	128.8	2F/1L	148.0	2F/1L	153.2

Table 5.3: Cross-sectional properties of the blade sections predicted by X3D compared to the measured straight blade.

	Straight Section		**Swept Section**
	Measured	*Predicted*	*Predicted*
Radial Station, r/R	0.27 - 0.8		0.835 - 1.0
Chord (cm)	8.0	8.0	8.0
Mass/length (kg/m)	0.33 ± 0.005	0.34	0.15
Center of Gravity (% c)	$27\% \pm 1\%$	26%	45%
EI_N (Nm^2)	20.1 ± 0.1	24.1	12.0
EI_C (Nm^2)	937 ± 33	941	534
GJ (Nm^2)	62 ± 3	76	36.8

Chapter 6: Vacuum Chamber Testing

This chapter describes the first test of the blades under rotation in vacuum. The blades were installed in a 10-ft diameter vacuum chamber. The 3-D finite element model was used to replicate the same test. The measured rotating frequencies and strains are compared with X3D predictions to further validate the model.

Figure 6.1: 10 feet diameter vacuum chamber.

6.1 Experimental Setup

The straight and swept-tip blades were installed and spun in a 10-ft diameter vacuum chamber, shown in Fig. 6.1. Three of each blade geometry were tested in the vacuum chamber. There were two goals for this test. The first was to measure the rotating frequencies of the swept-tip blade. The second was to measure the 3-D strains. These were used to validate the X3D model at a range of RPM values.

Prior to testing, each blade was balanced using metallic tape at the end of the straight section. Figure 6.2 shows the blades rigidly connected to the hub with a root incidence angle of 0° and the same root cutout as the MTR of 27%R. The leads of a strain gauge rosette, located on the quarter-chord axis at 40%R, were connected to the 65-channel slip ring. A 60/rev encoder measured the rotor speed and an absolute pressure sensor recorded the pressure inside the chamber.

After installing the blades and slip ring connections, the procedure for testing was as follows. First, the chamber was sealed and evacuated using a vacuum pump. Next, the motor was powered on with a throttle setting of zero. The strains were then recorded as a nominal zero. The throttle was then adjusted to set the desired RPM. Again, the strains were recorded for 5 seconds before moving to the next throttle setting. This rotor speed sweep was repeated a total of three times for each blade. When testing of one blade was complete, the chamber was refilled with air and a new blade was installed. During testing, attempts were made to excite the blade by allowing an impulse of air through the inlet valve. However, the change in pressure was too slow to cause any impulsive perturbations in the blade.

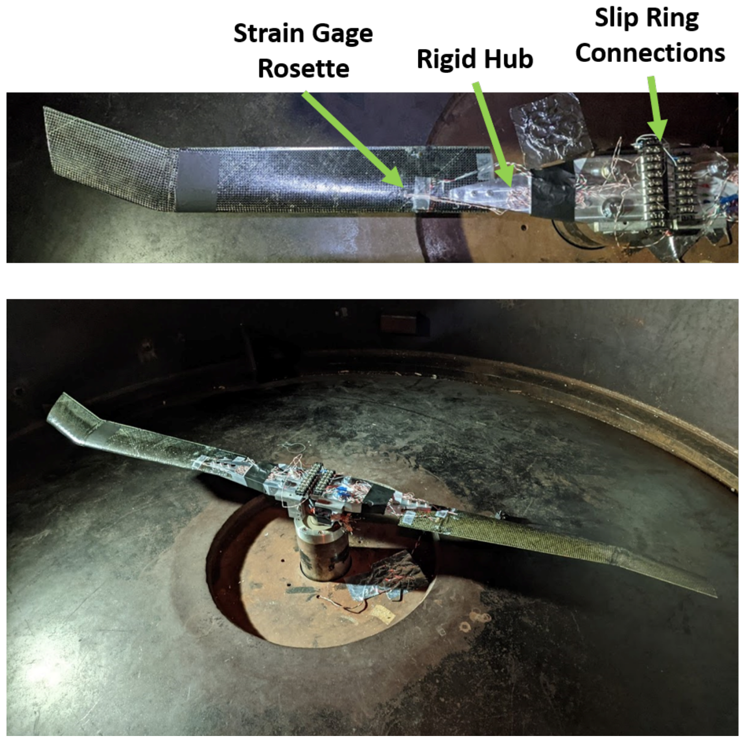

Figure 6.2: The swept-tip blades installed in the vacuum chamber.

6.2 X3D Vacuum Chamber Model

The X3D rotating strains and frequencies are obtained from a set of cases sweeping over a range of RPM. The blade bolt holes are rigidly connected to the center of rotation and no aerodynamics are applied to the blade. X3D directly outputs the stress at each node as well as the eigen-frequencies of the rotating system.

6.3 Rotating Frequencies

Examining the frequency content of the strain, it is first required to remove any frequencies known not to be caused by vibrations in the blade. At rest, the motor causes large spikes in the strain signal at multiples of the power supply frequency of 60 Hz as seen in Fig. 6.3. While at rest, the motor shaft vibrates at 120 Hz and imparts a physical

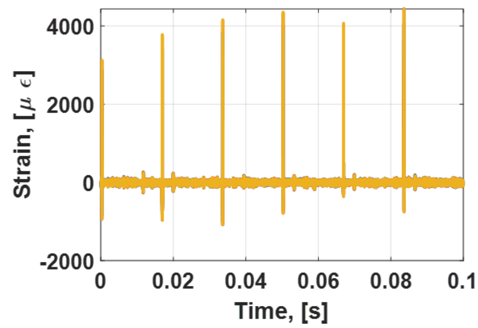

(a) Nominal zero with supply spikes.

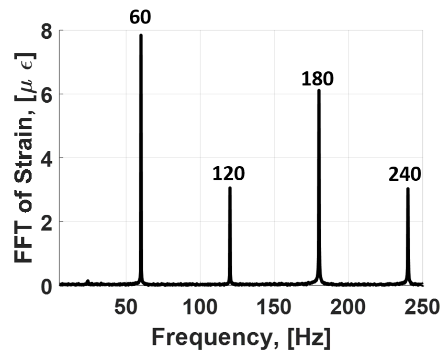

(b) FFT of resting strain signal.

Figure 6.3: Recorded strain while at rest in vacuum.

vibration to the blades. Once the blade is rotating, the spikes subside, but still persist. Fig. 6.4 shows a sample result for the strain in the swept-tip blade over 1 revolution and the Fast Fourier Transform (FFT) of the entire 5 second signal at 1050 RPM. Figure. 6.5 shows the five measured frequencies with tallest FFT peaks. The lowest frequency is 1/rev at every RPM tested. This is believed to be caused by variations in contact resistance in the slip ring brushes as the shaft rotates. Because the gauges are connected in a quarter-bridge configuration, changes in the resistance of the leads result in variations in the strain measurement. The next two frequencies to be ruled out are the consistent 60 Hz and 120 Hz spikes from the motor. The 60 Hz frequency is likely electromagnetic interference and the 120 Hz spike is from motor vibration. In addition to the 120 Hz frequency, there are 120 Hz $\pm$ 1/rev oscillations in the strain signal; these correspond to 102 Hz and 137 Hz

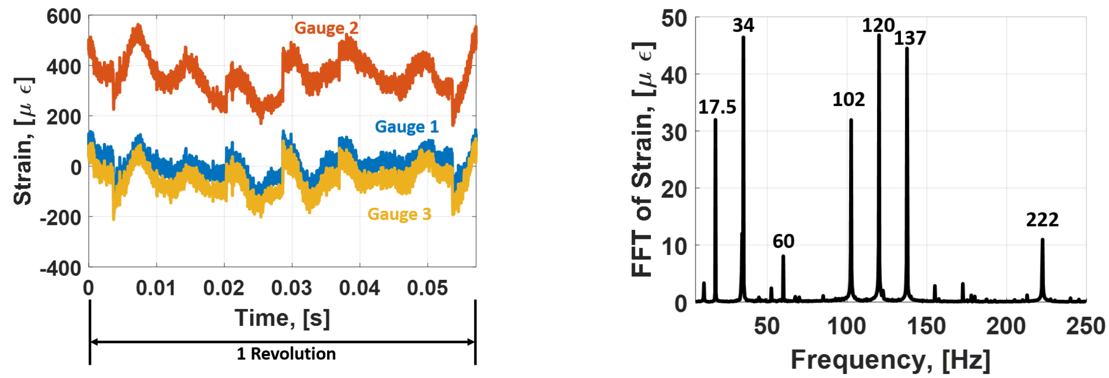

(a) Recorded strain over one revolution.

(b) FFT of rotating strain signal.

Figure 6.4: Recorded strain on the swept-tip blade while rotating at 1050 RPM.

in Fig. 6.4b. This is because the motor vibrations pass from the non-rotating to rotating frame and are measured at the blade root. Eliminating these spurious frequencies leaves only one set of frequencies that can be the result of natural blade vibrations. The process of removing spurious frequencies is shown for the swept-tip blade but was also performed for the twisted blade.

Figure 6.6a overlays the measured rotating frequencies (symbols) with the X3D predicted fan plot (lines) for both blade sets. Figure 6.6b shows a closer view of just the first elastic frequency. Along the y-axis are included the measured non-rotating frequencies. The comparison shows that the X3D model accurately predicts the first mode of the rotating response of each blade. Additionally, experiment and prediction demonstrate a measurable difference in the first frequency of each blade. The swept-tip blade deso not have leading edge weights in the outer 20% of the blade tip and therefore is lighter and has a higher frequency. In Fig. 6.6b, the measured frequency for the baseline blade at 700 RPM and the swept-tip blade at 900 RPM appear more likely to be a 2/rev forced oscillation and not natural vibrations of the first elastic frequency. But that cannot be concluded

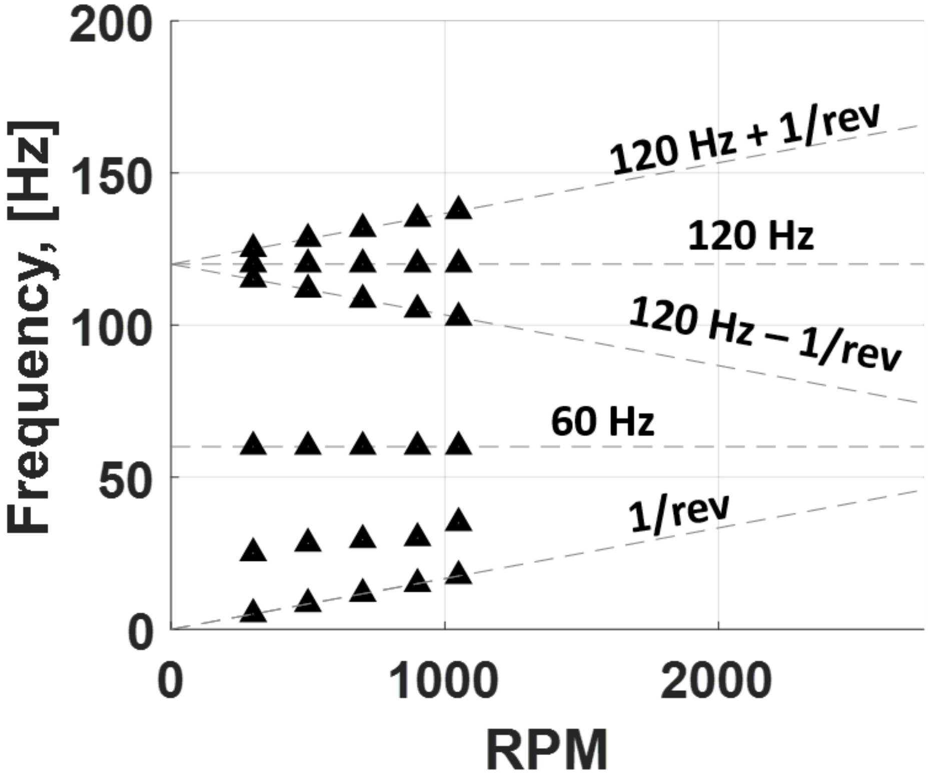

Figure 6.5: Primary frequencies of measured strains of the swept-tip blades.

without additional tests with active blade perturbation.

6.4 Rotating Strains

Over the course of one revolution, the strain signal is dynamic, but the mean level remains constant over the course of each revolution. The strain in each gauge is converted to the principal axes through the transformation:

$$\begin{bmatrix} \epsilon_{xx} \\ \epsilon_{yy} \\ \gamma_{xy} \end{bmatrix} = \begin{bmatrix} \cos^2\theta_1 & \sin^2\theta_1 & \sin\theta_1\cos\theta_1 \\ \cos^2\theta_2 & \sin^2\theta_2 & \sin\theta_2\cos\theta_2 \\ \cos^2\theta_3 & \sin^2\theta_3 & \sin\theta_3\cos\theta_3 \end{bmatrix}^{-1} \begin{bmatrix} \epsilon_1 \\ \epsilon_2 \\ \epsilon_3 \end{bmatrix} \tag{6.1}$$

where $\theta_1 = -45°$, $\theta_2 = 0°$, and $\theta_3 = 45°$, the angle between gauges 1 and 3 with the quarter-chord line. The average strain at each rotor speed is plotted in Fig. 6.7 with each symbol representing each individual blade and color corresponding to the strain axis. When mean vacuum chamber strains are compared directly with the X3D values, a strong correlation is observed and further verifies our model. The baseline blade shows similar results but the agreement with the test data is not as strong. Accurate prediction of strain values is a challenge because strain is a very local phenomenon and highly sensitive to variations in location, orientation, and concentrations due to changing materials of the composite blade. Additionally, [75] has demonstrated that incidental errors in the test setup can alter the measured strain.

Table 6.1: Measured first rotating frequency in vacuum.

Rotating Speed (RPM)	Baseline (Hz)	Swept-Tip (Hz)
0	17.5	24.1
300	20.0	25.0
500	–	28.18
700	23.4	29.4
900	27.7	30.0
1050	30.0	35.0

In addition to the single point where the strain rosette is attached, X3D provides stresses and strains along the entire blade geometry. Figure 6.8 shows the predicted axial stress values, σ_{11}, on the blade surface and along the cross section. The carbon fiber material used for the blades has a tensile yield strength of 979 MPa, more than one order of magnitude greater than the maximum stress level observed. This is typical of Froude scale models. Comparing the two results shows that the swept-tip introduces a component of centrifugal force in the lag direction that causes the surface stress to be carried in more

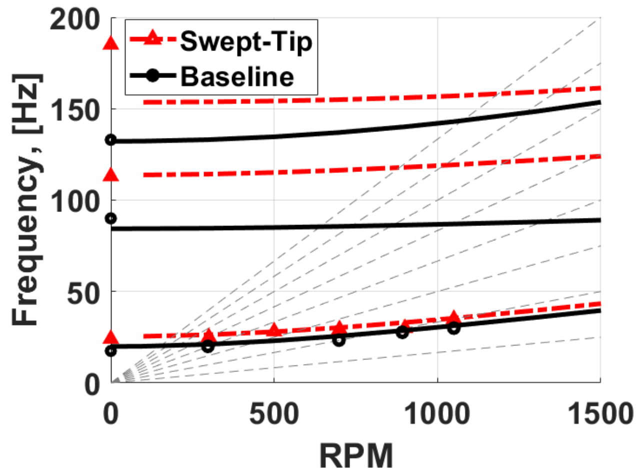

(a) Measured frequency and X3D predictions

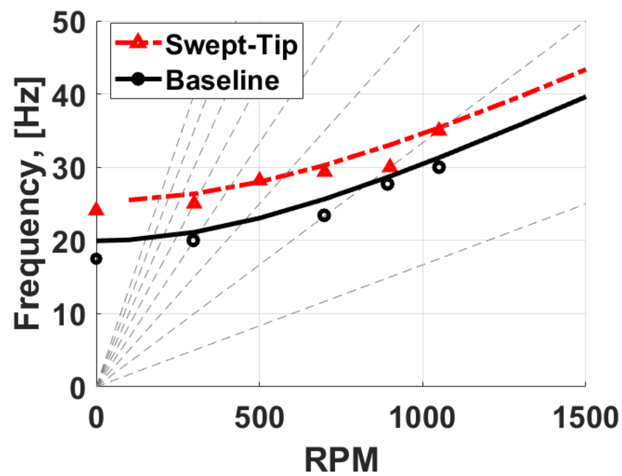

(b) Measured and predicted first rotating frequency

Figure 6.6: Measured and predicted frequencies under rotation in vacuum.

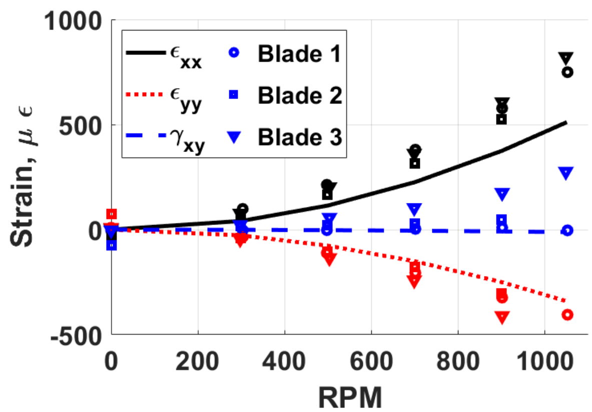

(a) Mean surface strain of the baseline blade.

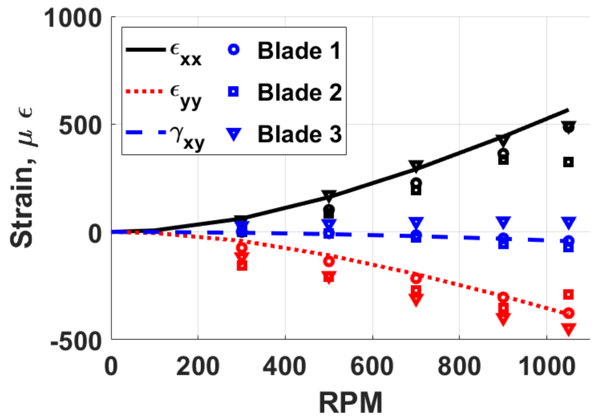

(b) Mean surface strain of the swept-tip blade.

Figure 6.7: Comparison of mean rotating strain between vacuum chamber tests and X3D; symbols are measured data, lines are predictions.

aft sections of the skin. Additionally, it causes a stress concentration at the trailing-edge of the transition region.

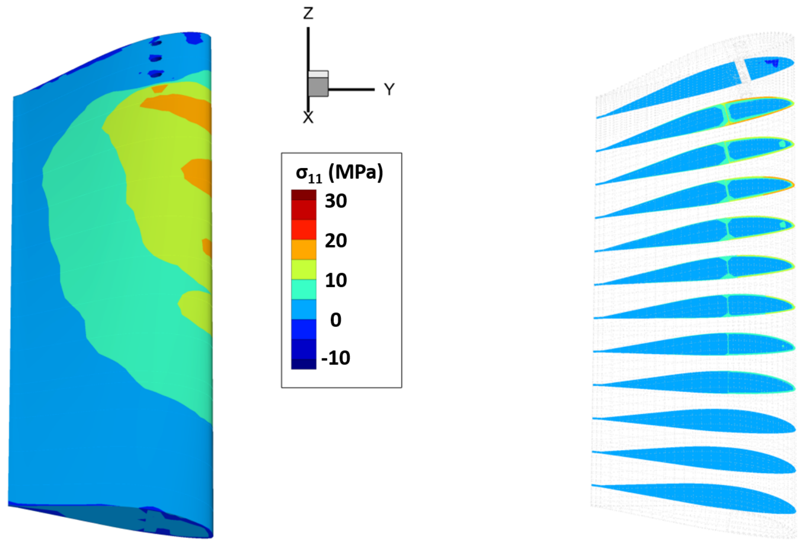

(a) σ_{11} distribution along the twisted blade.

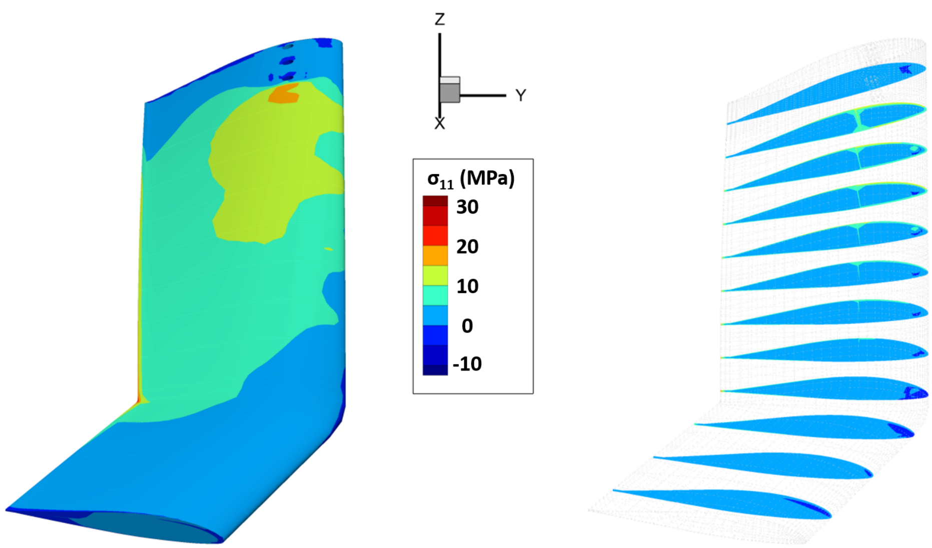

(b) σ_{11} distribution along the swept-tip blade.

Figure 6.8: Predicted surface and cross-sectional stress for the twisted and swept-tip blades in vacuum at 1050 RPM.

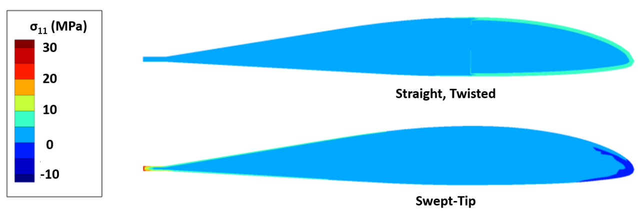

Figure 6.9: Predicted stresses at 80% R in vacuum.

Chapter 7: 3D Stress Analysis

This chapter describes the 3-D finite element analysis performed on the blades prior to aerodynamic testing. It starts with analysis in hover to evaluate the safety margin in the maximum static loading condition. The next section analyzes the rotor in forward flight to calculate the oscillatory stresses as well.

7.1 Hover Analysis

Prior to wind tunnel testing for the blades, X3D is used to evaluate the performance of the baseline and swept-tip blades. The calculation of 3-D stress and strains up-front in the design cycle is envisioned as an essential part of future design work-flow. X3D has provided the opportunity to put this vision into action. What follows is a true pre-test prediction of internal stress patterns of a new blade design enabled by 3-D structural analysis.

X3D's aerodynamic model is a lifting-line at 1/4-chord divided into distinct panels along the blade. Using blade element momentum theory (BEMT), the inflow, angle of attack, and airloads are calculated on each panel. The airloads are then applied to the structural segments of the mesh. The baseline blade has 14 aerodynamic panels along the span and the swept-tip blade has 13. The first 12 aerodynamic panels are identical to the baseline blade, but the swept and transition regions are defined as a single panel. The coarse aerodynamic panels are meant only for an initial assessment of critical stresses.

The entire blade uses the VR-7 airfoil tables to calculate lift, drag, and pitching moment on each panel including a low Reynolds number correction. The C81 decks are obtained using an in-house TURNS CFD code [76] at a Reynolds number of 10^6. In the swept-tip, a correction factor of $\cos^2(20°)$ is applied to the coefficients in the airfoil table to account for the reduced freestream velocity over the swept airfoils. In a hover condition, the collective angle, θ_{75}, is set and the blade structure and inflow iterate until convergence is reached.

The results of a collective sweep for the baseline blade and swept-tip blade are shown in Fig. 7.1. The collective range represents the total collective range of the MTR. At the rotor speed of 1050 RPM, the tip Mach number is 0.234. The thrust and power coefficients are scaled by the rotor solidity, $\sigma = 0.078$. The two blade geometries have very similar performance characteristics with the only observable difference occurring as the swept-tip blade begins to stall.

The difference in the two blades is revealed when examining the internal stresses. Figure 7.2 shows the predicted axial stress of the baseline and swept-tip blade. For a direct comparison of stresses between the two blade geometries, trim iterations were performed over $\theta_7 5$ until each blade achieved the same loading of $C_T/\sigma = 0.20$ near the peak of maximum thrust. On the surface, the swept-tip blade shows larger bending stresses along the length of the blade. With no spar in the swept-tip, the skin is forced to carry more of the flap bending load. This same result is observed when examining the cross section where the swept-tip starts. Figure 7.3 shows the stresses in a cross section located at

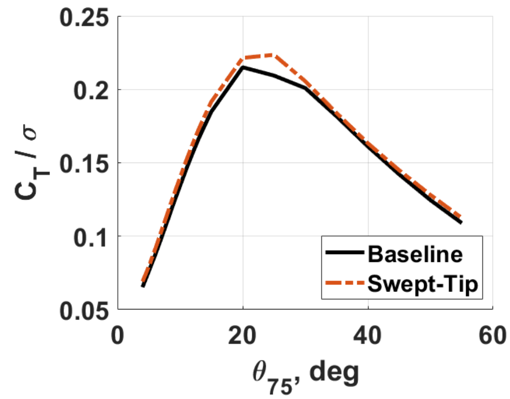

(a) Blade loading versus collective

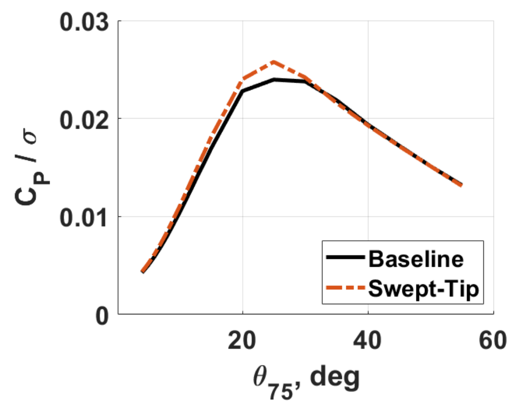

(b) Power coefficient versus blade loading

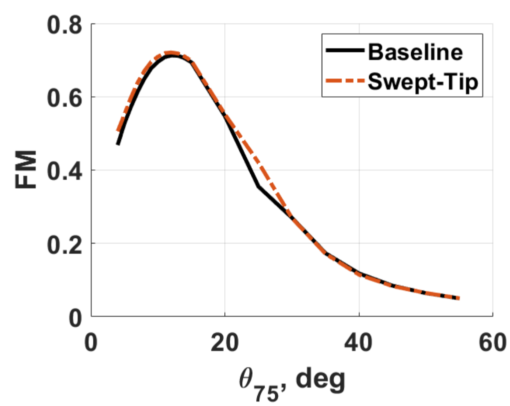

(c) Figure of Merit (FM) versus blade loading coefficient

Figure 7.1: Predicted hover performance for the baseline and swept-tip blades at 1050 RPM, M_{tip} = 0.23.

80% span. In addition to the higher stress being carried by the skin, there is also a high concentration at the trailing edge due to the centrifugal force on the swept-tip.

7.2 Forward Flight Analysis

As a final step to ensure structural integrity, the baseline and swept-tip blades are analyzed in helicopter mode. As a worst-case scenario, the rotor is analyzed with the gimbal locked and rigid hub components. As such, all loads must be carried by the blade root. The BEMT aerodynamic model is now replaced with free-wake. A single tip vortex, fully rolled up, is used. X3D has been recently validated against test data from the Tilt Rotor Aeroacoustic Model (TRAM) [77] and the same conditions are used here to anchor the predictions to a known result. The only difference from the work is that a free wake model is now used for instead of RANS CFD. This is deemed adequate for a gross assessment of safety margins. Only an isolated rotor is modeled without wing interference. Wing interference becomes important in airplane mode cruise.

The structural mesh and aerodynamic panels remain the same as hover. The wake is solved using Maryland Free Wake [78], which performs iterations starting from a prescribed wake until convergence of the wake geometry. The converged wake geometry for the baseline and swept-tip blades is shown in Fig. 7.4. To verify the aerodynamic results, the non-dimensional airloads of the MTR baseline blades are compared to predicted TRAM airloads without root fairing. Flying at an advance ratio of $\mu = 0.15$, with shaft tilt of -3°, and trimmed to $C_T/\sigma = 0.089$ with zero hub moments, the MTR and TRAM sectional airloads at 87% span show the same magnitude and trend in Fig. 7.5a. Since the

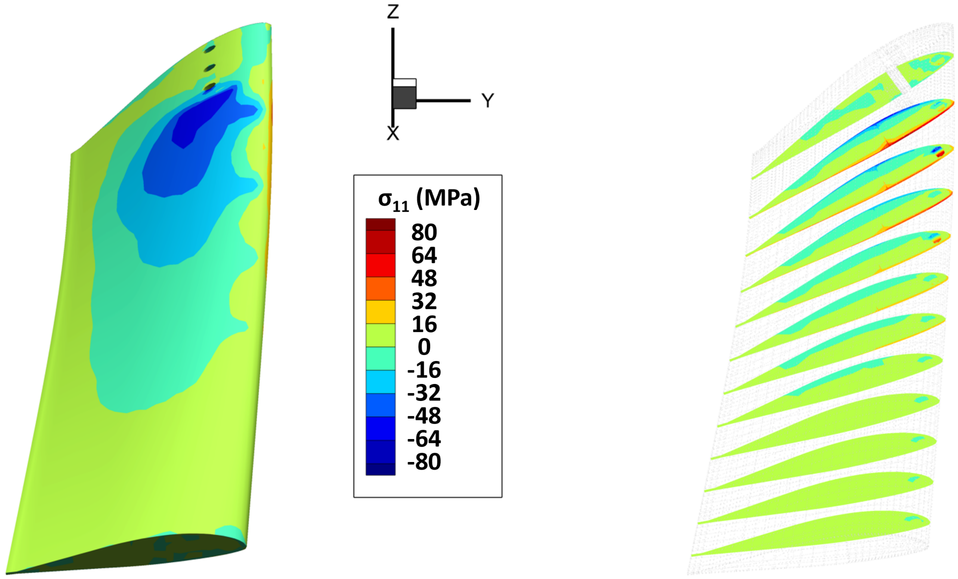

(a) σ_{11} of the baseline blade, $\theta_{75} = 16.6°$.

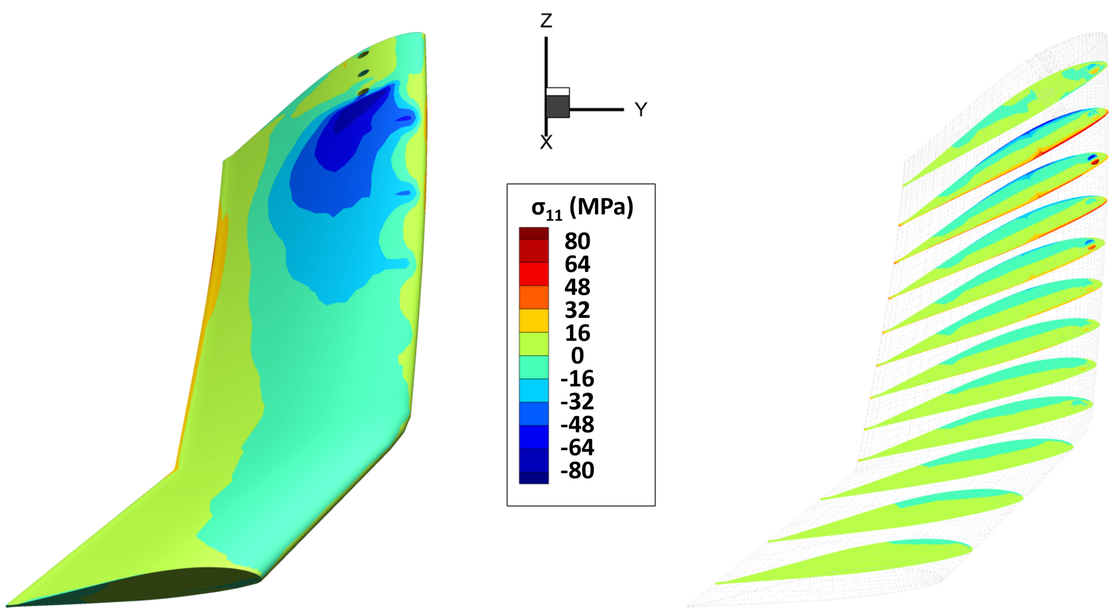

(b) σ_{11} of the swept-tip blade, $\theta_{75} = 15.8°$.

Figure 7.2: Predicted surface and cross-sectional stress for the baseline and swept-tip blades in hover at 1050 RPM and $C_T/\sigma = 0.20$.

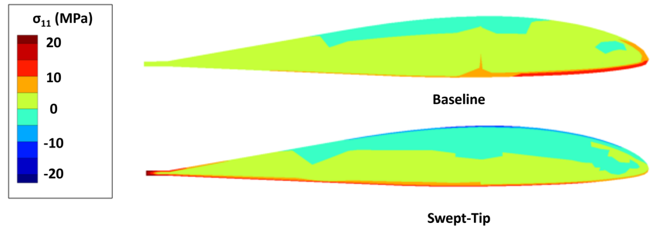

Figure 7.3: Stress in a cross section at 80% R during hover.

blades are Froude scale models, the tip Mach number is not matched. Thus, c_n, not M^2c_n is compared.

To estimate the maximum stresses that might be encountered, the analysis is performed at zero shaft tilt. Thus, the specific flight condition is at the operating RPM of 1050, with an advance ratio of $\mu = 0.15$ and no shaft tilt. The rotor is trimmed to a thrust of $C_T/\sigma = 0.10$ with zero hub moments. The trim controls for each blade geometry can be found in Table 7.1. Figure 7.5b shows the normal force coefficient at 87 % R. The swept-tip blade performs very similarly but demonstrates lower peak-to-peak oscillations at this radial station. Figures 7.6 and 7.7 show snapshots of the periodic blade stresses at 0, 90, 180, 270 degrees of azimuth. The maximum stress levels in each blade is 40 MPa, well below the yield strength of the carbon fiber skin and spar. On the advancing blade, inboard stresses on the top surface are comparatively higher while the bottom surface are lower. This indicates a reduced root bending moment that corresponds with the lower M^2c_n value. At the trailing edge, the swept-tip blade encounters higher stresses. But overall, the swept-tip does not cause a dramatic increase in stress levels.

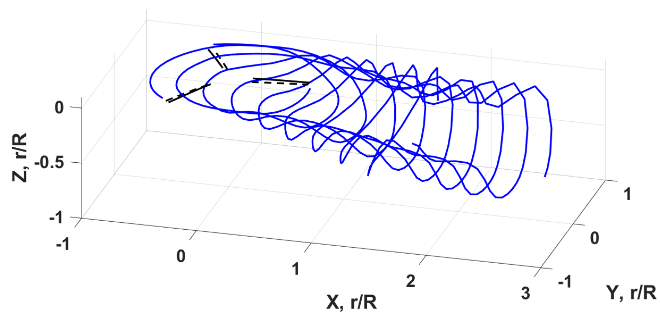

(a) Baseline blade wake geometry

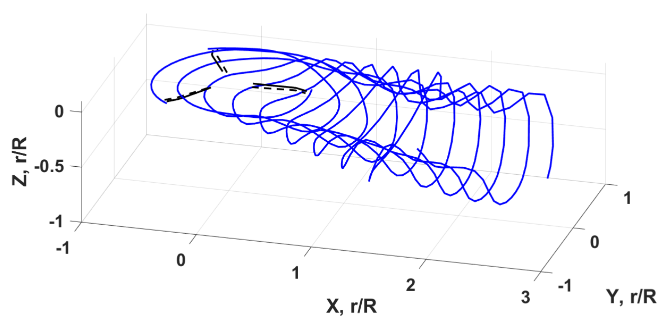

(b) Swept-tip blade wake geometry

Figure 7.4: Free wake geometries in forward flight. Black lines represent 1/4 and 3/4 chord lines of the blade; blue lines show trailing tip vortices.

Table 7.1: Collective and cyclic controls required to trim each rotor at $\mu = 0.15$.

	Baseline	Swept-Tip
θ_0	6.57°	5.86°
θ_{1C}	4.07°	3.81°
θ_{1S}	-2.34°	-1.98°

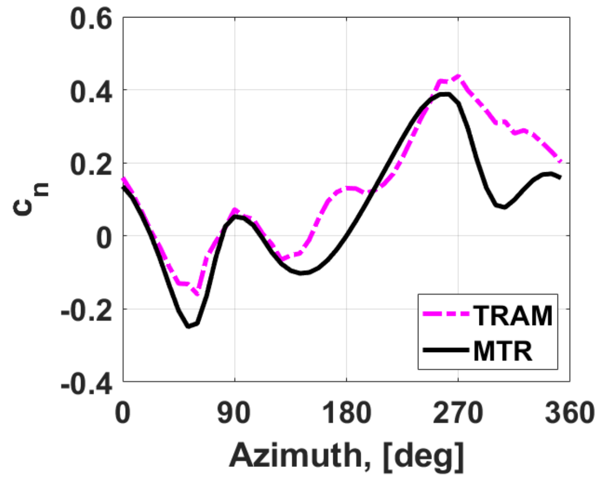

(a) TRAM rotor compared to MTR baseline rotor

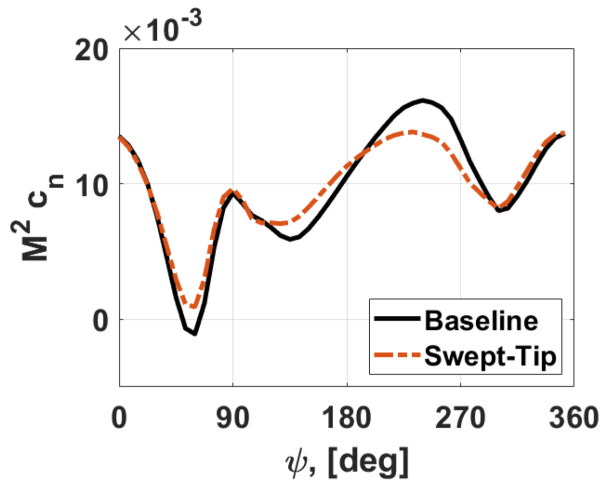

(b) MTR baseline rotor compared to swept-tip rotor

Figure 7.5: Aerodynamic normal force coefficient comparisons at 87% R.

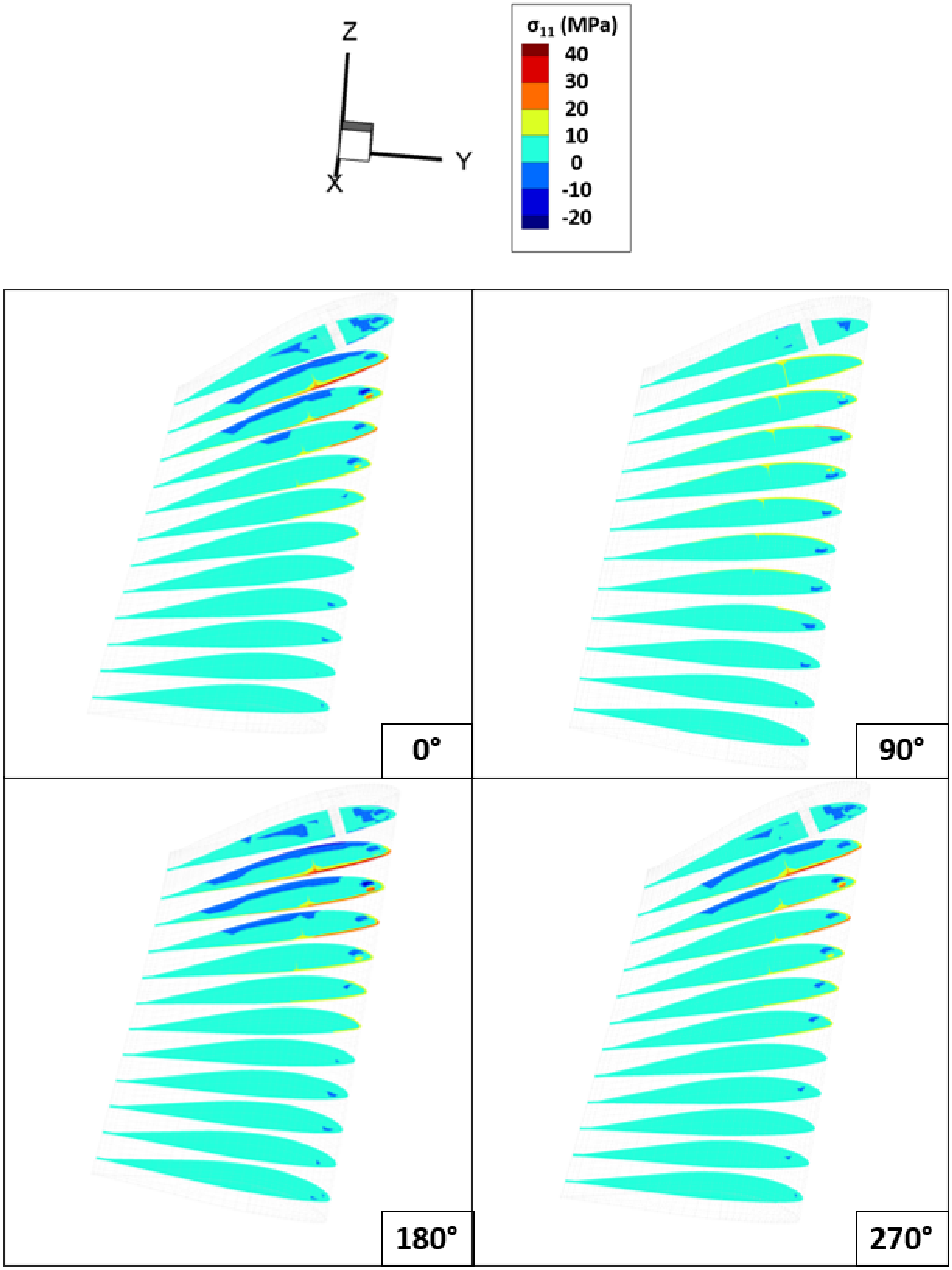

Figure 7.6: Predicted cross-sectional stresses for the baseline blade at 0°, 90°, 180°, 270° azimuth.

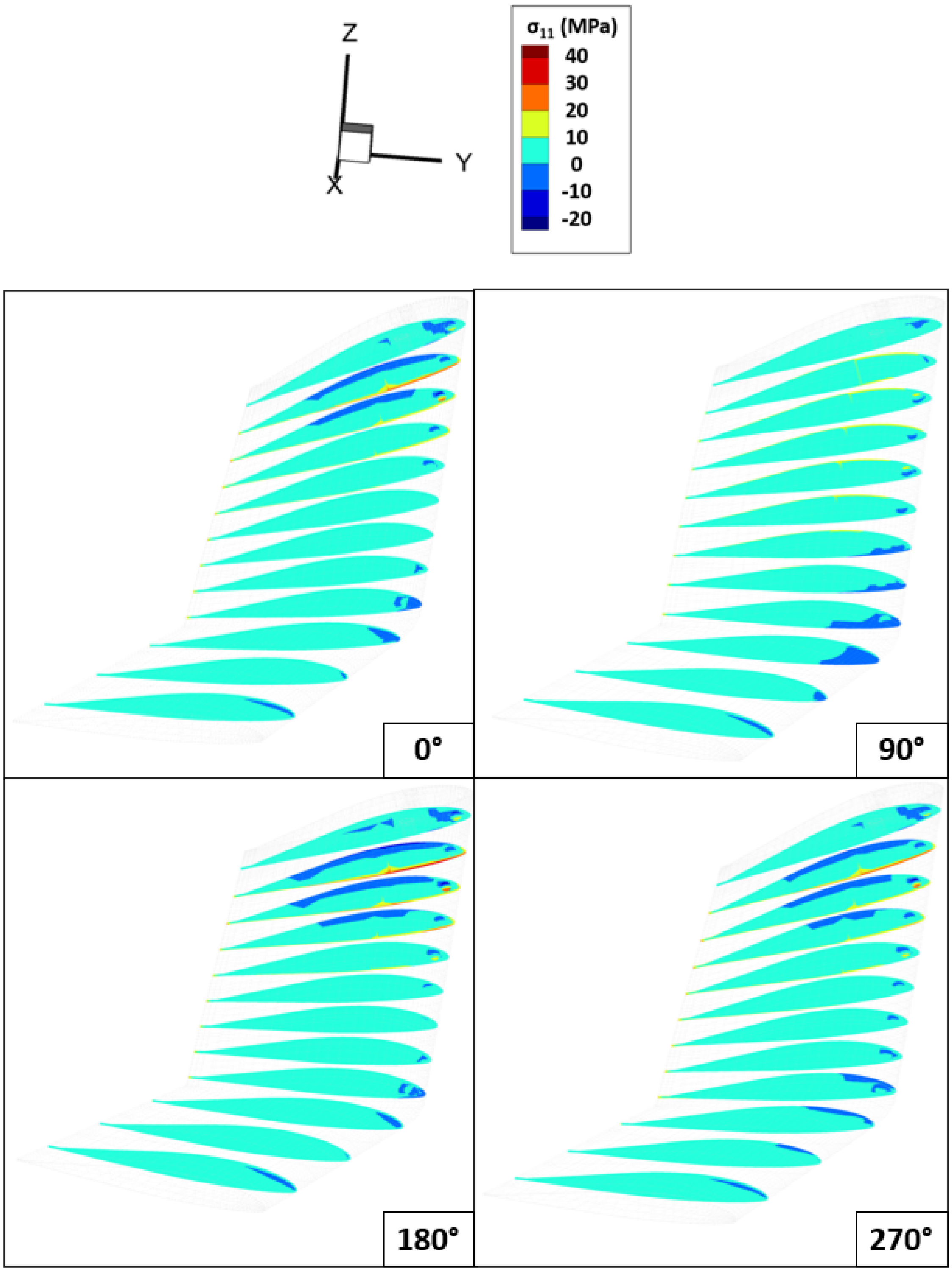

Figure 7.7: Predicted cross-sectional stresses for the swept-tip blade at 0°, 90°, 180°, 270° azimuth.

Chapter 8: Whirl Flutter Testing

This chapter covers the details of whirl flutter testing of the blades installed on the MTR. The first section describes the process required to prepare the blades for testing. Next, the procedure to acquire a whirl flutter test point during wind tunnel testing is described. The final section includes the results and discussion of the whirl flutter data in all test configurations.

8.1 Maryland Tiltrotor Rig Integration

The Maryland Tiltrotor Rig was installed in the Subsonic Wind Tunnel (SWT) located at the Naval Surface Warfare Center Carderock Division. This facility was chosen for use after a series of closures and delays with the Glenn L. Marting Wind Tunnel (GLMWT) which the MTR was designed for. The SWT has a similar cross section, 8- by 10-feet, but a maximum speed of 163 knots, lower than the 200 knots of the GLMWT. The tests were cleared only up to an even lower speed of 100 knots. Applying the Froude scale factor of 1/5.26, this equates to approximately 230 knots for a full-scale aircraft.

The Maryland Tiltrotor Rig was designed to allow for interchangeable blades. The process of changing blades only takes a few minutes. The pitch case and blade grip adapter are designed to be common between blade sets, so only three bolts and sensor connections need to be changed. First, the nose cone must be removed to allow access to the hub components and instrumentation plate. Next, all blade strain gauge wires are disconnected from the instrumentation plate at the hub. Then the three 9/16 inch diameter shoulder bolts connecting the straight blade to the grip adapter are unfastened, allowing for the removal of the blade. The swept-tip blade is installed with the same bolts. Although all three blades have normal and chord bending moment gauges, only four channels are available to record strain data. Therefore the normal and chord strain bridges from two blades are installed and should be noted in the test log. The excess length, as well as unconnected wires, are carefully wrapped around the pitch case and secured with metallic tape with care to ensure enough slack for full collective motion of the hub. Last, the strain gauge connections are verified with static deflections of the blade and rap tests.

Prior to installation, metallic tape was placed at the end of the straight section to ensure proper balance. The blades were balanced in pairs to ensure each has the same spanwise c.g. position. Additionally, retroreflective tape was adhered to the blade tip cross-section to allow for blade tracking. A light strobing at 3 /rev was aimed at the edge of the rotor disc, illuminating each blade as it passes. This was first done with the rotor spinning at 300 RPM and progressing to the nominal speed of 1050 RPM. With the swashplate level, the flap deflection of each blade had less than one airfoil thickness discrepancy and no discernible difference in lag deflection. The pitch links of each blade are adjustable in length to ensure uniform tracking, however no adjustments were necessary.

Figure 8.1: The swept-tip blades installed on the MTR in the Subsonic Wind Tunnel.

Figure 8.2: The MTR installed with wing fairings removed and baseline blades installed.

Table 8.1: Flutter test conditions.

Sweep	Tunnel Speed kts	Collective deg	Gimbal	Mode	Wing Assembly
Straight Blades Set 2					
1	30, 40, 50, 60, 65, 70, 74, 78, 82, 86, 89, 92, 96, 100	9.9, 17.6, 22.3, 26.7, 28.2, 30.0, 31.2, 32.8, 34.1, 35.4, 36.8, 37.5, 38.8, 39.8	Free	Freewheel	On
2	30, 40, 50, 60, 65, 70, 74, 78, 82, 86, 89, 92, 96, 100	10.4, 17.3, 22.4, 26.5, 28.6, 30.5, 31.7, 33.4, 34.6, 35.9, 36.8, 37.9, 39.1, 40.1	Free	Freewheel	Off
Set 1					
3	30, 40, 50, 60	11.3, 17.2, 22.1, 26.4	Locked	Freewheel	Off
4	4, 20, 30, 40, 50, 60	3.2, 11.4, 15.8, 20.7, 25.2, 28.9	Locked	Powered	Off
Swept-tip Blades					
5	30, 40, 50, 60, 65, 70, 74, 78, 82, 86, 89, 92, 96, 100	13.3, 18.9, 23.5, 27.4, 29.5, 31.2, 32.4, 34.3, 35.2, 37.1, 37.9, 39.0, 39.9, 40.7	Free	Freewheel	On
6	30, 40, 50, 60, 65, 70, 74, 78, 82, 86, 89, 92, 96, 100	11.9, 17.8, 22.0, 26.4, 28.8, 30.8, 32.5, 33.8, 35.1, 36.3, 37.8, 38.7, 39.6, 40.6	Free	Freewheel	Off
7	30, 40, 50, 60, 65, 70, 74, 78, 82	11.1, 17.1, 22.1, 26.5, 29.1, 31.4, 32.7, 34.3, 35.1	Locked	Freewheel	Off
8	4, 20, 30, 40, 50, 60	3.4, 13.0, 16.9, 21.6, 25.9, 29.7	Locked	Powered	Off

8.2 Whirl Flutter Test Procedure

Flutter test points were collected at nominal wind speeds for the wing beam and wing chord modes. At least three trials were performed per wing mode. The test conditions are shown in Table 8.1. The tests were performed with four major parametric changes, each performing a sweep of wind speed. The first 4 configurations use the straight rotor blades; configurations 5-8 are identical with the exception of having the swept-tip blades installed. The baseline configuration, Sweep 1, is the gimballed rotor with the twisted blades installed; the rotor is unpowered in a freewheel condition and is shown in Fig. 8.1. In Sweep 2, the wing fairing was removed to study the effect of wing aerodynamics on flutter stability. Figure 8.2 shows the MTR supported by the spar with wing fairing removed. With the wing fairings off, the gimbal was locked in Sweep 3, resulting in a stiff-inplane hingeless rotor. Finally, in Sweep 4, the rotor was powered by the electric motor to compare with results in the freewheel mode. Each configuration was tested with both straight and swept-tip blades.

To conduct the flutter test in freewheel conditions, the tunnel was set to the desired wind speed while the collective was adjusted to maintain 1050 RPM. When the gimbal was not locked, cyclic controls were input to trim the rotor. Under powered conditions, the motor throttle controlled RPM, and the rotor was trimmed to a constant thrust using collective pitch. Once at the specified condition, the swashplate was perturbed using the high bandwidth electric actuators of the MTR in order to excite the wing modes. For beam bending excitation, an approximately 0.5° perturbation in longitudinal cyclic at the wing beam frequency was applied while recording the strain at the root of the wing spar. For

Table 8.2: Measured frequencies of wing beam and chord modes in each configuration with both blade sets.

	Beam Frequency (Hz)		**Chord Frequency (Hz)**	
	Straight	**Swept-Tip**	**Straight**	**Swept-Tip**
Configuration 1, 4	5.04	5.06	9.45	9.39
Configuration 2, 5	5.05	5.06	9.47	9.39
Configuration 3, 6	5.05	5.03	9.45	9.44
Configuration 7, 8	5.03	5.03	9.49	9.48

chord bending excitation, an 0.5° perturbation in collective at the wing chord frequency was applied. Three trials were performed for each bending mode at each wind speed and a modified moving block method was used to extract the frequency and damping of the wing strain signals.

8.3 Whirl Flutter Results

Because each configuration was tested with both blade sets, this section draws direct comparisons between the straight and swept-tip blades in each configuration. Figure 8.3 shows the collective setting of each blade, θ_{75}, required for the MTR to maintain 1050 RPM at each speed. The correlation between the blades indicates the swept-tip blades are aerodynamically similar to the straight blades.

For all Figures 8.4-8.8b, the symbols show the measured frequency or damping during each individual trial. Squares symbolize values of wing chord frequency and damping, while triangles symbolize the wing beam mode. Results for the straight blade are plotted in gray, while the swept-tip blade results are plotted in red for chord and black for beam bending modes. All frequency and damping measurements are tabulated in Appendix A.

The wing structural damping was measured to be 0.4% in the beam mode and 0.57%

in the chord mode. Since this was the first whirl flutter test for the Maryland Tiltrotor Rig, and the first stability test in the Subsonic Wind Tunnel, initial testing proceeded cautiously. But at these low damping values, the MTR showed very little response to any natural perturbations in airflow. After swashplate perturbation, a safety officer was able to visibly watch the wing vibrations damp out while the test engineer observed the wing strain decay at the same rate. Observing the test rig stability and response to perturbation provided the confidence necessary to proceed to higher wind speeds.

8.3.1 Baseline Configurations

Sweeps 1 and 5 are in the baseline configuration, the gimballed rotor is in a free-wheeling condition and the wing fairings are installed. As summarized in Table 8.2, Fig. 8.4 shows no change to the wing bending frequencies in the baseline configuration; the same conclusion can be made for each subsequent configuration and so those results are omitted. Figures 8.5a and 8.5b shows the measured damping of the wing beam and chord bending modes in the baseline configuration.

For both blade sets, the damping of the beam mode starts low, approximately 0.5 %, and gradually grows to approximately 1%. At low speeds, there is no noticeable difference between the beam damping of the straight and swept-tip blades. At higher speeds, there is larger scatter between each trial. However, the beam damping with the swept-tip blades installed appears to increase more than when the straight blades are installed. Looking at the chord mode, the damping gradually decreases from approximately 1.5% to 1.2%. At nearly every wind speed, there is an approximately 10% increase in wing chord damping ratio when the swept-tip blades are installed. These results appear to be

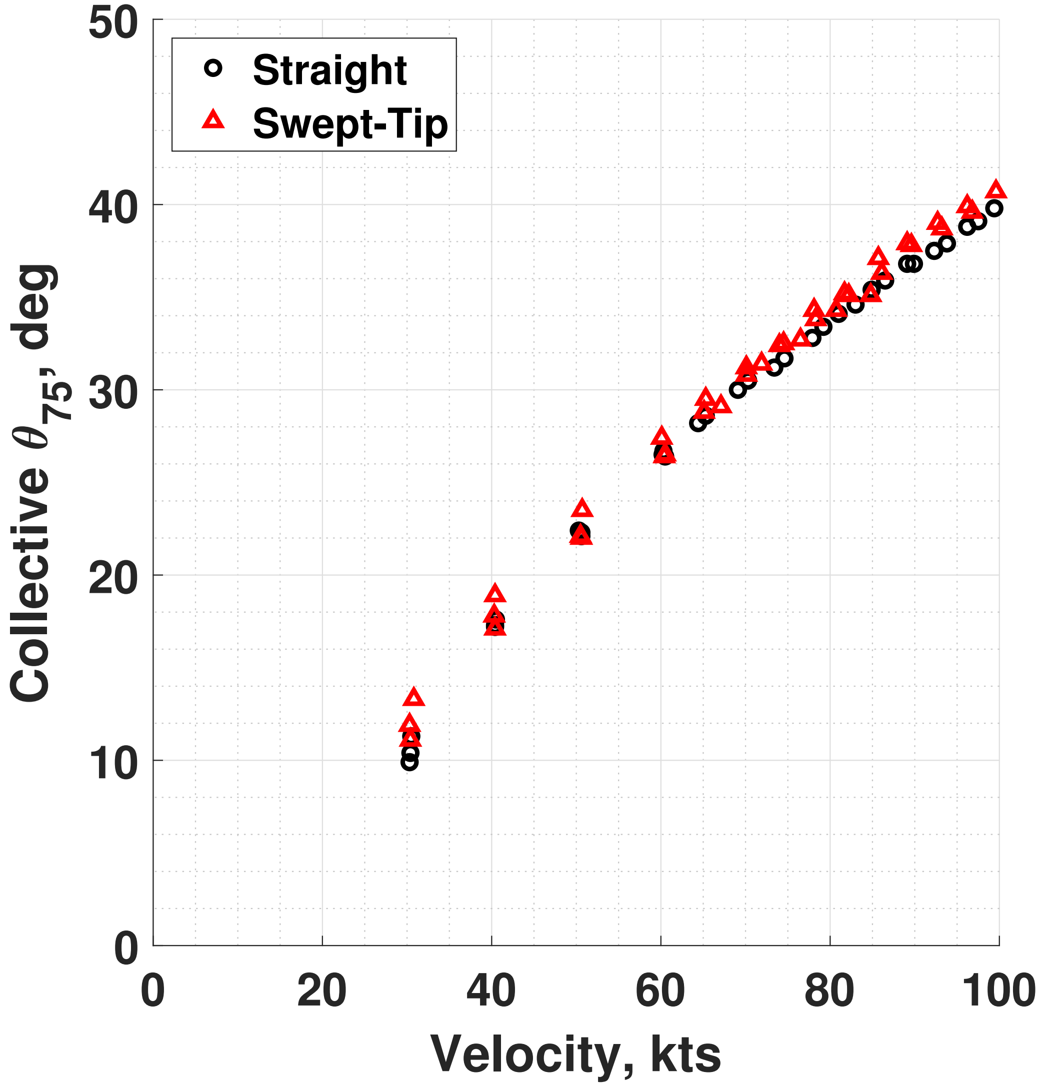

Figure 8.3: Collective, θ_{75}, required to maintain 1050 RPM at each wind speed for straight and swept-tip blades.

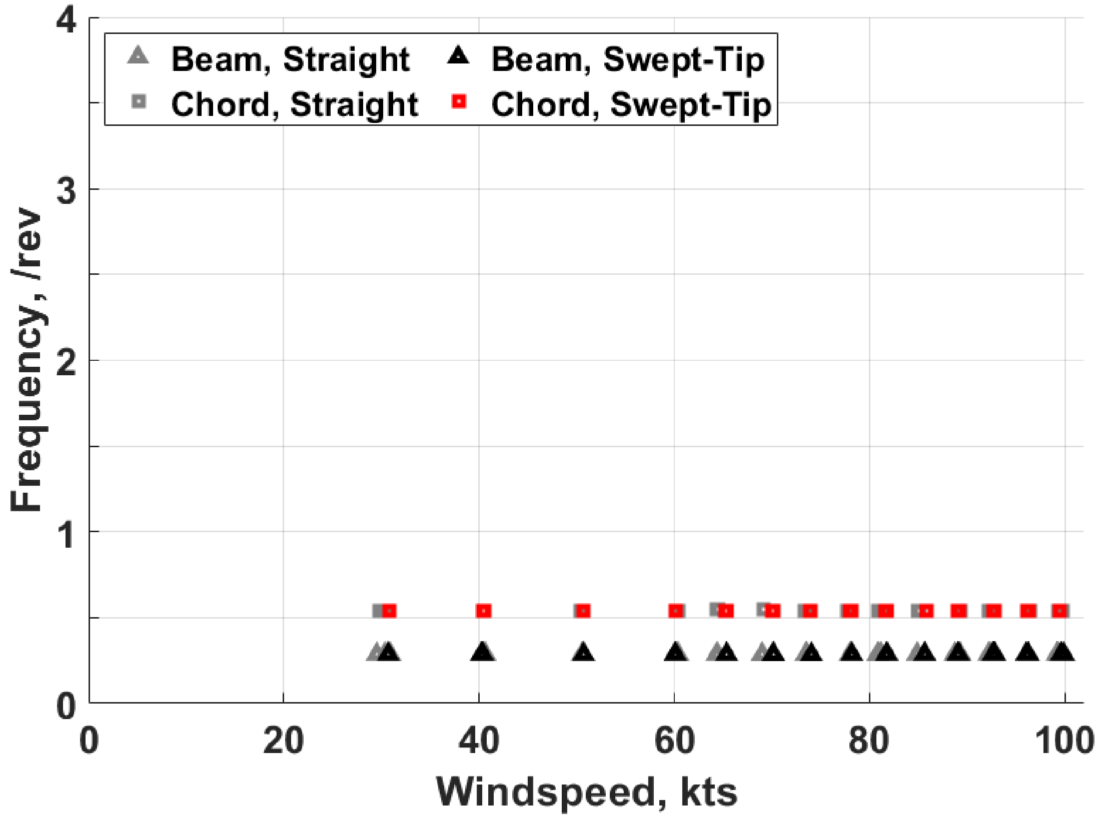

Figure 8.4: Measured frequency of the wing beam and chord bending in Configurations 1 and 5.

consistent with trends presented in previous analysis, where blade tip sweep has a more pronounced effect on the wing chord damping than the beam damping [45, 63]. The previous numerical studies predict a much larger increase in wing damping when the blade tip is swept 20° aft, however those results are for higher windspeeds and the swept tip blades has not yet been tested in those regimes.

8.3.2 Wing-Off Configurations

In Sweeps 2 and 6, the MTR is in a similar condition to Sweeps 1 and 5 with a gimballed rotor in a freewheeling condition except the wing fairings have been removed. Thus, the only effect on the results should be due to aerodynamics on the wing. In Figs. 8.6a and 8.6b, the same general trends of the baseline configuration are observed. The beam damping increases from approximately 0.5 % and gradually grows to approximately 1%. The chord mode decreases at a lower rate than with the wing installed from 1.3% on average to 1.2% over the 100 knot sweep.

The swept-tip beam mode damping follows closely with the straight blade results with variations within the data scatter. The damping of the wing chord mode is relatively unaffected by blade geometry up to 60 knots. But, between 70 and 86 knots, the swept-tip blade damping shows an increase in damping from 1.1% to 1.6% over the straight blades before returning back to the same increase observed with the wing fairings installed. This jump indicates that, even though the effects of sweep are expected to take effect at higher speeds, there are significant changes at lower speeds. However, the cause is unknown and presents an interesting case for further analysis and predictions to understand.

8.3.3 Gimbal Locked Configurations

In Sweeps 3 and 7, the rotor gimbal is locked but still freewheeling and the wing fairings are removed. The gimbal locked condition approximates a stiff in-plane hingeless hub with a first flap frequency of 1.8 /rev. Since flight with the gimbal locked was predicted to have higher damping prior to the test, testing in this condition was performed prior to the gimballed rotor testing. In order to build confidence in the test rig, initial sweeps only reached 60 knots until enough data was collected to safely proceed to 82 knots, and ultimately 100 knots. Unfortunately, due to limited test time, earlier runs were not able to be revisited and tested to the full range of speeds. Although the wind speed of Sweep 3 only covers 20-60 knots, Sweep 7 goes up to 82 knots.

Figures. 8.7a and 8.7b show the measured beam and chord damping of the wing for each test point. The wing beam damping shows the same overall trend as the gimbal free case but the wing chord damping is over 2% critical, nearly double the measured damping of the gimbal free case. When comparing the blade sets, no noticeable difference in wing beam damping can be observed between the straight and swept-tip blades. However, the swept-tip blades have a strong effect on chord damping. At 30 knots, the swept-tip blade increases the wing chord damping from 2.1% to 2.3% of critical. As wind speed increases, the wing chord damping decreases linearly for both sweeps, but the measured damping of Sweep 7 is decreasing at less than half the rate of Sweep 3. Based on these results, locking the gimbal drastically increases the wing chord damping compared to the gimballed rotor and the swept-tip blade further adds to the benefit. This test condition in Sweep 7 provides

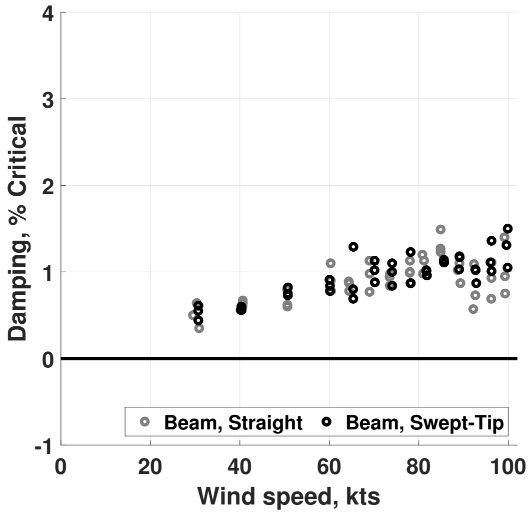

(a) Wing beam bending

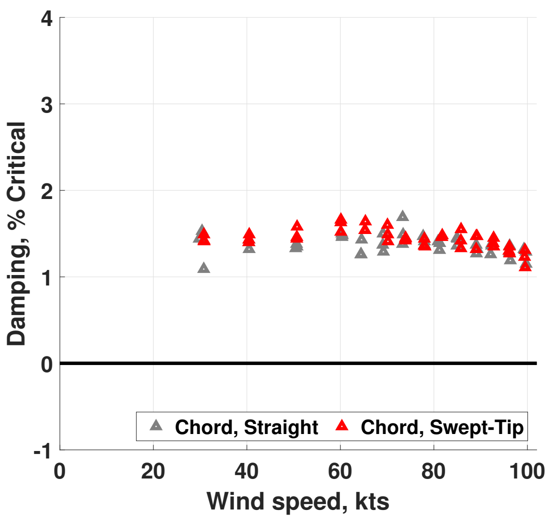

(b) Wing chord bending

Figure 8.5: Measured damping results of Sweeps 1 and 5.

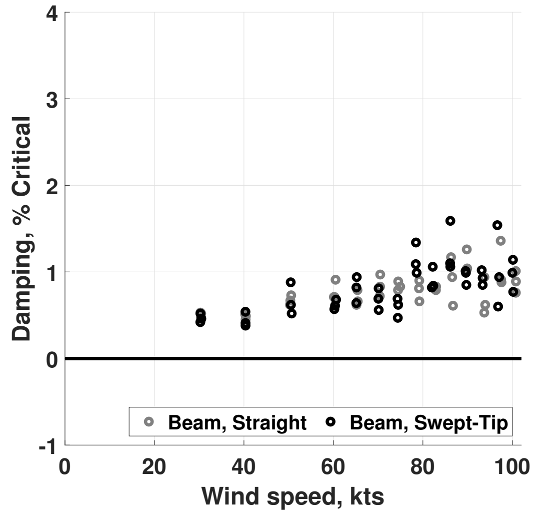

(a) Wing beam bending

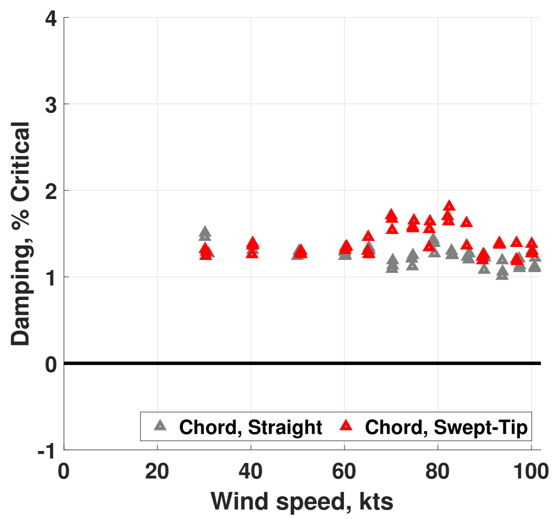

(b) Wing chord bending

Figure 8.6: Measured damping results of Sweeps 2 and 6.

the largest benefit to wing chord damping out of all freewheel configurations.

8.3.4 Powered Configurations

In Sweeps 4 and 8, the rotor gimbal is locked, the motor is powered on, and the wing fairings are removed. Due to electromagnetic interference between the motor and load cell, thrust measurements were not reliable. So the collective was set based on predictions for zero thrust. Although the first test point was tested at nominally 0 knots, the rotor recirculates flow through the wind tunnel and induces a 4 knot wind in the test section. Figures 8.8a and 8.8b show minimal difference in the wing beam bending between the straight and swept-tip blade sets at this condition.

Comparing Sweeps 4 and 8 to Sweeps 3 and 7 demonstrates the effect of powering the rotor versus freewheeling. When the rotor is powered, the wing beam damping ratio increase by 0.1% consistently across all tested wind speeds. The straight and swept-tip blades have very similar results for wing beam damping ratio. When the rotor is powered, the wing chord damping also sees a dramatic increase, as has been observed historically. However, the swept-tip causes a 20% decrease in the measured chord damping, the opposite effect observed in all freewheeling cases. While the test data obviously shows the effect of swept-tip, there is not yet an obvious answer why it causes such a dramatic decrease in Sweep 8. Therefore, it is critical to investigate how the combination of different parameter changes effect the wing damping in combination, not only in isolation. Thus, these conditions provide ample validation challenges for high-fidelity simulations.

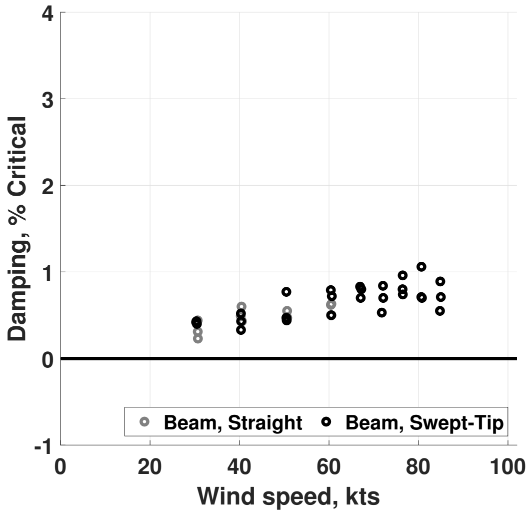

(a) Wing beam bending.

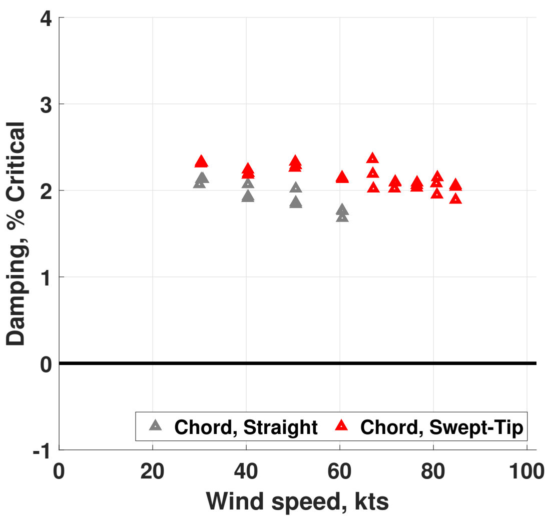

(b) Wing chord bending.

Figure 8.7: Measured damping results of Sweeps 3 and 7.

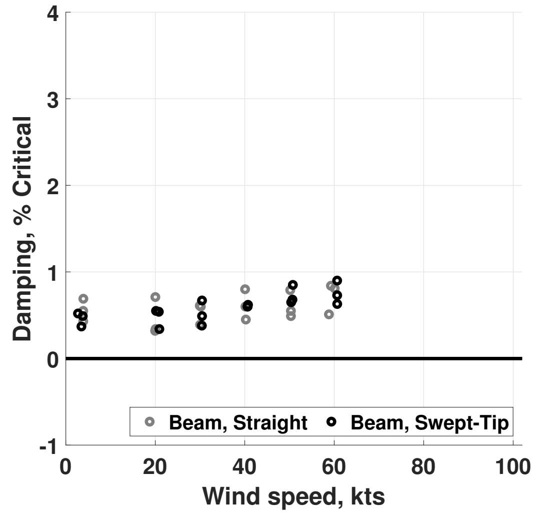

(a) Wing beam bending.

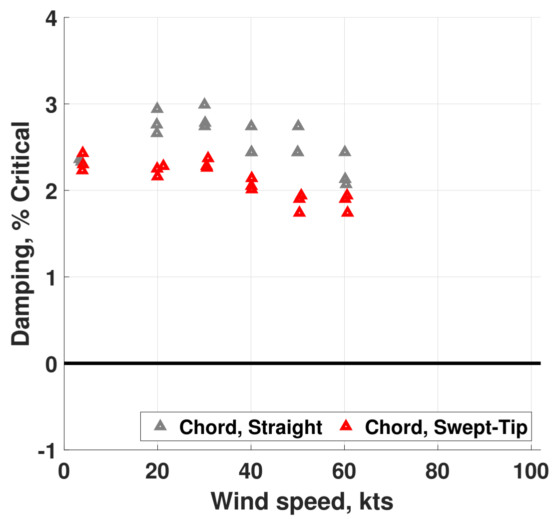

(b) Wing chord bending.

Figure 8.8: Measured amping results of Sweeps 4 and 8.

Chapter 9: Summary and Conclusions

This chapter summarizes the dissertation, highlights key conclusions that were made, and provides recommendations to continue the work in the future.

9.1 Summary

The main objective of the dissertation was to experimentally demonstrate that swept-tip tiltrotor blade geometries can increase the damping of the wing to delay whirl flutter and enable high speed tiltrotor flight. In recent years, numerical studies have demonstrated the benefit of blades where the outer 20% of the blade tip is swept aft by 20 °. But, tiltrotor blades with such a large swept-tip have never been fabricated and the dynamics have not been experimentally studied.

This dissertation covered the design, fabrication, characterization, 3-D finite element modeling, and whirl flutter testing of swept-tip tiltrotor blades. The blade properties were loosely designed on the 1/5.26 Froude-scale XV-15 properties. Two sets of blades were fabricated. A 20° sweep back was used on the swept-tip blades to introduce aerodynamic coupling and potentially delay whirl flutter. A 3-D finite element model was developed in unison to produce a high-fidelity representation of the fabricated blade based on the measured blade properties. In order to measure the blade sectional stiffness properties, a new method was developed using accelerometers to measure the bending slope along the blade under a tip load. Testing and simulation was performed on the blades in vacuum, recording strain levels and rotating frequencies. The 3-D model was validated by comparing to the measured properties of the fabricated blade. Ultimately, the blades were simulated in hover and forward flight to evaluate performance and structural integrity. The blades were installed on the Maryland Tiltrotor Rig and whirl flutter tests were carried out in the Subsonic Wind Tunnel located at the Naval Surface Warfare Center, Carderock Division. The whirl flutter tests followed a systematic variation of parameters including comparisons of wing aerodynamics, gimballed vs hingeless, freewheel vs powered flight, and straight vs swept-tip blades. Thus, there are enough significant differences introduced by the swept-tip, even at lower speeds, to provide a rich data set of validation data for advanced analysis.

9.2 Conclusions

The key conclusions of this research effort are summarized below:

1. The high twist rate and large swept tip of advanced geometry tiltrotor blades introduces structural, inertial, and aerodynamic couplings. The high twist rate couples the flap and lag bending stiffnesses and presents a challenge for measuring the sectional stiffness properties. Any measurement represents an averaged value as the blade sections twist along the span. In order to measure sectional properties an untwisted and unswept blade with the same cross section should be used instead.

2. The use of accelerometers instead of mirrors to measure bending and torsional stiff-

ness is faster and more reliable without sacrificing precision.

3. The high-fidelity 3-D model developed for this work very closely matches the physical blade. This was achieved through the measurement of the composite material properties from coupon test and tuning the shear modulus. The static structural and inertial properties as well as first rotating frequency and surface strain show good agreement between the finite element model and fabricated blade. 3-D finite-element modeling tools, such as X3D, are required to capture the stress concentrations due to blade sweep.

4. Introducing a swept-tip has little effect on hover performance at the low tip Mach numbers at which they are analyzed. The only observable difference occurs as the swept-tip blade begins to stall. The 3-D analysis reveals that the large swept-tip alters the blade loading in hover due to the lag moment caused by centrifugal forces on the swept-tip. In forward flight, the swept tip alters the sectional airloads, reducing the peak-to-peak airloads.

5. The Maryland Tiltrotor Rig was successfully tested with measured wing damping ratios of 0.5% up to 100 knots. Changing between the straight and swept-tip blades results in less than 1% change in wing bending frequencies. Additionally, the wing beam mode damping shows little change between the straight and swept-tip blades up to 100 knots.

6. The damping of the wing chord mode is observed to increase 10%-50% with the swept-tip blades installed over the straight blades in all freewheel flight conditions.

When the gimbal is locked (stiff-inplane hingeless), the wing chord mode damping ratio increases up to 80% higher than the gimballed hub results under freewheeling conditions. This effect is further strengthened by the swept-tip blades which greatly reduce the downward trend in wing chord damping in freewheel, locked-gimbal flight.

7. Powered flight conditions are more highly damped than freewheel flight, however, the swept-tip blade causes a 20% reduction in wing chord damping.

9.3 Recommendations for Future Work

This dissertation represents just the first step to a rich program of research focused on the Maryland Tiltrotor Rig. As such, the following recommendations are made for continuing the research of advanced geometry tiltrotor blades:

1. The MTR should be installed in the Glenn L. Martin Wind Tunnel and the range of windspeeds gradually expanded up to 200 knots for the current blades.

2. The MTR should have its own dedicated hover test facility

3. The electric motor should be isolated from all sensors and reduce signal noise. This should allow for measurement of rotor performance, loads, pitch link and blade strains.

4. The blade rotating frequencies should be measured in the vacuum chamber using a hub with active pitch perturbation.

5. A range of swept-tip blades should be designed with parametric variations to study the key parameters contributing to the increased damping. First, additional mass should be placed in the leading edge of the straight section to build a swept-tip blade with the same mass as the straight blade. Second, a straight blade with composite couplings should be built such that it introduces the same bending-torsion coupling as the swept-tip.

6. Beyond sweep, the blade tip geometry should be parametrically varied across multiple advanced tip geometries. This includes anhedral and planform taper variations.

APPENDIX

Table A.1: Measured damping of wing beam mode during Sweeps 1 and 5, the baseline configuration.

Straight Blades			**Swept-Tip Blades**		
Windspeed (knots)	**Frequency (Hz)**	**Damping (% critical)**	**Windspeed (knots)**	**Frequency (Hz)**	**Damping (% critical)**
29.5	5.02	0.50	30.7	5.03	0.44
30.4	5.04	0.64	30.7	5.02	0.55
30.9	5.03	0.35	30.7	5.03	0.61
40.6	5.02	0.60	40.4	5.02	0.56
40.6	5.02	0.64	40.2	5.02	0.56
40.6	5.02	0.67	40.3	5.02	0.60
50.6	5.01	0.62	50.7	5.02	0.82
50.5	5.02	0.80	50.7	5.02	0.73
50.6	5.01	0.60	50.7	5.01	0.75
60.3	5.03	1.10	60.0	5.02	0.91
60.3	5.03	0.90	60.1	5.01	0.78
60.4	5.02	0.78	60.1	5.01	0.84
64.4	5.02	0.78	65.3	5.01	0.80
64.3	5.02	0.89	65.3	5.02	0.69
64.4	5.01	0.87	65.4	5.02	1.29
69.0	5.00	0.98	70.1	5.01	1.13
69.0	5.04	0.77	70.1	5.03	1.02

Table A.1: (continued)

Straight Blades			Swept-Tip Blades		
Windspeed (knots)	**Frequency (Hz)**	**Damping (% critical)**	**Windspeed (knots)**	**Frequency (Hz)**	**Damping (% critical)**
69.0	5.02	1.13	70.2	5.01	0.88
73.5	5.04	0.94	74.0	5.01	1.00
73.6	5.03	0.98	74.0	5.01	1.10
73.5	5.02	0.84	74.0	5.01	0.84
78.0	5.04	0.99	78.1	5.02	0.87
78.0	5.03	1.00	78.2	5.02	1.23
78.0	5.04	1.13	78.2	5.02	0.87
80.8	5.01	1.20	81.8	5.02	0.96
80.9	5.03	0.98	81.7	5.02	1.02
81.2	5.04	1.13	81.7	5.03	1.01
84.9	5.02	1.27	85.6	5.03	1.14
84.9	5.02	1.23	85.7	5.02	1.11
84.9	5.05	1.49	85.6	5.05	1.11
89.3	5.02	0.87	89.0	5.03	1.03
88.7	5.02	1.02	89.1	5.03	1.17
89.1	5.03	1.10	89.1	5.03	1.18
92.6	5.03	0.73	92.8	5.04	0.87
92.3	5.02	1.09	92.7	5.03	1.02

Table A.1: (continued)

Straight Blades			**Swept-Tip Blades**		
Windspeed (knots)	**Frequency (Hz)**	**Damping (% critical)**	**Windspeed (knots)**	**Frequency (Hz)**	**Damping (% critical)**
92.2	5.05	0.57	92.6	5.05	1.03
96.2	5.06	0.69	96.0	5.04	1.11
96.3	5.03	1.11	96.2	5.01	1.01
96.2	5.02	0.93	96.2	5.03	1.36
99.3	5.01	0.75	99.6	5.05	1.31
99.2	5.04	0.95	99.8	5.03	1.05
99.2	5.04	1.40	99.9	5.04	1.50

Table A.2: Measured damping of wing chord mode during Sweeps 1 and 5, the baseline configuration.

Straight Blades			Swept-Tip Blades		
Windspeed (knots)	**Frequency (Hz)**	**Damping (% critical)**	**Windspeed (knots)**	**Frequency (Hz)**	**Damping (% critical)**
30.8	9.52	1.09	30.8	9.50	1.49
30.4	9.50	1.53	30.8	9.50	1.41
29.8	9.51	1.44	30.8	9.50	1.42
40.4	9.50	1.43	40.4	9.50	1.43
40.4	9.52	1.40	40.5	9.49	1.49
40.5	9.51	1.32	40.4	9.51	1.40
50.4	9.52	1.33	50.7	9.52	1.44
50.7	9.51	1.35	50.7	9.51	1.58
50.6	9.51	1.38	50.7	9.52	1.46
60.3	9.51	1.46	60.1	9.51	1.52
60.4	9.51	1.48	60.1	9.51	1.66
60.3	9.51	1.50	60.1	9.51	1.63
64.4	9.53	1.26	65.2	9.49	1.54
64.5	9.54	1.43	65.3	9.50	1.54
64.4	9.54	1.26	65.4	9.49	1.64
69.2	9.54	1.29	70.1	9.52	1.60
69.1	9.53	1.50	70.1	9.49	1.49

Table A.2: (continued)

Straight Blades			Swept-Tip Blades		
Windspeed (knots)	**Frequency (Hz)**	**Damping (% critical)**	**Windspeed (knots)**	**Frequency (Hz)**	**Damping (% critical)**
69.1	9.54	1.37	70.2	9.51	1.41
73.3	9.50	1.69	73.9	9.51	1.44
73.3	9.50	1.38	74.0	9.50	1.45
73.4	9.51	1.49	73.9	9.49	1.42
77.7	9.50	1.47	78.0	9.46	1.44
78.0	9.51	1.41	78.1	9.46	1.35
78.0	9.51	1.37	77.9	9.44	1.36
81.2	9.50	1.39	81.8	9.45	1.48
81.2	9.49	1.31	81.7	9.45	1.46
80.9	9.49	1.41	81.7	9.45	1.46
85.0	9.46	1.44	85.8	9.43	1.55
84.9	9.46	1.36	85.8	9.43	1.33
84.9	9.46	1.45	85.8	9.46	1.42
89.0	9.46	1.37	89.2	9.45	1.47
89.1	9.46	1.27	89.1	9.45	1.47
89.3	9.46	1.32	89.0	9.45	1.32
92.4	9.45	1.38	92.7	9.45	1.39
92.3	9.45	1.36	92.8	9.46	1.45

Table A.2: (continued)

Straight Blades			Swept-Tip Blades		
Windspeed (knots)	**Frequency (Hz)**	**Damping (% critical)**	**Windspeed (knots)**	**Frequency (Hz)**	**Damping (% critical)**
92.1	9.46	1.26	92.8	9.44	1.35
96.1	9.46	1.28	96.1	9.45	1.30
96.2	9.46	1.36	96.2	9.45	1.35
96.4	9.46	1.19	96.2	9.44	1.27
99.7	9.45	1.29	99.5	9.45	1.31
99.7	9.45	1.15	99.4	9.45	1.23
99.3	9.45	1.32	99.5	9.47	1.11

Table A.3: Measured damping of wing beam mode during Sweeps 2 and 6, the wing off configuration.

Straight Blades			Swept-Tip Blades		
Windspeed (knots)	**Frequency (Hz)**	**Damping (% critical)**	**Windspeed (knots)**	**Frequency (Hz)**	**Damping (% critical)**
30.4	5.05	0.48	30.3	5.07	0.42
30.3	5.05	0.53	30.5	5.07	0.46
30.5	5.05	0.52	30.3	5.07	0.52
40.3	5.04	0.51	40.3	5.07	0.54
40.4	5.04	0.45	40.4	5.07	0.41
40.4	5.04	0.49	40.4	5.06	0.38
50.4	5.04	0.67	50.7	5.07	0.52
50.6	5.04	0.73	50.5	5.07	0.88
50.3	5.04	0.62	50.5	5.07	0.62
60.3	5.04	0.71	60.2	5.07	0.57
60.5	5.02	0.91	60.4	5.07	0.61
60.1	5.04	0.71	60.6	5.06	0.68
65.4	5.04	0.79	65.2	4.99	0.94
65.4	5.04	0.66	65.1	4.98	0.82
65.2	5.04	0.62	65.1	4.98	0.64
70.4	5.05	0.83	70.1	5.01	0.56
70.4	5.05	0.72	70.1	4.98	0.69

Table A.3: (continued)

Straight Blades			Swept-Tip Blades		
Windspeed (knots)	**Frequency (Hz)**	**Damping (% critical)**	**Windspeed (knots)**	**Frequency (Hz)**	**Damping (% critical)**
70.5	5.05	0.97	70.1	4.99	0.81
74.4	5.03	0.79	74.4	4.98	0.47
74.5	5.04	0.89	74.3	4.98	0.69
74.9	5.04	0.83	74.5	5.01	0.62
79.2	5.06	0.90	78.6	4.97	0.99
79.2	5.06	0.66	78.5	5.01	1.34
79.1	5.04	0.81	78.4	5.00	1.09
82.9	5.04	0.79	82.0	5.00	0.82
82.8	5.04	0.80	82.2	4.98	1.06
83.0	5.06	0.83	82.3	4.98	0.84
86.3	5.06	1.17	86.1	4.99	1.10
86.7	5.06	0.61	86.1	5.01	1.06
86.6	5.06	0.94	86.1	5.02	1.59
89.8	5.05	1.26	89.7	5.05	0.85
89.8	5.03	1.03	89.6	5.04	0.99
89.9	5.06	1.04	89.5	5.04	1.01
93.7	5.04	0.53	93.1	5.05	1.02
93.9	5.04	0.62	93.4	5.04	0.93

Table A.3: (continued)

Straight Blades			**Swept-Tip Blades**		
Windspeed (knots)	**Frequency (Hz)**	**Damping (% critical)**	**Windspeed (knots)**	**Frequency (Hz)**	**Damping (% critical)**
93.8	5.04	0.94	93.4	5.05	0.85
97.5	5.06	0.91	97.0	5.05	0.99
97.6	5.05	0.88	96.8	5.04	1.14
97.4	5.06	1.36	96.6	5.04	0.77
100.8	5.09	1.01	100.0	5.04	0.94
100.8	5.08	0.76	100.1	5.05	0.60
100.8	5.06	0.89	100.2	5.07	1.54

Table A.4: Measured damping of wing chord mode during Sweeps 2 and 6, the wing off configuration.

Straight Blades			**Swept-Tip Blades**		
Windspeed (knots)	**Frequency (Hz)**	**Damping (% critical)**	**Windspeed (knots)**	**Frequency (Hz)**	**Damping (% critical)**
31.0	9.46	1.27	30.4	9.51	1.29
30.2	9.49	1.51	30.3	9.50	1.24
30.1	9.49	1.46	30.2	9.50	1.32
40.5	9.43	1.37	40.4	9.47	1.39
40.4	9.43	1.31	40.2	9.47	1.26
40.3	9.43	1.38	40.4	9.47	1.36
49.9	9.45	1.24	50.6	9.48	1.28
50.3	9.44	1.30	50.7	9.48	1.30
50.2	9.42	1.27	50.7	9.48	1.26
60.2	9.45	1.25	60.2	9.50	1.34
60.0	9.45	1.24	60.5	9.50	1.35
60.1	9.45	1.29	60.2	9.50	1.31
65.2	9.45	1.34	65.1	9.50	1.46
65.3	9.46	1.27	65.0	9.44	1.30
65.3	9.45	1.31	65.2	9.46	1.26
70.3	9.47	1.13	70.2	9.45	1.67
70.2	9.47	1.09	70.2	9.43	1.54

Table A.4: (continued)

Straight Blades			Swept-Tip Blades		
Windspeed (knots)	**Frequency (Hz)**	**Damping (% critical)**	**Windspeed (knots)**	**Frequency (Hz)**	**Damping (% critical)**
70.3	9.48	1.19	70.0	9.49	1.71
74.5	9.47	1.12	74.9	9.42	1.65
74.4	9.48	1.21	74.6	9.41	1.56
74.6	9.48	1.25	74.6	9.42	1.58
79.3	9.48	1.27	78.1	9.43	1.34
79.2	9.49	1.39	78.3	9.42	1.64
79.0	9.48	1.43	78.2	9.42	1.55
82.9	9.47	1.30	82.4	9.44	1.81
83.2	9.46	1.25	82.3	9.40	1.64
82.9	9.45	1.25	82.1	9.39	1.70
86.3	9.45	1.23	86.1	9.40	1.38
86.6	9.45	1.20	86.2	9.42	1.36
86.7	9.45	1.27	86.1	9.42	1.62
90.0	9.46	1.22	89.5	9.41	1.23
90.0	9.47	1.25	89.7	9.42	1.26
89.9	9.47	1.08	89.5	9.41	1.19
93.8	9.45	1.06	93.2	9.44	1.38
93.7	9.44	1.01	93.1	9.43	1.39

Table A.4: (continued)

Straight Blades			Swept-Tip Blades		
Windspeed (knots)	**Frequency (Hz)**	**Damping (% critical)**	**Windspeed (knots)**	**Frequency (Hz)**	**Damping (% critical)**
93.8	9.43	1.19	93.1	9.42	1.37
97.5	9.41	1.13	96.9	9.43	1.38
97.4	9.43	1.21	96.8	9.41	1.30
97.4	9.42	1.10	96.8	9.42	1.27
100.7	9.39	1.10	100.1	9.41	1.18
100.7	9.38	1.12	100.2	9.42	1.20
100.8	9.40	1.22	100.0	9.42	1.39

Table A.5: Measured damping of wing beam mode during Sweeps 3 and 7, the gimbal locked configuration.

Straight Blades			Swept-Tip Blades		
Windspeed (knots)	**Frequency (Hz)**	**Damping (% critical)**	**Windspeed (knots)**	**Frequency (Hz)**	**Damping (% critical)**
30.7	5.06	0.31	30.3	5.08	0.42
30.6	5.06	0.44	30.4	5.08	0.43
30.7	5.05	0.23	30.5	5.07	0.40
40.5	5.06	0.43	40.3	5.07	0.33
40.4	5.06	0.60	40.3	5.07	0.52
40.3	5.04	0.49	40.3	5.07	0.43
50.6	5.06	0.48	50.5	5.07	0.44
50.6	5.04	0.55	50.5	5.07	0.47
50.7	5.05	0.47	50.5	5.07	0.77
60.4	5.05	0.50	60.6	5.06	0.72
60.4	5.04	0.62	60.4	5.07	0.79
60.5	5.05	0.63	60.5	5.07	0.50
			66.9	5.07	0.83
			67.1	5.06	0.70
			67.2	5.06	0.80
			71.8	5.06	0.53
			72.1	5.07	0.70

Table A.5: (continued)

Straight Blades			Swept-Tip Blades		
Windspeed (knots)	**Frequency (Hz)**	**Damping (% critical)**	**Windspeed (knots)**	**Frequency (Hz)**	**Damping (% critical)**
			72.1	5.07	0.84
			76.4	5.07	0.80
			76.5	5.05	0.96
			76.5	5.07	0.74
			80.6	5.07	0.71
			80.8	5.05	0.70
			80.7	5.07	1.06
			84.9	5.06	0.89
			85.0	5.07	0.71
			84.8	5.06	0.55

Table A.6: Measured damping of wing chord mode during Sweeps 3 and 7, the gimbal locked configuration.

Straight Blades			Swept-Tip Blades		
Windspeed (knots)	**Frequency (Hz)**	**Damping (% critical)**	**Windspeed (knots)**	**Frequency (Hz)**	**Damping (% critical)**
30.4	9.50	2.13	30.4	9.45	2.33
30.0	9.48	2.07	30.3	9.46	2.31
30.7	9.50	2.13	30.5	9.43	2.32
40.4	9.49	1.93	40.4	9.41	2.20
40.3	9.48	1.91	40.4	9.41	2.24
40.4	9.49	2.07	40.4	9.40	2.18
50.6	9.46	1.86	50.6	9.39	2.29
50.6	9.46	2.02	50.5	9.42	2.33
50.6	9.46	1.84	50.4	9.40	2.26
60.5	9.44	1.68	60.5	9.39	2.13
60.6	9.45	1.76	60.5	9.39	2.14
60.5	9.45	1.77	60.5	9.39	2.15
			67.2	9.40	2.02
			67.0	9.39	2.36
			67.0	9.38	2.19
			71.7	9.38	2.02
			71.8	9.41	2.10

Table A.6: (continued)

Straight Blades			Swept-Tip Blades		
Windspeed (knots)	**Frequency (Hz)**	**Damping (% critical)**	**Windspeed (knots)**	**Frequency (Hz)**	**Damping (% critical)**
			71.8	9.42	2.09
			76.4	9.41	2.06
			76.5	9.37	2.09
			76.4	9.35	2.03
			80.6	9.37	2.08
			80.8	9.36	1.95
			80.8	9.34	2.15
			84.7	9.33	1.89
			84.7	9.36	2.04
			84.7	9.33	2.06

Table A.7: Measured damping of wing beam mode during Sweeps 4 and 8, the powered configuration.

Straight Blades			Swept-Tip Blades		
Windspeed (knots)	**Frequency (Hz)**	**Damping (% critical)**	**Windspeed (knots)**	**Frequency (Hz)**	**Damping (% critical)**
3.9	5.07	0.55	2.7	5.07	0.52
3.9	5.04	0.43	3.5	5.06	0.37
3.9	5.05	0.69	3.8	5.06	0.49
20.1	5.04	0.34	20.8	5.08	0.54
20.0	5.00	0.71	20.9	5.07	0.34
20.0	5.04	0.32	20.2	5.07	0.55
30.2	5.06	0.60	30.4	5.07	0.67
30.0	5.06	0.61	30.4	5.08	0.38
30.0	5.04	0.39	30.5	5.07	0.49
40.1	5.05	0.80	40.6	5.06	0.60
40.2	5.04	0.45	40.6	5.07	0.60
40.1	5.06	0.60	40.7	5.06	0.62
40.2	5.05	5.05			
50.3	5.05	0.49	50.8	5.06	0.85
50.2	5.04	0.79	50.7	5.05	0.68
50.3	5.03	0.55	50.4	5.04	0.65
58.8	5.05	0.51	60.7	5.06	0.63

Table A.7: (continued)

Straight Blades			Swept-Tip Blades		
Windspeed (knots)	**Frequency (Hz)**	**Damping (% critical)**	**Windspeed (knots)**	**Frequency (Hz)**	**Damping (% critical)**
59.3	5.05	0.84	60.7	5.04	0.73
60.1	5.04	0.81	60.7	5.06	0.90

Table A.8: Measured damping of wing chord mode during Sweeps 4 and 8, the powered configuration.

Straight Blades			Swept-Tip Blades		
Windspeed (knots)	**Frequency (Hz)**	**Damping (% critical)**	**Windspeed (knots)**	**Frequency (Hz)**	**Damping (% critical)**
3.3	9.44	2.36	4.0	9.47	2.30
3.7	9.38	2.33	3.9	9.46	2.23
3.8	9.46	2.20	4.0	9.45	2.43
19.8	9.44	2.76	19.9	9.37	2.25
19.9	9.47	2.94	21.2	9.40	2.28
19.8	9.46	2.66	20.0	9.38	2.16
30.2	9.42	2.78	30.8	9.38	2.37
30.0	9.47	2.99	30.6	9.38	2.26
30.1	9.45	2.74	30.5	9.38	2.28
40.1	9.43	2.74	40.2	9.38	2.01
40.1	9.45	2.44	40.2	9.40	2.14
40.1	9.47	2.44	40.1	9.38	2.05
50.1	9.43	2.74	50.4	9.39	1.90
50.0	9.45	2.44	50.4	9.38	1.74
50.0	9.47	2.44	50.7	9.37	1.94
60.4	9.44	2.07	60.2	9.39	1.90
60.1	9.44	2.44	60.7	9.38	1.74

Table A.8: (continued)

Straight Blades			Swept-Tip Blades		
Windspeed (knots)	**Frequency (Hz)**	**Damping (% critical)**	**Windspeed (knots)**	**Frequency (Hz)**	**Damping (% critical)**
60.2	9.46	2.13	60.6	9.37	1.94

Bibliography

[1] Hirschberg, M. J., "A Perspective on the First Century of Vertical Flight," *SAE Transactions*, Vol. 108, No. 1: Journal of Aircraft, 1999, pp. 1113–1136.

[2] Muson, K., *Helicopters and Other Rotorcraft Since 1907*, The MacMillan Company, London, UK, 1968.

[3] Busemann, A., "Drücke auf kegelförmige Spitzen bei Bewegung mit Überschallgeschwindigkeit," *ZAMM - Journal of Applied Mathematics and Mechanics / Zeitschrift für Angewandte Mathematik und Mechanik*, Vol. 9, No. 6, 1929, pp. 496–498.

[4] Meier, H.-U., *German Development of the Swept Wing 1935–1945*, 2010.

[5] William Green, G. S., *The Great Book of Fighters*, MBI Publishing Company LLC, 2001.

[6] Ames Research Center, "Collected Works of Robert T. Jones," February 1976.

[7] Jones, R. T., "Wing Plan Forms for High-Speed Flight," March 1946.

[8] Ley, W., "The "Brickwall" in the Sky," *Astounding Science Fiction*, Vol. 42, No. 3, November 1948, pp. 78–99.

[9] Blackburn, A., *Aces Wild: The Race for Mach 1*, Scholarly Resources Inc, 1999.

[10] "Forward-Swept Wing Potential Studied," *Aviation Week and Space Technology*, Vol. 110, No. 5, January 1979, pp. 126–127.

[11] Uhad, G. C., Weeks, T. M., and Large, R., "Wind Tunnel Investigation of the Transonic Aerodynamic Characteristics of Forward Swept Wings," *Journal of Aircraft*, Vol. 20, No. 3, March 1983, pp. 195–202.

[12] Bertin, J. J., and Cummings, R. M., *Aerodynamics For Engineers*, 6th ed., Pearson, 2014.

[13] Kramer, E. H., and Smilg, B., "The Effect of Sweepforward on the Critical Flutter Speed of Wings," *Army Air Forces Reprt TSEAC 5-4595-2-6*, April 1946.

[14] Diederich, F. W., and Budiansky, B., "Divergence of Swept Wings," *NACA TN 1680*, August 1948.

[15] Weisshaar, T. A., “Divergence of Forward Swept Composite Wings,” 1979, pp. 51–59.

[16] Krone, N. J. J., “Divergence Elimination with Advanced Composites,” *AIAA Paper 75-1009*, August 1975.

[17] Ricketts, R. H., and Doggett, R. V. J., “Wind-Tunnel Experiments on Divergence of Forward-Swept Wings,” August 1980.

[18] Putnam, T. W., “X-29 Flight-Research Program,” *NACA TM 86025*, January 1984.

[19] Maisel, M. D., Giulianetti, D. J., and Dugan, D. C., “The History of the XV-15 Tilt Rotor Research Aircraft: From Concept to Fligt,” *NASA SP-2000-4517*, 2000.

[20] Brocklehurst, A., and Barakos, G. N., “A review of helicopter rotor blade tip shapes,” *Progress in Aerospace Sciences*, Vol. 56, Janurary 2013, pp. 35–74.

[21] Spivey, R. F., “Blade Tip Aerodynamics – Profile and Planform Effects,” *American Helicopter Society249th Annual Forum Proceedings*, May, 1968.

[22] Spivery, W. A., and Morehouse, G. G., “New Insights into the Design of Swept-Tip Rotor Blades,” *American Helicopter Society 26th Annual Forum Proceedings*, Washington, D.C., June, 1970.

[23] Aoyama, T., Kawachi, K., and Saito, S., “Effect of Blade-Tip Planform on Shock Wave of Advancing Helicopter Blade,” *Journal of Aircraft*, Vol. 32, No. 5, September-October 1995, pp. 955–961.

[24] Beaumier, P., Zibi, J., and Costes, M., “CFD drag and power prediction for a rotor in hover and forward flight – formulation and first applications,” *Journal of the American Helicopter Society*, Vol. 42, No. 4, October 1997, pp. 327–336.

[25] Desopper, A., “Study of Unsteady Transonic Flow on Rotor Blade with Different Tip Shapes,” *Vertica*, Vol. 9, No. 3, July 1985.

[26] Desopper, A., Lafon, P., Ceroni, P., and Philippe, J. J., “Ten Years of Rotor Flow Studies at ONERA,” *Journal of the American Helicopter Society*, Vol. 34, No. 1, January 1989.

[27] Philippe, J. J., and Vuillet, A., “Aerodynamic Design of Advanced Rotors with New Tip Shapes,” *American Helicopter Society 39th Annual Forum Proceedings*, St. Louis, MO, May, 1983.

[28] Smith, D., and Sigl, D., “Helicopter rotor tip shapes for reduced blade vortex interaction - An experimental investigation,” *33rd Aerospace Sciences Meeting and Exhibit*, Reno, NV, January 1995.

[29] Preston, M. B., and Leishman, J. G., “Trailing Vortex Measurements in the Wake of a Hovering Rotor Blade with Various Tip Shapes,” *American Helicopter Society 58th Annual Forum Proceedings*, Montreal, Canada, June, 2002.

[30] Lyrintzis, A. S., Jameson, J. R., and Koutsavdis, E. K., "A Study of Rotorcraft Blade-Tip Shape High-Speed Impulsive Noise Characteristics," *Journal of the American Helicopter Society*, Vol. 45, No. 1, January 2000, pp. 54–57.

[31] Prieur, J., Lafon, P., Caplot, M., and Desopper, A., "Aerodynamics and Acoustics of Rectangular and Swept Rotor Blade Tips," *American Helicopter Society National Specialists' Meeting on Aerodynamics and Aeroacoustics*, Arlington, TX, February 1987.

[32] Kim, K., and Chopra, I., "Aeroelastic Analysis of Swept, Anhedral, and Tapered Tip Rotor Blades," *Journal of the American Helicopter Society*, Vol. 37, No. 1, January 1992, pp. 15–30.

[33] Maier, T. H., Sharpe, D. L., and Abrego, A. I., "Aeroelastic Stability for Straight and Swept-Tip Rotor Blades in Hover and Forward Flight," *American Helicopter Society 25th Annual Forum Proceedings*, Montreal, Canada, May, 1999.

[34] Preston, M. B., and Leishman, J. G., "Aerodynamcs of the world speed record," *American Helicopter Society 43rd Annual Forum Proceedings*, May, 1987.

[35] Spenser, J. P., *Whirlybirds, a History of U.S. Helicopter Pioneers*, University of Washington Press, 1998.

[36] Mark, H., and Lynn, R. R., "Aircraft Without Airports – Changing the Way Men Fly," *Vertiflite*, May/June 1988, pp. 80–87.

[37] Schroers, L., "Dynamic Structural Aeroelastic Stability Testing of the XV-15 Tilt Rotor Research Aircraft," *NASA TM-84293*, December 1982.

[38] Bilger, J. M., Marr, R. L., and Zahedi, A., "Results of Structural Dynamic Testing of the XV-15 Tilt Rotor Research Aircraft," *American Helicopter Society 37th Annual Forum Proceedings*, New Orleans, LA, May, 1981.

[39] Arrington, W. L., Kumpel, M., Marr, R. L., and McEntire, K. G., "XV-15 Tilt Rotor Research Aircraft Flight Test Report," *Vol I-V, NASA CR 177406*, June 1985.

[40] Quigley, H. C., and Koenig, D. G., "A Flight Study of the Dynamic Stability of a Tilting-Rotor Convertiplane," *NASA TN D-778*, April 1961.

[41] Yeager, W. T., and Kvaternik, R. G., "A Historical Overview of Aeroelasticity Branch and Transonic Dynamics Tunnel Contributions to Rotorcraft Technology and Development," *NASA TM-2001-211054*, August 2001.

[42] Reed, W. H. I., "Review of Propeller-Rotor Whirl Flutter," *NASA TR R-264*, July 1967.

[43] Hall, W. E., "Prop-Rotor stability at High Advance Ratios," *Journal of the American Helicopter Society*, Vol. 11, No. 2, April 1966, pp. 11–26.

[44] Johnson, W., “Dynamics of Tilting Proprotor Aircraft in Cruise Flight,” *Technical Report TN D-7677, NASA*, May 1974.

[45] Acree, C. W., “Effects of V-22 Blade Modifications on Whirl Flutter and Loads,” *Journal of the American Helicopter Society*, Vol. 50, No. 3, July 2005, pp. 269–278.

[46] Nixon, M., Piatak, D., Corso, L., and Popelka, D., “Aeroelastic Tailoring for Stability Augmentation and Performance Enhancements of Tiltrotor Aircraft,” *Journal of the American Helicopter Society*, Vol. 45, No. 4, October 2000, pp. 270–279.

[47] “Hover, Low Speed and Conversion TEsts of a Tilt Rotor Aeroelastic Model,” *NASA CR 114615, Bell Helicopter Company, V/STOL Tilt Rotor Study, Vol VI*, May 1973.

[48] Magee, J. P., and Alexander, H. R., “Wind Tunnel Tests of a Full Scale Hingeless Prop/Rotor Designed for the Boeing Model 222 Tiltrotor Aircraft,” *Technical Report D222-10059-1*, April 1973.

[49] Weiberg, J. A., and Maisel, M. D., “Wind Tunnel Tests of the XV-15 Tiltrotor Aircraft,” *NASA TM 81177*, April 1980.

[50] Acree, C. W., Sheikman, A. L., and Norman, T. R., “High-Speed Wind Tunnel Tests of a Full-Scale Proprotor on the Tiltrotor Test Rig,” *Vertical Flight Society 75th Annual Forum Proceedings*, Philadelphia, PA, May, 2019.

[51] Ham, N. D., Bauer, P. H., Lawrence, T. H., and Yasue, M., “A Study of Gust and Control Response of Model Rotor-Propellers in a Wind Tunnel Airstream,” *NASA CR 137756*, August 1975.

[52] Ham, N. D., and Whitaker, H. P., “A Wind-Tunnel Investigation of Tilt-Rotor Gust Alleviation System,” *NASA CR 152264*, January 1978.

[53] Popelka, D., Sheffler, M., and Bilger, J., “Correlation of Test and Analysis for the 1/5-Scale V-22 Aeroelastic Model,” *Journal of the American Helicopter Society*, Vol. 32, No. 2, 1987, pp. 21–33.

[54] Piatak, D., Kvaternik, R. G., Nixon, M. W., Langston, C. W., Singleton, J. D., Bennett, R. L., and Brown, R. K., “A Parametric Investigation of Whirl-Flutter Stability on the WRATS Tiltrotor Model,” *Journal of the American Helicopter Society*, Vol. 47, No. 2, April 2002, pp. 134–144.

[55] Nixon, M. W., Langston, C. W., Singleton, J. D., Piatak, D. J., Kvaternik, R. G., Corso, L. M., and Brown, R. K., “Aeroelastic Stability of a Four-Bladed Semi-Articulated Soft-Inplane Tiltrotor Model,” *American Helicopter Society 59th Annual Forum Proceedings*, Pheonix, AZ, May 2003.

[56] Matuska, D., Dale, A., and Lorber, P., “Wind Tunnel Test of a Variable-Diameter Tiltrotor (VDTR) Model,” *NASA CR 177629*, 1994.

[57] Johnson, J. L., and Young, L. A., “Tilt Rotor Aeroacoustic Model Project,” *Confederation of European Aerospace Societies (CEAS) Forum on Aeroacoustics of Rotorcraft and Propellers*, Rome, Italy, June 1999.

[58] Kvaternik, R. G., and Kohn, J. S., “An Experimental and Analytical Investigation of Proprotor Whirl Flutter,” *NASA TP 1047*, December 1977.

[59] Gaffey, T. M., “The Effect of Positive Pitch-Flap Coupling (Negative δ_3) on Rotor Blade Motion Stability and Flapping,” *Journal of the American Helicopter Society*, Vol. 14, No. 2, April 1969, pp. 49–67.

[60] Settle, T. B., and Kidd, D. L., “Evolution and Test History of the V-22 0.2-Scale Aeroelastic Model,” *American Helicopter Society National Specialists’ Meeting on Rotorcraft Dynamics*, Arlington, TX, November 1989.

[61] Wolowicz, C. H., “Similitude Requirements and Scaling Relationships as Applied to Model Testing,” *NASA TP 1435*, August 1979.

[62] Hammond, C. E., and Doggett, R. V. J., “Determination of subcritical damping by moving-block/randomdec applications,” *Its Flutter Testing Technology*, 1976, pp. 59–76.

[63] Srinivas, V., Chopra, I., and Nixon, M., “Aeroelastic Analysis of Advanced Geometry Tiltrotor Aircraft,” *Journal of the American Helicopter Society*, Vol. 43, No. 3, July 1998, pp. 212–221.

[64] Barkai, S., and Rand, O., “The Influence of Composite Induced Couplings on Tiltrotor Whirl Flutter Stability,” *Journal of the American Helicopter Society*, Vol. 43, No. 2, April 1998, pp. 133–145.

[65] Liu, J., and McVeigh, M., “Design of Swept Blade Rotors for High-Speed Tiltrotor Application,” *AIAA Aircraft Design Systems and Operations Meeting*, Baltimore, MD, September 1991.

[66] Yen, J. G., “Effects of Blade Tip Shape on Dynamics, Cost, Weight, Aerodynamic Performance, and Aeroelastic Response,” *Journal of the American Helicopter Society*, Vol. 39, No. 4, October 2005, pp. 37–45.

[67] Bartie, K., Alexander, H., McVeigh, M., La Mon, S., and Bishop, H., “Hover Performance Tests of Baseline Metal and Advanced Techology Blade (ATB) Rotor Systems for the XV-15 Tilt Rotor Aircraft,” 1988.

[68] Krüger, W., “Multibody Analysis of Whirl Flutter Stability on a Tiltrotor Wind Tunnel Model,” *Proceedings of the Institution of Mechanical Engineers*, Part K: Journal of Multi-body Dynamics, Vol. 230, 2016, pp. 121–133.

[69] Beaumier, P., Decours, J., and Lefebvre, T., “Multibody Analysis of Whirl Flutter Stability on a Tiltrotor Wind Tunnel Model,” *26th ICAS Congress*, Anchorage, AK, September 2008.

[70] Tsai, F., "Development and Whirl Flutter Testing of the Maryland Tiltrotor Rig," *Ph.D. Dissertation*, University of Maryland, College Park, 2022.

[71] Morin, A., "Fabrication, Wind Tunnel Testing, and Freewheeling Analysis of 4.75-ft Diameter Composite Tiltrotor Blades," *M.S. Thesis*, University of Maryland, College Park, 2021.

[72] Han, S., and Bauchau, O., "High-fidelity, 3-D Stress Prediction for Composite Rotor Blades," *American Helicopter Society 73rd Annual Forum Proceedings*, Fort Worth, TX, May 9-11, 2017.

[73] Jung, S., and Lau, B., "Determination of HART I Blade Structural Properties by Laboratory Testing," *CR-2012-216039, NASA*, August 2012.

[74] Datta, A., "X3D – A 3-D Solid Finite Element Multibody Dynamic Analysis for Rotorcraft," *American Helicopter Society Technical Meeting on Aeromechanics Design for Vertical Lift*, San Francisco, CA, January 2016.

[75] Chi, C., Datta, A., Chopra, I., and Chen, R., "Three-Dimensional Strains on Twisted and Swept Composite Rotor Blades in Vacuum," *Journal of Aircraft*, Vol. 58, No. 1, January-February 2021, pp. 1–16.

[76] Srinivasan, G., and Baeder, J., "TURNS: A Free-Wake Euler/Navier-Stokes Numerical Method for Helicopter Rotors," *AIAA Journal: Technical Notes*, Vol. 31, No. 5, May 1993.

[77] Staruk, W., Jayaraman, B., and Sitaraman, J., "Integrated 3D Structural Dynamics Using the CREATE™ - AV Helios v9 Rotorcraft Analysis Framewor," *AIAA SciTech Forum*, AIAA 2019-2136, San Diego, CA, 2019.

[78] Bagai, A., and Leishman, J. G., "Rotor Free-Wake Modeling Using a Pseudoimplicit Relaxation Algorithm," *Journal of Aircraft*, Vol. 32, No. 6, December 1995, pp. 1276–1285.